universität wien

DISSERTATION / DOCTORAL THESIS

Titel der Dissertation /Title of the Doctoral Thesis

„Fabrication and characterization of graphene-based mixed-dimensional van der Waals heterostructures“

verfasst von / submitted by

Rasim Mirzayev, MSc

angestrebter akademischer Grad / in partial fulfilment of the requirements for the degree of

Doktor der Naturwissenschaften (Dr. rer. nat.)

Wien, 2021 / Vienna 2021

Studienkennzahl lt. Studienblatt / degree programme code as it appears on the student record sheet:	UA 796 605 411
Dissertationsgebiet lt. Studienblatt / field of study as it appears on the student record sheet:	Physik
Betreut von / Supervisor:	Assoz. Prof. Dr. Jani Kotakoski
Betreut von / Supervisor:	Univ.-Prof. Dipl.-Phys. Dr. Jannik C. Meyer

Abstract

Mixed-dimensional van der Waals (vdW) heterostructures constructed by integration of 2D materials with non-2D materials provide a distinct platform for next-generation optoelectronics and open a huge potential to fabricate novel devices based on functional device systems and metamaterials. For this purpose, carbon nanostructures are considered to be ideal building units and important candidate components for designing novel nanostructures due to their unique properties.

In this thesis, two distinct graphene-based mixed-dimensional heterostructures and their study by aberration-corrected scanning transmission electron microscopy (STEM) are presented. The first example is a novel 0D/2D Buckyball sandwich heterostructure that consists of free-standing, highly-ordered C_{60} molecules encapsulated between two graphene monolayers. This structure is obtained by vacuum deposition of C_{60} fullerenes on a free-suspended graphene monolayer and subsequent encapsulation in ambient conditions. The graphene sandwich provides a nanoscale reaction chamber, a clean interface to the microscope vacuum, partial protection from radiation damage during imaging under 60 keV electron beam, and a low contrast background that can be easily subtracted from the images. We show that the fullerene molecules in the C_{60} monolayer exhibit an anomalous truncated intermolecular spacing of 9.6±0.1 Å explained by vdW simulations. Further, we confirm the C_{60} crystallites follow a graphene epitaxy – zig-zag or armchair – and an ABA or ABC stacking configuration. Moreover, we study the diffusion and rotational dynamics of C_{60} molecules and show that fullerenes retain their rotational degree of freedom at room temperature, while they become rotationally locked when they bond to neighbouring molecules. The graphene sandwich system can provide a versatile platform for various molecular studies and nanoscale physics.

The second example is 1D/2D mixed-dimensional vdW heterostructure that incorporates a single-walled carbon nanotube (SWCNT) on a suspended graphene monolayer held together by vdW forces. We observe that after thermal annealing by laser irradiation, the SWCNTs self-align and thereby optimize the stacking of the lower nanotube wall with the underlying graphene lattice. Moreover, we show that both SWCNTs and the graphene deform as a result of vdW interaction at the interface, resulting in one-dimensional corrugations in the graphene lattice. The observed topographic features are strain-correlated but show no evident

sensitivity to carbon nanotube helicity, electronic structure, or stacking order. This structure and its atomic-scale analysis provide a profound insight into the interaction between the 1D and 2D carbon systems.

Zusammenfassung

Gemischtdimensionale van-der-Waals (vdW)-Heterostrukturen, die durch die Integration von 2D-Materialien mit Nicht-2D-Materialien konstruiert wurden, bieten eine besondere Plattform für die Optoelektronik der nächsten Generation und eröffnen ein enormes Potenzial für die Herstellung neuartiger Bauelemente basierend auf funktionalen Bauelementsystemen und Metamaterialien. Kohlenstoff-Nanostrukturen gelten dabei aufgrund ihrer einzigartigen Eigenschaften als ideale Bausteine und wichtige Kandidatenkomponenten für das Design neuartiger Nanostrukturen.

In dieser Arbeit werden zwei verschiedene Graphen-basierte gemischtdimensionale Heterostrukturen un deren Untersuchung durch aberrationskorrigiertes Rastertransmissionselektronenmikroskop (RTEM) vorgestellt. Das erste Beispiel ist eine neuartige 0D/2D-Buckyball-Sandwich Heterostruktur, die aus freistehenden, hochgeordneten C_{60}-Molekülen besteht, die zwischen zwei Graphen-Monoschichten eingekapselt sind. Diese Struktur wird durch Vakuumabscheidung von C_{60}-Fullerenen auf einer frei suspendierten Graphen-Monoschicht und anschließende Verkapselung unter Umgebungsbedingungen erhalten. Das Graphen-Sandwich bietet eine nanoskalige Reaktionskammer, eine saubere Schnittstelle zum Mikroskop-Vakuum, einen teilweisen Schutz vor Strahlungsschäden während der Bildgebung unter einem 60 keV-Elektronenstrahl und einen kontrastarmen Hintergrund, der leicht von den Bildern abgezogen werden kann. Wir zeigen, dass die Fullerenmoleküle in der C_{60}-Monoschicht einen anomalen verkürzten intermolekularen Abstand von 9.6±0.1 Å aufweisen, was durch vdW-Simulationen erklärt wird. Darüber hinaus bestätigen wir, dass die C_{60}-Kristallite einer Graphen-Epitaxie – Zick-Zack oder Sessel – und einer ABA- oder ABC-Stapelkonfiguration folgen. Darüber hinaus untersuchen wir die Diffusions- und Rotationsdynamik von C_{60}-Molekülen und zeigen, dass Fullerene ihren Rotationsfreiheitsgrad bei Raumtemperatur behalten, während sie bei Bindung an benachbarte Moleküle rotatorisch fixiert werden. Das Graphen-Sandwich-System kann eine vielseitige Plattform für verschiedene molekulare Studien und die Nanophysik bieten.

Das zweite Beispiel ist eine gemischtdimensionale 1D/2D-vdW-Heterostruktur, die eine einwandige Kohlenstoff-Nanoröhre (SWCNT) auf einer suspendierten Graphen-Monoschicht enthält, die durch vdW-Kräfte zusammengehalten wird. Wir beobachten, dass sich die SWCNTs nach der thermischen Nachbehandlung durch Laserbestrahlung selbst ausrichten und

dadurch die Stapelung der unteren Nanoröhrenwand mit dem darunter liegenden Graphengitter optimieren. Darüber hinaus zeigen wir, dass sich sowohl SWCNTs als auch das Graphen als Ergebnis der vdW Wechselwirkung an der Grenzfläche verformen, was zu eindimensionalen Wellungen im Graphengitter führt. Die beobachteten topographischen Merkmale sind spannungskorreliert, zeigen jedoch keine offensichtliche Empfindlichkeit gegenüber der Helizität der Kohlenstoffnanoröhren, der elektronischen Struktur oder der Stapelordnung. Diese Struktur und ihre Analyse auf atomarer Skala geben einen tiefen Einblick in die Wechselwirkung zwischen den 1D- und 2D-Kohlenstoffsystemen.

Acknowledgements

Many are the people who travelled with me in this journey of my PhD. I owe them heartfelt gratitude and respect for their participation in my struggles and joys, for their encouragement and patience, and ever present support.

First and foremost I wish to express my deepest appreciation and gratitude towards my two supervisors Prof. Jani Kotakoski and Prof. Jannik C. Meyer for offering continuous guidance, motivation, and encouragement throughout the development of this research project. The work presented in this thesis would not have been possible without their supervision and precious support.

I am greatly indebted to Prof. Jannik C. Meyer for providing me with the opportunity to do my PhD in his research group under his supervision and for his invaluable scientific support, insightful discussions, creative ideas, and for his patience and kindness all along the way. He contributed many of the key ideas for this work and guided me through my project with his great expertise and many helpful suggestions. Furthermore, I thank him for his help to develop my skills and gain the knowledge on how to conduct research and hence realize this thesis. Similarly, I would like to express my deep and sincere gratitude to Prof. Jani Kotakoski for his valuable guiding inputs to this research project, for his sharp vision on scientific problems, and particularly for his constant support, understanding, and patience during the writing process of my thesis. Without his help, I could not conclude this dissertation.

Throughout my PhD, I had the privilege to cooperate with Dr. Kimmo Mustonen to whom I would like to express my sincere appreciation and gratitude for all his support, for being the driving force in this project, for his numerous contributions and effort, and for his kindness and open-mindedness. He not only produced some amazing data but also shared this data with me, which triggered some major parts of this thesis. I am very thankful for all the fruitful discussions and the productive team spirit.

I am greatly thankful to Dr. Clemens Mangler for his invaluable assistance in STEM experiments and for creating an enjoyable and inspiring atmosphere in the lab. Also, I am very grateful to Prof. Toma Susi for his valuable contributions to this work, especially for the simulations, and for his great expertise and enthusiasm. I would also like to thank Dr. Bernhard C. Bayer and Christian Kramberger for their support during my research and for helping me to improve my experimental skills.

I sincerely thank Dr. Ugur Sezer for helping me translate the abstract

into German. He is not just a former colleague to me but also a dear friend with whom I shared many things. I would also like to thank Dr. Kenan Elibol for his valuable support during the writing process of my thesis and for being the most entertaining office mate. To all the other former and active members of our group I would like to express my gratitude for their direct and indirect contribution to this work, for their support, motivation, and for creating such a pleasant atmosphere to work in: Dr. Viera Skakalova, Dr. Andreas Mittelberger, Dr. Giacomo Argentero, Dr. Mohammad Monazam, Dr. Timothy Pennycook, Dr. Christoph Hofer, Stefan Hummel, Dr. Mukesh Tripathy, and Dr. Ursula Ludacka. I would also like to thank Mrs. Regina Pinter for her invaluable administrative support and friendliness.

Last, but definitely not least, many thanks to my family and friends for being always there for me and supporting me in every possible way.

Contents

List of acronyms

CNT carbon nanotube 18

CNTs carbon nanotubes 15

SWCNT single-walled carbon nanotube . . . . .

MWCNT multi-walled carbon nanotube 16

VMD Visual Molecular Dynamics 10

AIREBO Adaptive Intermolecular Reactive Empirical Bond Order 38

LAMMPS Large-scale Atomic/Molecular Massively Parallel Simulator 38

Chapter 1

Introduction

1.1 Overview and motivation

Carbon is regarded as one of the building blocks for life on Earth and it is one of the most versatile elements: it forms the basis for many chemical compounds, it exhibits many different bonding geometries and hybridization states and it has several allotropes with different dimensionality. Furthermore, nano-allotropes of carbon play significant role in the development of nanomaterials research and novel device applications. The first of these nanostructures to be discovered was the quasi-zero-dimensional (0D) C_{60} molecules. These molecules are also known as buckminsterfullerenes or buckyballs and were initially reported in 1985 [1]. Subsequently, several other fullerenes were discovered, such as C_{20}, C_{70}, C_{84}, and even larger ones, but C_{60} fullerenes are by far the most widely studied to date. Another major step in the development of carbon nanostructures was taken in 1991, with the discovery of quasi-one-dimensional (1D) carbon nanotubes [2], [3]. The most recently discovered carbon nanostructure is graphene, the first experimentally realized atomically-thin quasi-two-dimensional (2D) material. The isolation of graphene came in 2004 even though its existence had been predicted decades ago [4]. Graphene is also regarded as a building block of many other carbon-allotropes: it can be wrapped up to form fullerenes, rolled up to form cylindrical carbon nanotubes, or stacked with other graphene sheets to construct three-dimensional (3D) graphite. All of these carbon nano-allotropes can be regarded as members of the same family since they primarily consist of sp^2 hybridized carbon atoms arranged in a hexagonal lattice. As a result they all have some common properties, although they also have significant differences due to their different sizes and shapes.

The carbon nanostructures have attracted tremendous attention from various scientific and engineering disciplines owing to their fascinating electrical, mechanical, optical, chemical and thermal properties as well as their diverse potential applications in nanotechnology. These materials have been studied extensively and a lot of effort has been made to understand their fundamental physical and chemical properties. In fact, the experimental discovery of graphene has triggered the eruptive research and discovery of other 2D nanomaterials in the form of monolayers, bilayers, and multilayers. While these materials possess amazing range of properties, perhaps the most intriguing discovery is that these structures can also be combined into stacks to create new materials with novel hybrid properties known as vdW heterostructures. The vdW heterostructures are of great interest for the next generation technology because they open a huge potential to create numerous metamaterials and new devices tailored to a specific purpose [5].

Besides the assembly of different 2D atomic layers, 2D materials can be integrated with other non-2D materials through vdW forces, given the dangling-bond-free surface. Consequently, the formation of *mixed−dimensional vdW heterostructures* can be realized by hybridizing 2D materials with materials of different dimensionality. The study of combined 2D+nD (n=0, 1 and 3) materials have begun to emerge as a new field in low-dimensional materials research and represents a new class of vdW heterostructures for further study [6]. Such hybrid structures provide considerable freedom in material selection and allow to utilize the synergetic advantage of different dimensionalities.

This thesis focuses specifically on carbon-based mixed-dimensional vdW heterostructures. The very first study of combining different dimensionality carbon allotropes has been achieved by encapsulating C_{60} fullerene molecules in 1D carbon nanotubes to produce the first novel hybrid 0D/1D carbon nano-allotrope, so called 0D/1D *nano pea-pods* [7]. It was subsequently shown that C_{60} molecules trapped inside the nanotube self-assemble into vdW interacting chains and further coalesce into interior tubes, generating pairs of nested graphene cylinders upon high-temperature annealing [8]. Another noticeable example is collapsed double-walled carbon nanotubes intercalated with C_{60} molecules to form a nanoribbon-type pea-pods [9], [10]. A different combination of carbon allotropes as an example of 0D/3D, is C_{60}-intercalated graphite which has been studied theoretically and experimentally in the late 1990s and early 2000s [11], [12], [13]. One of the main motivations behind these studies was to produce stable alkali-metal-doped superconductive fullerenes, which is yet to be achieved since it was shown that fullerenes can exhibit

superconductivity when doped with alkali-metals at transition temperatures up to 33 K [14], [15], [16], [12].

Another purpose of encapsulating fullerenes in nanotubes besides creating a new structure was making it possible for the imaging and studying them under the high-resolution transmission electron microscopy (TEM) in which nanotubes act as 1D nano-containers, test-tubes or nano-reactors with reduced electron damage [17]. However, carbon nanotubes offer a 1D environment that allows to study the dynamics or reactions of fullerenes only in singular dimension. The limited space and only one possible direction of motion in nanotube environment does not provide any information on the structure and behaviour of molecules in two dimensions. Additionally, harsh insertion procedure and curved structure of nanotubes reduce their usability. Graphene can overcome these factors by offering a 2D system that provides a similar encapsulation environment, while at the same time allowing two degrees of freedom for the free motion of molecules. Graphene has also been shown to reduce electron damage at low voltages significantly [18], [19] and as will be shown later, offers better imaging conditions under an electron microscope and broader study of the fullerenes due to its dimensionality. Moreover, organic molecules, nanoparticles, and atomic layers can be deposited or transferred on graphene's atomically flat and inert surface more efficiently and in an ordered way, which increases its applicability [20].

In this thesis, first I present a 0D/2D novel hybrid heterostructure, namely buckyball sandwich, which consists of free-suspended one-molecule thick monolayers and multilayers of C_{60} crystals sandwiched between two graphene monolayers. This new material not only fills the gap in the available combinations of hybrid carbon nano-allotropes but also offers a powerful method to encapsulate nanomaterials for further characterization. This method proved to be effective in protecting the C_{60} molecules from e-beam damage and allowed us to study the structure, morphology, dynamics and bonding of C_{60} fullerenes at the atomic scale by utilizing state-of-the-art STEM. In addition to protecting the encapsulated nanostructures from vacuum and irradiation damage, the graphene sandwiching method also helps to stabilize structures that are otherwise not likely to exist in ambient temperatures.

Similar to carbon pea-pods, the C_{60} sandwiched between graphene monolayers are expected to have hybridized properties that could be suited for applications ranging from nanoscale lasers to spin cubit arrays and nanoscale mechanical elements [21], [22]. Furthermore, similar to calcium or potassium intercalated crystalline C_{60} [16], [14], alkali metal

co-intercalation of fullerene-graphene sandwich structure may turn it into a high-temperature superconductor [12], [11].

Subsequently, I present another mixed-dimensional carbon hybrid nanostructure, namely monolayer graphene-SWCNT heterostructure, which is an example of a suspended 1D/2D system. Here the interaction between the two nanostructures and their mutual deformations at the atomic-scale is investigated via STEM. The study of this interesting mixed-dimensional heterostructure may provide insights for nanoelectronic applications.

1.2 Outline of thesis

This thesis is structured as follows. An overview of the materials, different experimental methods, sample preparation procedures, and computational simulations used during this thesis will be given in chapter 2. First I will introduce the carbon nanostructures, subsequently I will illustrate the basis of transmission electron microscopy with a particular emphasis on scanning transmission electron microscopy and Raman spectroscopy. Consequently I will explain the sample preparation techniques and simulations used in this work.

In the third chapter of this thesis the main results of this research will be presented. The first part of chapter is dedicated to buckyball sandwich structure and the second part is dedicated to graphene-carbon nanotube heterointerface. All the results have already been published in peer-reviewed scientific journals and listed in List of Publications section.

In chapter 4 a brief summary of the main results of this thesis will be given and finally outlook and future work will be discussed.

List of Publications

This thesis is based on the following publications:

1. **Buckyball sandwiches**

   Rasim Mirzayev, Kimmo Mustonen, Mohammad R. A. Monazam, Andreas Mittelberger, Timothy J. Pennycook, Clemens Mangler, Toma Susi, Jani Kotakoski and Jannik C. Meyer

   Science Advances, 3, 6 (2017)

   Abstract: Two-dimensional (2D) materials have considerably expanded the field of materials science in the past decade. Even more recently, various 2D materials have been assembled into vertical van der Waals heterostacks, and it has been proposed to combine them with other low-dimensional structures to create new materials with hybridized properties. We demonstrate the first direct images of a suspended 0D/2D heterostructure that incorporates C60 molecules between two graphene layers in a buckyball sandwich structure. We find clean and ordered C60 islands with thicknesses down to one molecule, shielded by the graphene layers from the microscope vacuum and partially protected from radiation damage during scanning transmission electron microscopy imaging. The sandwich structure serves as a 2D nanoscale reaction chamber, allowing the analysis of the structure of the molecules and their dynamics at atomic resolution.

   Author contributions: R.M contributed to sample preparation, STEM experiments, Raman spectroscopy experiments, data analysis and writing the paper.

2. **Atomic-Scale Deformations at the Interface of a Mixed-Dimensional van der Waals Heterostructure**

   Kimmo Mustonen, Aqeel Hussain, Christoph Hofer, Mohammad R. A. Monazam, **Rasim Mirzayev**, Kenan Elibol, Patrik Laiho, Clemens Mangler, Hua Jiang, Toma Susi, Esko I. Kauppinen, Jani Kotakoski, and Jannik C. Meyer

   ASC Nano, 12, 8, 8512–8519 (2018)

   Abstract: Molecular self-assembly due to chemical interactions is the basis of bottom-up nanofabrication, whereas weaker intermolecular forces dominate on the scale of macro-molecules. Recent

advances in synthesis and characterization have brought increasing attention to two- and mixed-dimensional heterostructures and it has been recognized that van der Waals (vdW) forces within the structure may have a significant impact on their morphology. Here, we suspend single-walled carbon nanotubes (SWCNTs) on graphene to create a model system for the study of a 1D-2D molecular inter-face through atomic resolution scanning transmission electron microscopy observations.

Author contributions: R.M contributed to sample preparation.

Publications not included in this thesis:

3. **Creating nanoporous graphene with swift heavy ions**

   Henrique Muiños Vázquez , Åhlgren Harriet, Ochedowski Oliver, Leino Aleksi, **Rasim Mirzayev**, Roland Kozubek , Henning Lebius, Karlusic Marko, Jaksic Milko, Arkady V. Krasheninnikov , Jani Kotakoski, Marika Schleberger, Kai Nordlund, Flyura Djurabekova

   Carbon, 114, 511 - 518 (2017)

   Abstract: We examine swift heavy ion-induced defect production in suspended single layer graphene using Raman spectroscopy and a two temperature molecular dynamics model that couples the ionic and electronic subsystems. We show that an increase in the electronic stopping power of the ion results in an increase in the size of the pore-type defects, with a defect formation threshold at 1.22–1.48 keV/layer. We also report calculations of the specific electronic heat capacity of graphene with different chemical potentials and discuss the electronic thermal conductivity of graphene at high electronic temperatures, suggesting a value in the range of 1 Wm^{-1} K^{-1}. These results indicate that swift heavy ions can create nanopores in graphene, and that their size can be tuned between 1 and 4 nm diameter by choosing a suitable stopping power.

4. **A new detection scheme for van der Waals heterostructures, imaging individual fullerenes between graphene sheets, and controlling the vacuum in scanning transmission electron microscopy**

   Giacomo Argentero, Kimmo Mustonen, **Rasim Mirzayev**, Andreas Mittelberger, Toma Susi, Gregor T. Leuthner, Y. Cao, Mohammad. R. A. Monazam, Timothy Pennycook, Clemens Mangler,

Christian Kramberger, Andre K. Geim, Jani Kotakoski, Jannik C. Meyer

Microscopy and Microanalysis, 23, 460-461 (2017)

5. **In-situ Raman study of laser-induced graphene oxidation**

Felix Herziger, **Rasim Mirzayev**, Emanuele Poliani, Janina Maultzsch

physica status solidi (b), 252(11), 2451-2455 (2015)

Abstract: We present in-situ Raman measurements of laser-induced oxidation in exfoliated single-layer graphene. By using high-power laser irradiation, we can selectively and in a controlled way initiate the oxidation process and investigate its evolution over time. Our results show that the laser-induced oxidation process is divided into two separate stages, namely tensile strain due to heating and subsequent p-type doping due to oxygen binding. We discuss the temporal evolution of the D/G-mode ratio during oxidation and explain the unexpected steady decrease of the defect-induced D mode at long irradiation times. Our results provide a deeper understanding of the oxidation process in single-layer graphene and demonstrate the possibility of sub-μm patterning of graphene by an optical method.

Chapter 2

Materials & Methods

2.1 Materials

2.1.1 Low-Dimensional Materials

Over the past decade dimensionality has become one of the most defining material parameters. Low-dimensional materials can be described as systems with reduced physical dimension in at least one spatial direction. Based on their reduced dimensionality, from the physical point of view, low-dimensional materials can be classified as 2D, 1D, and 0D. The carbon based nanomaterials such as fullerenes, carbon nanotubes and graphene are the major experimental realization of zero-, one-, and two-dimensional materials, respectively, as illustrated in figure 2.1 (b-d). In low-dimensional materials, the reduced dimensionality gives rise to confinement of motion of electrons. Due to this electronic confinement the properties of low-dimensional materials can differ significantly from their bulk form and they can exhibit unique and novel properties. By combining different low-dimensional materials, new functional materials with intriguing properties can be generated. Therefore controlled synthesis and processing of these materials has a critical importance.

Since the discovery of single layered 2D materials low-dimensional materials has been on the spotlight of the mainstream science because of their extraordinary physical properties and versatile potential applications. 2D materials were first discussed in the context of electronic properties of graphite in 1947 [4] but the experimental realization came with the isolation of graphene, the single layer of graphite, by Andre Geim and Konstantin Novoselov in 2004 [23]. This discovery earned them the Nobel Prize in Physics in 2010 for the "groundbreaking experiments regarding the two dimensional material graphene". It is interesting to note

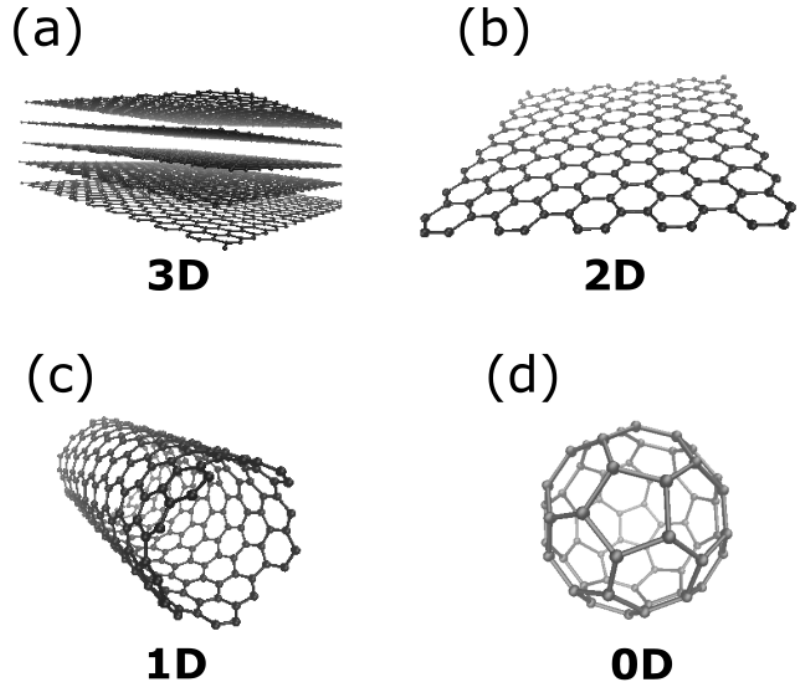

Figure 2.1: **Carbon nanostructures.** a) 3D graphite, b) 2D graphene, c) 1D carbon nanotube and d) 0D C_{60} fullerene. The images were made using Visual Molecular Dynamics (VMD) software.

that the discovery of graphene has surprised the science world because it was commonly accepted that 2D materials can not exist independently in an isolated form as predicted by Peierls [24], Landau [25] and Mermin [26]. However it was lately shown experimentally that graphene sheets are not perfectly flat and display spontaneous ripples due to thermal fluctuations [27]. The research in graphene has led to further studies in exploring the field of low-dimensional systems in general. In this thesis I mainly focus on the mixed-dimensional heterostructures which is a new field emerged as a result of studies in low-dimensional materials.

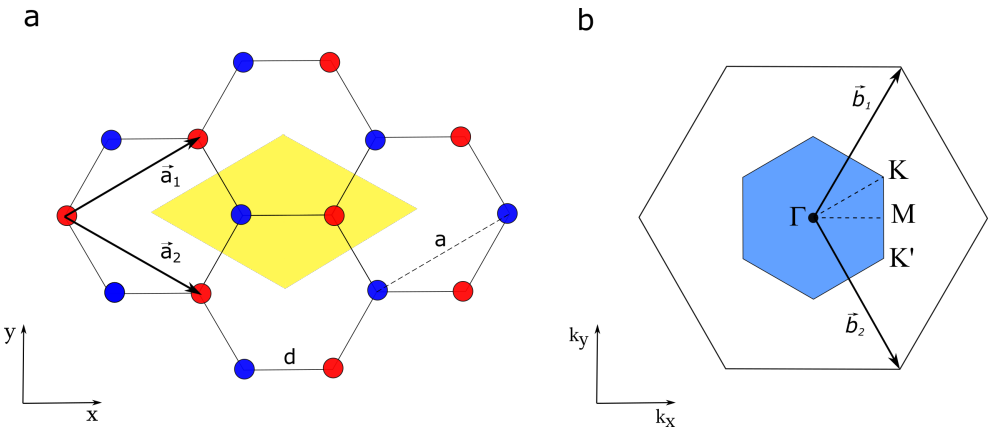

Figure 2.2: **The atomic structure of graphene.** a) The blue and the red dots represent the two inequivalent lattice positions. The unit cell is highlighted in yellow and the real space lattice vectors are $\vec{a}_1$ and $\vec{a}_2$. The lattice constant a is 2.46 Å and the interatomic distance d is 1.42 Å. b) Reciprocal lattice of graphene showing the first Brillouin zone highlighted by blue colour. Γ, K, K' and M are the high symmetry points. $\vec{b}_1$ and $\vec{b}_2$ are reciprocal lattice vectors.

2.1.2 Graphene

Graphene is a one-atom-thick layer of sp^2 bonded C atoms arranged in a two-dimensional honeycomb lattice. It is regarded as the basic building block of carbon nanostructures. It is the thinnest and strongest material known till now [28]. Since its discovery, graphene has become a topic of intense research because of its unique structural and electronic properties such as observation of Dirac dispersion, which leads to high thermal conductivity [29], very high electron mobility [30] and ballistic transport [31].

Graphene was first synthesized by extracting a single layer of graphite using micromechanical exfoliation, also known as scotch tape method. In fact, graphite is nothing else than 3D coupled graphene layers that stick together due to van der Waals interaction as depicted in figure 2.1a.

The hexagonal lattice structure of graphene and corresponding lattice vectors in real space $(\vec{a}_1, \vec{a}_2)$ are illustrated in figure 2.2a. The hexagonal lattice of graphene is not a Bravais lattice but can be seen as a triangular lattice with basis of two atoms per unit cell. The two sublattices are illustrated by red and blue colours. If d is the interatomic distance between the nearest neighbours, the primitive vectors can be chosen as

$$\vec{a}_1 = \frac{d}{2}(3, \sqrt{3}) \ , \qquad \vec{a}_2 = \frac{d}{2}(3, -\sqrt{3}) \ . \tag{2.1}$$

The distance between the carbon atoms d is about $1,42$ Å and the magnitude of the lattice vector $\vec{a}/a$ is $2,46$ Å. The reciprocal lattice vectors are

$$\vec{b}_1 = \frac{2\pi}{3d}(1, \sqrt{3}) \ , \qquad \vec{b}_2 = \frac{2\pi}{3d}(1, -\sqrt{3}) \ . \tag{2.2}$$

The first Brillouin zone is shown in 2.2b. The two non-equivalent K and K′ points at the corners of the first Brillouin zone are of particular importance for the electronic properties of graphene because the electrons have zero effective mass at these points and behave as massless Dirac particles. These points are known as Dirac points. Being massless allows the electron to move quickly within the graphene, which means graphene has high electron mobility. The electronic band structure of graphene (figure 2.3) can be calculated by using the tight binding approximation which neglects the interaction between atoms separated by large distances. The positions of the K and K′ points in reciprocal space are given by

$$K = \frac{2\pi}{3d}(1, \frac{1}{\sqrt{3}}) \ , \qquad K' = \frac{2\pi}{3d}(1, -\frac{1}{\sqrt{3}}) \ . \tag{2.3}$$

Each carbon atom has four valence electrons which are located in $2s$ and $2p$ orbitals. In graphene, the $2s^1$ orbital combines with two $2p$ orbitals ($2p_x^1$ and $2p_y^1$) to form three sp^2 hybridized orbitals separated by 120° and leave $2p_z^1$ orbital unhybridized. The sp^2 hybridized carbon atoms make strong covalent σ-bonds in the plane of graphene which makes the lattice structure robust, and leads to a hexagonal planar structure. On the other hand the remaining unhybridized $2p_z$ orbital, which is perpendicular to the graphene plane, forms π-bond with neighbouring carbon atoms. The extra π electron in $2p_z$ orbital has a great importance, since electronic properties of graphene are governed by this delocalized π electron. The energy dispersion of π electrons was first derived by Wallace using the tight-binding model [4]. The band dispersion, involving only the nearest neighbour t_1 and the next nearest neighbour t_2 hopping energies [32], is given as

$$E_{\pm}(\vec{k}) = \pm t_1 \sqrt{3 + f(\vec{k})} - t_2 f(\vec{k}) \ , \tag{2.4}$$

$$f(\vec{k}) = 4\cos\left(\frac{\sqrt{3}}{2}k_y d\right)\cos\left(\frac{3}{2}k_x d\right) + 2\cos\left(\sqrt{3}k_y d\right) \ , \tag{2.5}$$

where plus and minus signs correspond to upper π (conduction) band and lower π^* (valence) band, respectively and $\vec{k}$ is the wave vector. The resulting energy band dispersion of graphene is shown in figure 2.3. The conduction and valence bands touch each other at the two non-equivalent Dirac points (K and K′) which makes the graphene a zero band gap semiconductor or semimetal. The dispersion relation at low energies at the vicinity of the Dirac points becomes linear and can be expressed as

$$E_{\pm}(\vec{q}) \approx \pm v_F \left|\vec{q}\right| \ , \tag{2.6}$$

where $\vec{q}$ is the momentum vector relative to the Dirac point and v_F is the Fermi velocity for graphene with a value $v_F \approx 10^6$ m/s [32]. This shows that the carriers in graphene behave as massless Dirac fermions at low energies and their behaviour is described by Dirac relativistic equation. This linear energy dispersion is a hallmark of graphene and the Dirac nature of the electrons is the root cause of many interesting phenomena observed in graphene such as anomalous quantum Hall effect [33] and Klein tunnelling [34]. Perhaps one of the most interesting aspects of graphene physics is that it can be mixed with other low-dimensional materials to produce new structures with unique properties yielding rich new physics to be studied and exploited.

2.1.3 Fullerenes

Fullerenes are class of molecules made entirely of carbon atoms in a hollow closed-cage structure. They come in with wide variety of sizes and shapes depending on the number of carbon atoms such as C_{20}, C_{60}, C_{70}, and C_{82}. Among them C_{60} is the most abundant, the most widely investigated and the one that has been used most heavily to date, primarily because of its structural stability and unique high-symmetry spherical form. C_{60} fullerene is also known as buckminsterfullerene or buckyball because of its resemblance to famous geodesic domes designed by Buckminster Fuller [1]. Fullerenes were discovered experimentally by Kroto, Curl and Smalley in 1985 through laser evaporation of graphite. Later in

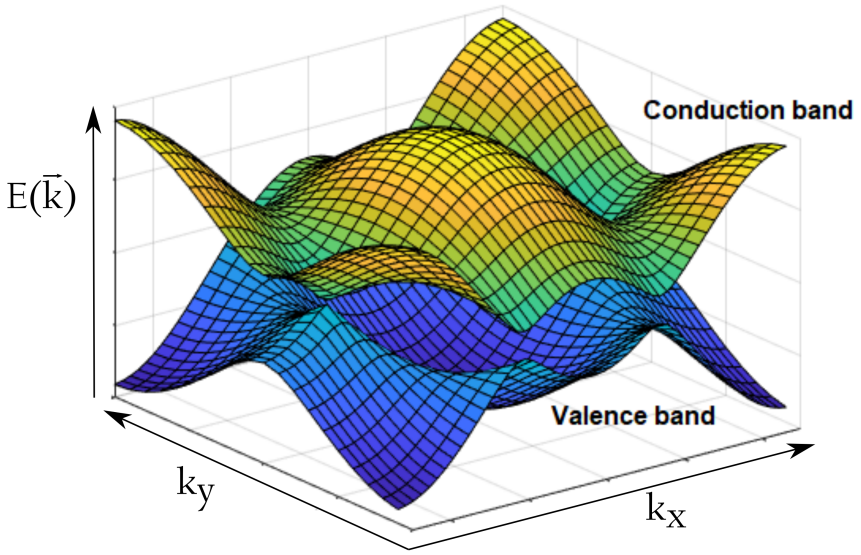

Figure 2.3: The electronic band structure of graphene. The image was obtained by using MATLAB software.

1996 they were awarded Nobel Prize in Chemistry for their discovery of a new form of carbon allotrope. In fact, the study of carbon nanostructures began with the discovery of the fullerenes. Buckyballs are spherical closed-cage molecules consisting of sixty carbon atoms. The carbon atoms in C_{60} are sp^2 hybridized and are covalently bonded to three other carbon atoms just like in graphene. This is why fullerenes are described as wrapped up or folded graphene. Because of their point-like spherical shape fullerenes are referred as zero-dimensional structures and also regarded as the smallest carbon nanostructure. The molecular structure can be described as a truncated icosahedron with 12 pentagonal and 20 hexagonal faces similar to a soccer ball. The pentagonal rings, which are isolated by hexagonal rings, provide curvature. The structure of C_{60} is depicted in figure 2.4.

Although each carbon atom is equivalent, there are two different bonds in C_{60} molecule; the double bond between two hexagons (6:6 bond) with a length of 1.39 Å and the single bond between pentagons and hexagons (5:6 bond) with a length of 1.46 Å [35]. The mean diameter of the C_{60} molecule has been determined to be about 7.10 Å and the outer diameter is about 10.04 Å [36].

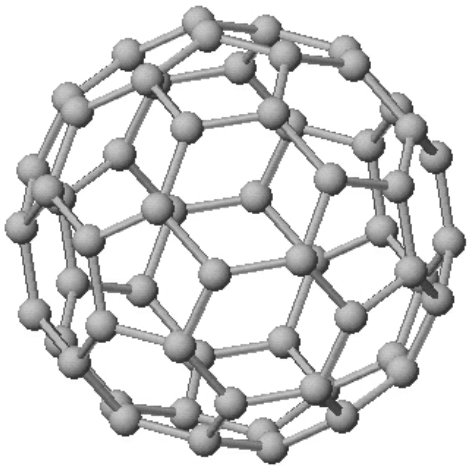

Figure 2.4: Structure of C_{60} fullerene. The image was created by using VMD software.

A common method to produce fullerenes is to apply a large current between two nearby graphite electrodes in an inert atmosphere. As a result carbon vaporizes into plasma in an electric arc that subsequently cools into sooty residue [1], [37], [38]. Alternative method is the laser ablation of graphite which yields clusters of fullerenes [39].

Fullerenes are versatile and have many interesting properties such as having a band gap under ambient conditions [40], becoming metallic when doped, and even exhibiting superconductivity under certain conditions [41]. Another interesting fact about fullerenes is that they belong to the rare group of saturable absorbers and can exhibit peculiar ferromagnetic behaviour when polymerized and at low temperatures [42], [43], [44].

Fullerenes have been used in composites, photo-resistive masks, and as lubricants. They have also applications in micro electronics, optics, solar cells, batteries for efficient energy storage and hydrogen fuel cells. Fullerenes are also extensively used in several biomedical applications such as antiviral agents, MRI contrast agents and X-ray contrast agents, as well as in photodynamic therapy and drug and gene delivery [45].

2.1.4 Carbon nanotubes

The discovery of carbon nanotubes (CNTs) was reported by Iijima in 1991 and received great attention in the light of the ongoing fullerene research [2]. CNTs can be described as cylindrical nanostructures which

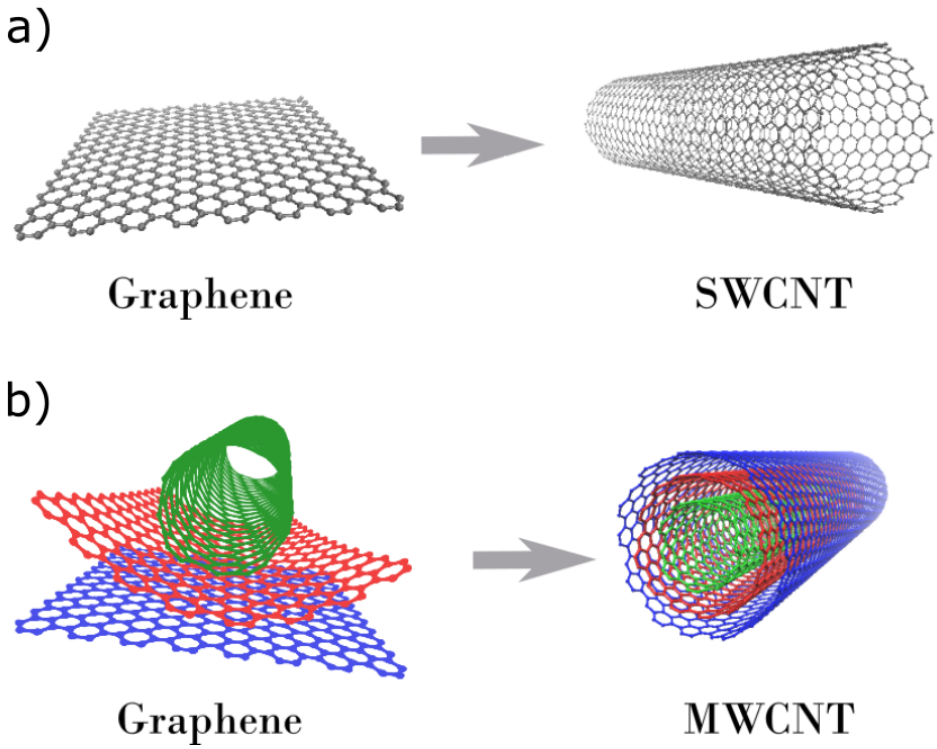

Figure 2.5: **Theoretical construction of carbon nanotubes.** (a) Single-walled carbon nanotube (SWCNT) and (b) multi-walled carbon nanotube (MWCNT) made from rolled-up graphene. The image was created by using VMD software.

consist of graphene sheets rolled up along a specific crystallographic direction. CNTs can vary by the number of graphene layers in their side walls. If the nanostructure is made up of single-layer graphene, it is called SWCNT, while if it consists of several concentric graphene layers the resulting nanostructure is known as multi-walled carbon nanotube (MWCNT) as schematically illustrated in figures 2.5 (a) and (b).

The specific wrapping direction of the nanotube is characterized by chiral vector $\vec{C}_h$ as shown in figure 2.6. The chiral vector can be expressed as a linear combination of basis vectors:

$$\vec{C}_h = n\vec{a}_1 + m\vec{a}_2 \ , \tag{2.7}$$

where $(\vec{a}_1,\ \vec{a}_2)$ are the unit vectors of the hexagonal lattice and n and m

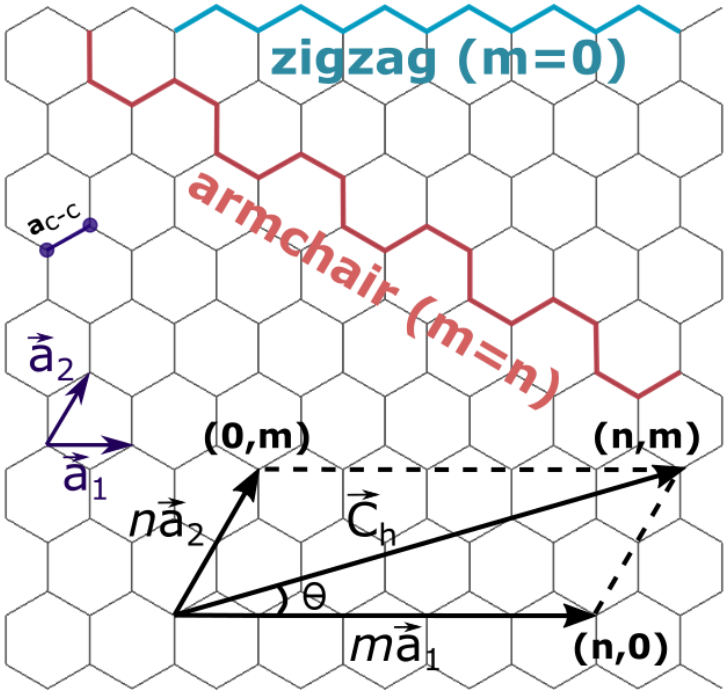

Figure 2.6: Schematic illustration of ideal graphene sheet and parameters required to define nanotube structures. $\vec{C}_h$ is the chiral vector, θ is chiral angle, $\vec{a}_1$ and $\vec{a}_2$ are the lattice vectors and a_{c-c} is the carbon-carbon bond length. The orientation of the carbon network in zigzag (n, 0) and armchair (n, n) carbon nanotubes are highlighted with blue and red lines.

are integers, also known as the chiral indices of the nanotube. These hexagonal basis vectors can be used to uniquely describe a nanotube using the (n, m) coefficients of the chiral vector, $\vec{C}_h$. The chiral angle θ is defined as the angle between the chiral vector $\vec{C}_h$ and the zigzag direction where θ=0. The chiral vector is perpendicular to the axis of the nanotube and has a magnitude equal to the circumference of the tube. The diameter, D, of the tube, hence, is determined by dividing the magnitude of $\vec{C}_h$ by π.

$$D = \frac{|\vec{C}_h|}{\pi} = \frac{a_{c-c}\sqrt{3(n^2 + nm + m^2)}}{\pi}\,, \tag{2.8}$$

where a_{c-c} is the C-C bond length (≈1.42 Å).

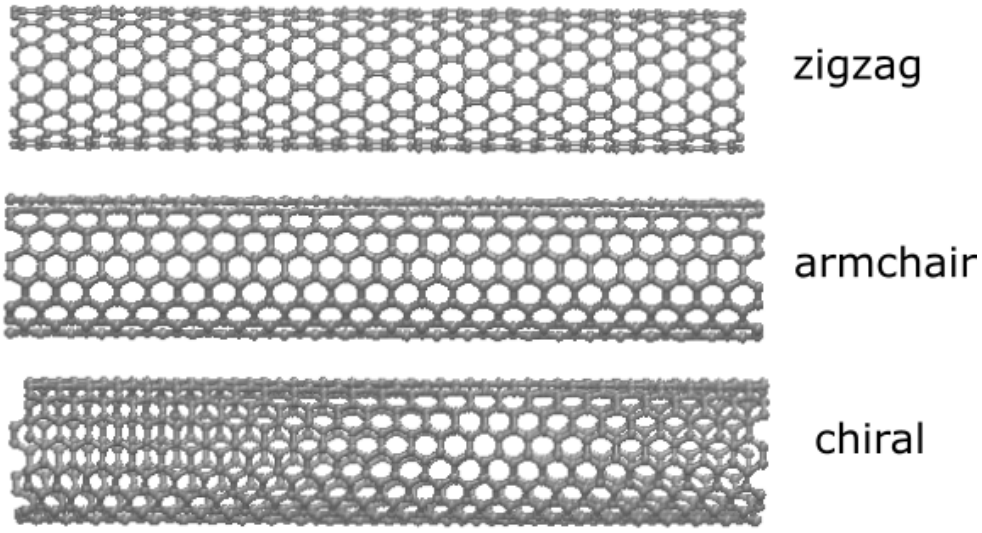

Figure 2.7: Schematic representation of three structural models of SWCNTs: zigzag, armchair and chiral. The images are obtained by using VMD software.

Chiral vector defines the symmetry of the nanotube and is therefore important in determining the electronic properties of the carbon nanotube (CNT). There are two special cases for the wrapping direction of the nanotubes. One is when n and m are equal and the other is, when either n or m is zero. These nanotubes are called armchair and zigzag nanotubes, respectively and are classified as achiral CNTs. The names zigzag and armchair are based on the line shape of the cross-sectional ring of the CNTs as shown in figure 2.7. The other types of nanotubes are referred as chiral nanotubes where $n \neq m$. An example of chiral nanotube is depicted graphically in figure 2.7 (bottom image). The zigzag CNTs correspond to chiral angle of θ=0 and armchair CNTs correspond to θ=30° whereas chiral CNTs correspond to 0>θ>30°.

Based on their chirality and diameter, CNTs can have distinctly different electronic properties even though the local chemical bonding between the carbon atoms in different tubes remains the same. Depending on their structural type nanotubes can be either metallic or semiconducting [46], [47], [48]. This fact originates from the peculiar band structure of graphene. Armchair CNTs are always metallic; due to the finite density of states at the Fermi level. Zigzag and chiral CNTs can be semiconducting or metallic. The band structure of a semiconducting CNT exhibits a very small band gap with a zero density of states (DOS) inside the gap

because of the modest degree of sp^2 to sp^3 hybridization caused by the non-flat shape of the hexagons on the nanotube walls. Metallic CNTs have n-m=3p and semiconducting CNTs have n-m≠3p where p is an integer. This variety opens a way to many different applications. For example, semiconducting SWCNTs have been used in field-effect transistor based sensors [49], whereas metallic conducting MWCNTs have been used as electrodes for electrocatalysis [50].

The outstanding properties of CNTs include high tensile strength and stiffness, electrical and thermal conductivity , and their ability to establish interaction with organic and inorganic compounds [51], [52], [53], [54], [55], [56]. CNTs have been extensively applied in the design of electrodes and showed enhanced performance when compared to traditional carbon surfaces. Some SWCNTs have also been reported to exhibit superconductivity [57].

2.1.5 Van der Waals heterostructures

The family of carbon nanomaterials has been at the center of materials research for more than a decade owing to their outstanding features. Speaking of which, the three most well-known sp^2 nanocarbons, fullerenes, carbon nanotubes and graphene triggered tremendous interest among both science and technology communities [58], [59]. Especially the discovery of graphene, gave rise to a new field of materials research, so called 2D materials. With the rapid development of this field, much more layered 2D materials with novel and unique properties in comparison to their bulk counterparts have been discovered and reported.

Nowadays, 2D materials are a big family of materials encompassing insulators, semiconductors, semimetals, ferromagnets and even superconductors making them promising materials in a wide variety of applications [60], [61]. Moreover heterostructures, made by stacking different 2D layered materials on top of each other, known as the *van der Waals heterostructures*, exhibit novel electrical, optical, magnetic and photoelectric properties, providing a platform to explore the new physics not observable in conventional materials and develop novel devices with tailored functionality. These 2D materials have been fabricated either by transferring prepared layers onto a base layer or synthesizing the layers on the base substrate. While strong in-plane covalent bonds are responsible for the planar stability of vdW heterostructures, these materials are called *van der Waals heterostructures* because the 2D layers are not bonded through chemical reaction but rather attached to each other via so called weak vdW forces including interaction of electrostatic dipoles

(Debye forces) and London dispersion forces [5]. These interlayer forces are associated with bond energies ranging between 40 and 70 meV and are much smaller compared to covalent bond energies of 200-600 meV [62].

vdW interactions are not limited to interlayer bonding in 2D layered materials. Any passivated, chemically inert, dangling-bond-free surface can interact with another by vdW forces. Hence, 2D materials can be combined with an array of different materials of different dimensionality via vdW forces to form *mixed-dimensional* vdW *heterostructures* [6]. The emergence of such materials with mixed-dimensionality of 2D + nD (n=0, 1, and 3) is broadening the family of vdW heterostructures and offers a new platform for fundamental studies and applied technologies such as transistors, photodetectors and photovoltaics. For instance, one of the potential implementation of 2D-1D and 2D- 0D nanostructures can be for catalyst and gas-sensing applications, since these heterostructures present a large surface to volume ratio resulting in significant density of active sites for chemical interactions.

2.2 Experimental Methods

2.2.1 Electron Microscopy

Optical microscopes, also called light microscopes, use visible light as a source of illumination. For any optical system, the theoretical diffraction resolution limit, d_r, is defined by the Rayleigh criterion which describes the smallest resolvable distance between two points:

$$d_r = 0.61\frac{\lambda}{NA} \ , \tag{2.9}$$

where λ is the wavelength of illumination, and NA is the objective numerical aperture. According to this criterion the resolution of a light microscope is theoretically limited to approximately one-half the wavelength of visible light ($\sim$ 200 nm). For imaging of nanoscale materials this resolution is not sufficient and one can not for instance distinguish a single nanotube from two adhering to each other, since they have diameters less than 100 nm. To achieve higher resolutions, illumination with smaller wavelengths is needed. In contrast to the light microscope, the electron microscope uses electron beam with a wavelength far less than visible light as the source of illumination.

The wave-like characteristics of electrons were first postulated in 1924

by Louis de Broglie. De Broglie defined the wavelength of a particle with the equation

$$\lambda = \frac{h}{p} \ , \tag{2.10}$$

where λ and p are respectively the wavelength and the momentum of the particle and h is the Planck constant [63]. Applying the de Broglie equation to an electron we obtain

$$\lambda_e = \frac{h}{\sqrt{2m_e E_b}} \ , \tag{2.11}$$

where λ_e is the wavelength of electron, m_e is the rest mass of electron and E_b is the energy of the electron beam. The electron's rest energy is

$$E_e = m_e c^2 \ , \tag{2.12}$$

which is equivalent to 511 keV. If an electron at rest with a charge q_e is accelerated by an electrical potential U, to the electron beam energy given as

$$E_b = q_e U \ , \tag{2.13}$$

it will have a theoretical wavelength of ≈1.2 pm at 100 keV. However, at the acceleration voltages used in TEM and STEM, relativistic effects have to be taken into account, which gives

$$\lambda_e = \frac{h}{\sqrt{2m_e q_e U(1 + \frac{q_e U}{2m_e c^2})}} \ , \tag{2.14}$$

which corresponds to electron's relativistic wavelength of $\approx 3.7\ pm$ at 100 keV beam energy, which is far lower than the wavelength of visible light ($\sim$ 400-750 nm).

Shortly after De Broglie's postulate, H. Busch revealed that an electromagnetic field might act as a focusing lens on electrons [64]. Not long after this discovery, the idea of using electrons as the source of imaging in a microscope was introduced by Ernst Ruska. In 1931, together with Knoll, Ruska built the first electron microscope by applying the theory of visible light to electron optics for which he was awarded the Nobel Prize in Physics in 1986 [65]. Since then, the constant progress in manufacture processes and electron optics has led to modern electron microscopes which are now capable of imaging the structure of matter in the atomic level. The electron microscopy opened new horizons to

visualize materials and structures far below the resolution limit reached in optical microscopy.

2.2.2 Transmission Electron Microscopy (TEM)

TEM is a powerful instrument used to study the structure, composition, and properties of specimens in sub-micron detail. The main components of TEM consist of an electron gun, a series of electromagnetic lenses and a detector. Figure 2.8 shows schematically the basic outline of TEM along with electron ray diagram. Electrons are generated in electron gun by either thermionic or field effect emission. The emitted electrons are then accelerated with the application of high voltage. The acceleration voltage values in a TEM typically range from 60 kV to 300 kV [66]. After emission from the gun, accelerated electrons pass through condenser lenses which control the spot size and convergence angle of the beam. The next set of electromagnetic lenses are objective lenses which are used to focus the beam onto the very thin sample (<100 nm) and to form initial inverted image of the sample. The sample is located between two objective lenses. Electrons transmitted through the sample finally pass through the projector lenses which magnify and project the image of the sample or its diffraction pattern (which is formed in the back focal plane of the objective lens) onto the detector.

Electrons may interact with a sample in various ways which can provide many useful information about the sample. Figure 2.9 depicts schematically the various interactions that can occur when electron beam is incident on a specimen. These interactions can be broadly categorized as forward and back scattered electrons based on the angle of outgoing electron rays. TEM techniques mainly rely on forward scattered electrons, which include elastic scattering and inelastic scattering. Elastically scattered electrons conserve their initial kinetic energy (or the energy loss is negligible) whereas inelastically scattered electrons undergo an energy exchange which can be detected in microscope. Elastic scattering mainly involves interactions with atomic nuclei and is typically used for obtaining information mainly on the structure of the sample i.e. diffraction pattern and in ADF imaging in STEM. Electron diffraction is an important technique that occurs as a result of elastically scattered electrons when they enter a periodic atomic structure. Inelastic scattering occurs mainly from electron-electron interactions and produces a wide variety of information of the sample such as chemical composition, electronic excitations, plasmons, phonons, interband transition of valence electrons. The technique that employs inelastically scattered electrons for chemical

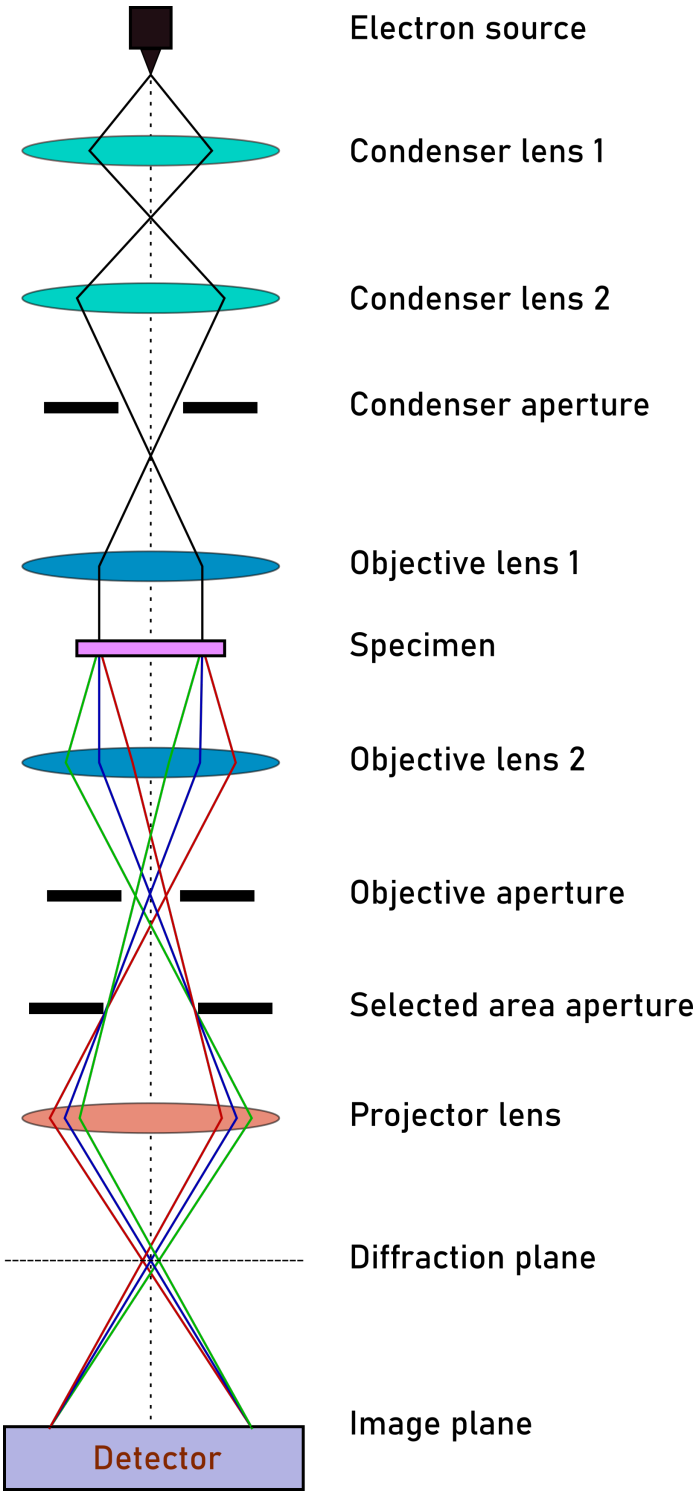

Figure 2.8: A schematic of a transmission electron microscope and its major components.

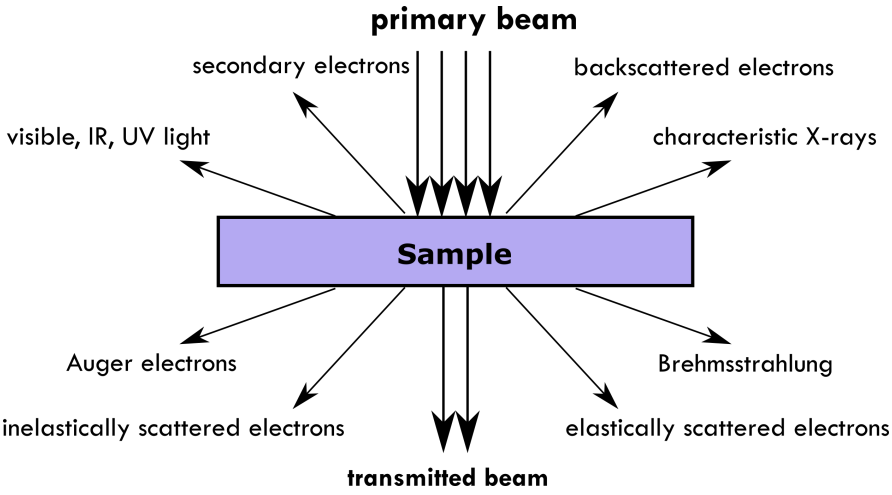

Figure 2.9: Types of interactions between incident electrons and a sample

analysis is known as electron energy loss spectroscopy (EELS).

The main limitation in electron optics in TEM is not the wavelength of the illumination source but the presence of aberrations known as *spherical aberration (C_s)* and *chromatic aberration (C_c)* which results in blurred image and hence a reduced spatial resolution. These aberrations occur due to the deviation of the electrons from their ideal trajectory. In case of C_s the electrons far from the optical axis are focused more strongly than those travelling closer to the optical axis which as a result produces an undefined focal point. Spherical aberration can be quantified by using the collection semiangle of the electromagnetic lens, θ and the coefficient of the spherical aberration, C_{sph}. The radius of the spherical aberration disc, which is also known as disc of least confusion, r_{sph}, is described by

$$r_{sph} = C_{sph}\theta^3 \ . \tag{2.15}$$

Due to this relation C_s is also referred as the third-order spherical aberration and is the most well-known aberration because it was the dominant aberration before correction became possible [67].

C_c arises due to the energy spread of the emitted electrons: electrons with lower kinetic energy are focused more strongly than those with higher kinetic energy which again causes different rays to converge to different points. As in the case of spherical aberration, the disc of confusion in chromatic aberration, r_{chr}, is given by

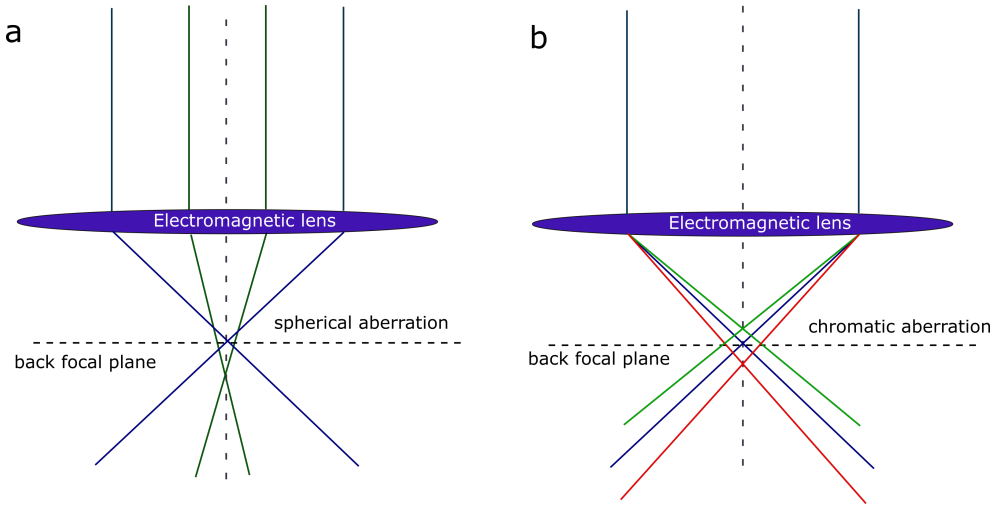

Figure 2.10: **Electromagnetic lens aberrations.** (a) Spherical aberration occurring due to more strongly scattering of off-axial electrons than paraxial ones. (b) Chromatic aberration where electrons of different energies are focused at different focal points.

$$r_{chr} = C_{chr}\theta\frac{\Delta E}{E_0} \ , \tag{2.16}$$

where C_{chr} is the chromatic aberration coefficient, E_0 is the energy of the incident electron beam and ΔE describes the energy loss [68]. in TEM C_c becomes more pronounced for thicker samples, since ΔE is directly proportional with thickness of the specimen. A schematic illustration of spherical and chromatic aberrations is presented in figure 2.10.

The problem of aberrations in electron optics was first addressed by Otto Scherzer in 1936 in his famous publication on the aberrations of electrons that is usually referred as *"Scherzer theorem"* [69]. It states that any electron lens having a rotational symmetry will always have a positive C_s and C_c. Later in 1947, Scherzer proposed a route to correct the C_s and C_c [70]. To overcome these aberrations a non-rotationally symmetric (or non-cylindrical) lenses in TEM were developed and tested for a long time before their successful application in 1990s [71], [72]. A C_s corrector compensates the intrinsic positive C_s by producing a negative C_s by using multi-pole lenses in series with the objective lens. The correction is achieved by either a set of quadrupole and octupole lenses or a set of

hexapole lenses. Another type of aberration in a TEM is *astigmatism* which occurs when electrons pass through a non-uniform magnetic field as they travel down in a microscope column in a spiral path. It can be described as

$$r_{ast} = \Delta f \theta \ , \tag{2.17}$$

where r_{ast} is the disc of confusion for astigmatic aberration and Δf is the maximum focus difference caused by the astigmatism. This phenomenon mainly arises due to the imperfections in the symmetry of lens pole pieces and inhomogeneities in their microstructure [68]. Fortunately, astigmatism can be easily corrected by using stigmators. It is achieved by the small octopoles that create compensating field to cancel out the imperfections in the lens that gives rise to astigmatism. Remarkable improvements of aberration correction in electron optics is one of the most significant improvements in the history of electron microscopy which led to the development of modern electron microscopes with high spatial resolution.

In this thesis the TEM imaging and electron diffraction patterns were obtained by using a low voltage Delong LVEM-5 bench-top transmission electron microscope (or "mini TEM") operated at 5 kV.

2.2.3 Scanning Transmission Electron Microscopy (STEM)

STEM is a very powerful characterization tool for detecting the structure of nanomaterials with high spatial resolution, as well as providing information related to their chemical composition and electronic structure. As with TEM, in STEM electrons pass through a sufficiently thin, electron-transparent specimen. Some components of TEM is also common to STEM such as electron source, electromagnetic lenses, apertures and detectors. The main difference between the two, is that in TEM the parallel electron beam is spread on the sample over the whole area of interest, whereas in STEM the beam is focused into a tiny, convergent electron probe and then scanned point by point across the sample. In STEM the transmitted electrons are recorded at each point and the image is acquired pixel by pixel by correlating the detected signal to the probe position [68]. The scanning of the probe over the desired field of view (FOV) is achieved by scan coils. Due to the scanning motion the image acquisition in STEM is slower than in TEM. The spatial resolution of STEM is governed by the size of the electron probe on the

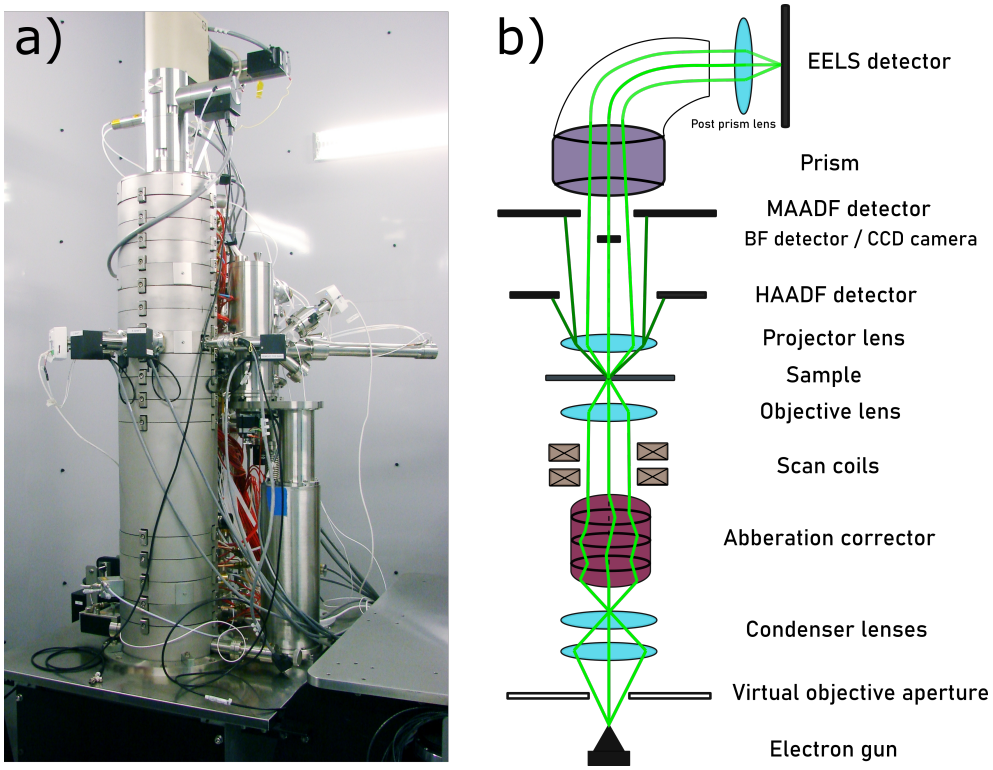

Figure 2.11: A schematic diagram showing the main components of STEM with an electron source at the base.

sample which, in aberration-corrected STEMs, can be well below 1 Å, sufficient to resolve inter-atomic distances in most crystal structures [73]. Similar to high-resolution TEM instruments, STEMs are sensitive instruments that operate in ultra-high vacuum (UHV) condition and require exceptionally stable room environments with limited level of mechanical vibration, temperature fluctuations, and electromagnetic waves [74].

Dedicated STEM devices have rather different set-up than conventional TEM such that in STEM the gun is located at the bottom of the microscope in order to improve mechanical stability. Figure 2.11 shows an image of a dedicated STEM and simplified schematic diagram of the instrument, including only the most important components. The STEM microscope shown is a Nion UltraSTEM 100, which is the microscope used for imaging in this thesis. In a STEM electrons are usually generated from a cold field emission gun (CFEG) which is preferred in STEM because it provides more monochromatic emission from a very small area. The accelerated electrons are then finely focused into a small spot incident upon a specimen by condenser lenses and an objective lens.

An objective aperture is used to limit the maximum angle of illumination included in the incident beam in order to minimize the effects of the aberrations. The sample is scanned over the desired FOV by scan coils. As the electrons leave the specimen, no additional optical element is required for imaging therefore post specimen objective and projector lenses play only a minor role in STEM image acquisition. Here various different detectors are used to collect the wide range of possible signals. To form an image in STEM two common detectors are used which are bright field (BF) detector, and annular dark field (ADF) detector, the latter being used more often. BF detector is a circular detector centred on the optical axis and collects transmitted electrons including electrons scattered at relatively low angles with respect to the optical axis (smaller than the probe convergence angle). BF mode produces principally phase contrast images similar to TEM.

The ADF detector is a ring-shaped scintillator-photomultiplier with a circular hole at the center to exclude unscattered electrons. It collects the electrons that are deflected further away from the optical axis, usually scattered at angles several times the probe convergence angle [67]. Transmitted electrons that pass through the ADF detector's hole enter either to BF detector or EELS section.There are commonly two types of ADF detectors depending on their angular selection of the scattered signal (i.e annular geometry of the detector): medium angle annular dark field (MAADF) and high angle annular dark field (HAADF) detector. Different mechanisms contribute to the signals arriving at each detector yielding different and complementary views of the sample. In MAADF image mode, coherently scattered electrons (or Bragg scattering) at medium angles play a significant role in overall detected signal [73]. In HAADF image mode, electrons scattered inelastically at high angles are the main source of the recorded signal. High angle scattering occurs due to incoherent, Rutherford scattering of electrons by the atomic nuclei. This type of scattering depends strongly on the atomic number (Z) of the scattering atom, meaning that for heavier atoms electrons are scattered to higher angles. HAADF imaging is often referred to as Z-contrast imaging because the intensity of the image is proportional to atomic number and can be interpreted directly in terms of crystal structure.

The advances in STEM imaging have been quite dramatic in the past few years. The ability of aberration-corrected electron microscopes to image nanostructures in the atomic scale more clearly than ever is significantly increasing the demand for these invaluable instruments.

In this thesis work, most of the results were obtained using the state

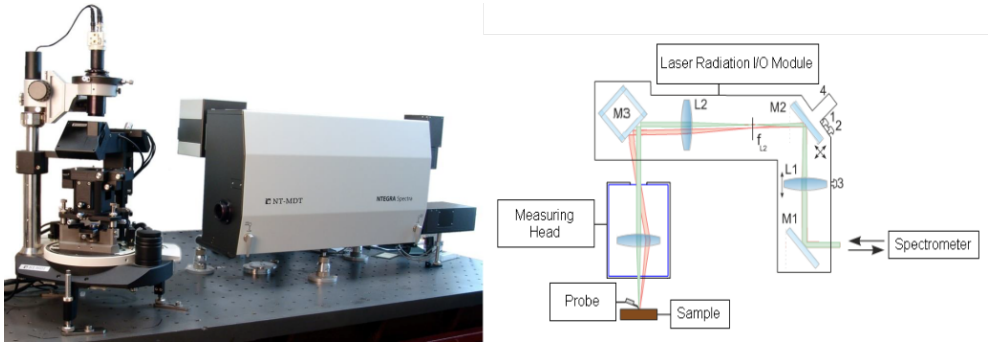

Figure 2.12: NT-MDT Raman instrument and its schematic optical setup. Image is adapted from the instrument's manual.

of the art, dedicated STEM, Nion UltraSTEM100, which was installed in 2013 in Vienna. The image in Figure 2.11(a) shows this instrument in the configuration as it was installed. The UltraSTEM100 is equipped with HAADF and MAADF detectors, an EELS spectrometer, and a charge-coupled device (CCD) camera in direct beam direction. It employs a 100 kV cold field emission gun CFEG as an electron source, providing high brightness and typical energy width of only 0.3 eV in electron emission. Acceleration voltage values range between 40 kV and 100 kV. It is also equipped with a 3^{rd} generation C_3/C_5 aberration corrector which corrects all the geometrical aberrations up to the 5^{th} order. The probe size is about 1 Å at 30 pA beam current, ensuring high spatial resolution on the atomic scale. The experiments in this work were operated with 60 keV primary electron beam energy with near UHV around 10^{-7} Pa at the vicinity of the sample. The angular range of the MAADF detector was 60-200 mrad and the illumination semi-angle of the incident e-beam was 35 mrad. A fully detailed description of the Nion UltraSTEM can be found in ref. [75].

2.2.4 Raman Spectroscopy

Raman spectroscopy is a powerful analytical technique based on the inelastic scattering of light by matter that is widely used for the identification of vibrational modes of materials. It was experimentally first discovered in 1928 by C. V. Raman who observed a frequency shift in the spectrum of scattered light compared to the incident light [76]. He was awarded the Nobel prize in Physics in 1930 for this discovery.

Raman spectroscopy is a versatile, non-destructive, easy-to-use tool that does not require any specific sample preparation and is usually car-

ried out in ambient conditions. In a typical Raman setup, the surface of the sample is exposed to monochromatic light, usually a laser light in the visible range, and the scattered light intensity is recorded as a function of inverse wavelength or wave-number. When a sample is illuminated by a monochromatic laser, the large majority of the incident photons are scattered elastically, which is known as Rayleigh scattering. A very small fraction of the incident photons, however, scatter inelastically due to the interaction and energy exchange between photons and vibrational quantum states of the matter (phonons); this is known as the Raman scattering or Raman effect. In Raman scattering, a phonon can either be emitted resulting in energy loss (Stokes scattering) or absorbed resulting in energy gain for the scattered photon (anti-Stokes scattering). In both cases, the energy shift (or Raman shift) between the incident photon and scattered photon is equivalent to the vibrational state of the sample. The vibrational states, or phonons, are quantized and unique for each material, therefore the Raman spectrum is commonly interpreted as a distinct structural fingerprint by which material can be identified. Moreover, Raman spectroscopy can be used to determine many other properties that may affect the vibrational states of the studied material, such as chemical doping, structural defect/disorder, isotope ratios, temperature, mechanical deformation, stress/strain, crystallinity, electronic doping and impurity. The spectral resolution of a Raman spectrometer is defined by the spot size of the laser, which is typically in the order of 0.4-1 μm.

The micro Raman spectroscopy presented in this thesis were measured using a NT-MDT NTEGRA Raman Spectrometer in backscattering geometry equipped with diode pumped blue solid-state laser with 473 nm excitation wavelength (2.62 eV). An image schematic of optical setup of the instrument is shown in Figure 2.12. The output laser power was $\sim$4 mW over a focused spot size of $\sim$0.5 μm (100$\times$ objective, NA=0.7) under ambient conditions. The laser can be moved laterally on the sample surface in $x-y$ directions via a mirror mounted onto a second piezo tube in the illumination beam path. The sample is placed on a movable stage which is a motorized $x-y$ positioner that is used to focus the laser spot on the required position.

The Raman spectrum contains various peaks corresponding to specific vibrational modes. These peaks are characterized by the peak position, full width at half maximum (FWHM), and peak intensity with respect to other peaks. Figure 2.13 shows an example of Raman spectrum on mixed-dimensional heterostructure. The sample presented here consists of free-standing 2D monolayer graphene deposited with 1D C_{60} fullerene

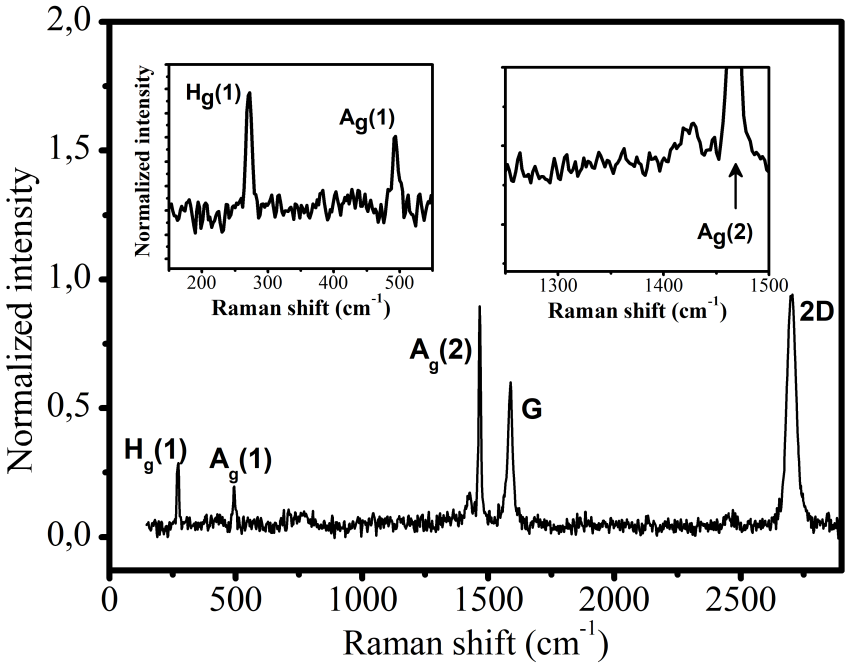

Figure 2.13: Raman spectra of C_{60} fullerene deposited on monolayer graphene. The insets highlight the C_{60} modes.

molecules. The Raman spectra was obtained from an arbitrary location on the sample. The main features of graphene's Raman spectrum are the G peak at ∼1584 cm^{-1} and the 2D peak at ∼2700 cm^{-1}. The G peak is common to all graphitic sp^2-bonded carbon materials and originates from doubly-degenerate E_{2g} phonons at the Γ points in the Brillouin zone and corresponds to in plane stretching of carbon-carbon bonds [77]. 2D peak occurs due to the second order double resonance scattering of the phonons at K and K' points of the Brillouin zone. Another Raman peak that can be detected in graphene's Raman spectra at ∼1340 cm^{-1} is the so called disorder or defect mode (D mode), originating from the second order Raman scattering through the inter-valley double resonance process. This mode occurs when graphene's lattice symmetry is broken by structural defects in the lattice. The absence of the D peak represents high crystallinity of graphene [78]. In our sample the D mode is hardly detectable, indicating high crystallinity.

In this example spectra, three significant C_{60} vibrational modes are detected; $H_g(1)$ squashing mode at ∼273 cm^{-1}, $A_g(1)$ breathing mode at ∼497 cm^{-1}, and the most prominent $A_g(2)$ pentagonal pinch mode at ∼1469 cm^{-1}. These three main vibrational modes of C_{60} are illus-

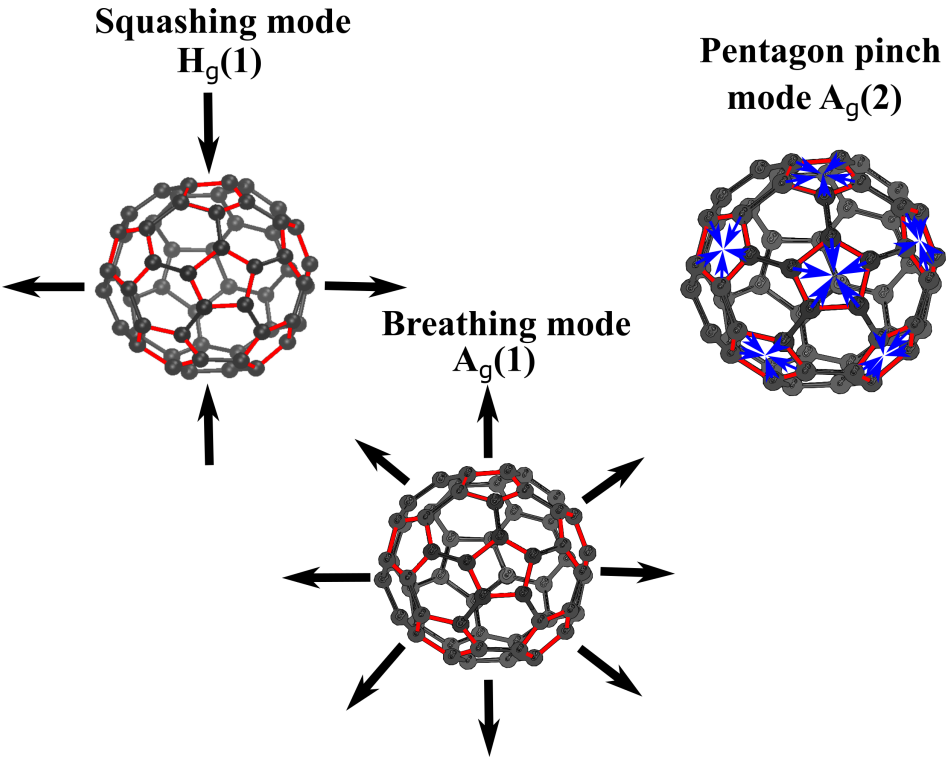

Figure 2.14: **Vibrational modes of C_{60} molecule.** $H_g(1)$ squashing mode, $A_g(2)$ pentagon pinch mode and $A_g(1)$ breathing mode.

trated in figure 2.14. The squashing mode ($H_g(1)$) deforms the spherical C_{60} molecule into a rugby ball shape and back to spherical shape again by expanding and contracting it on the opposite poles and simultaneously squeezing and enlarging at the central circumference (see figure 2.14a). The $A_g(1)$ mode, is a "radial breathing" mode of C_{60} molecules, expanding and contracting the whole C_{60} molecule (figure 2.14b). The pentagonal pinch mode is a tangential displacement mode in which all pentagons on the molecule are "breathing" caused by contraction and expansion of pentagonal rings in C_{60} (figure 2.14c). The $A_g(2)$ mode is widely used as an analytical probe to determine the structural and electronical properties of C_{60} [79].

2.3 Sample Preparation

In this section the fabrication method of 2D-0D mixed-dimensional graphene fullerene sandwich vdW heterostructure is presented. The sample fabrication is a multi-step process including respectively the production of

monolayer graphene, the C_{60} deposition, and addition of another layer of graphene on top of the deposited C_{60} which results in a sandwich structure.

Most of the graphene samples used in our experiments were commercially available chemical vapour deposition (CVD) grown monolayer graphene membranes on holey carbon support films (Quantifoil®) coated on TEM grids purchased from Graphenea Inc. Home-grown CVD graphene monolayers were also used in the encapsulation process, however due to contamination issue they could not be characterized properly. Nevertheless, I would like to mention this method as an alternative sandwiching technique.

2.3.1 Synthesis of Graphene via Chemical Vapour Deposition (CVD)

Chemical vapour deposition (CVD) is a process of depositing thin films on a suitable substrate surface via chemical reaction of precursor gases. So far CVD technique is the most common and large-scale fabrication method for graphene and for many other 2D materials [80]. A typical research-scale CVD reactor mainly consists of a cylindrical hollow tube furnace with a quartz tube installed at its center and a gas flow control system as illustrated in figure 2.15. The quartz tube is attached to a vacuum pump from one end and gas inlet system from the other. In graphene growth, a metal substrate is placed in the quartz tube and the volume is evacuated before the carrier gas consisting of a mixture of Ar and H_2 gases enters the quartz tube. The furnace is then heated until the set temperature and carbon precursor gas methane (CH_4) is allowed

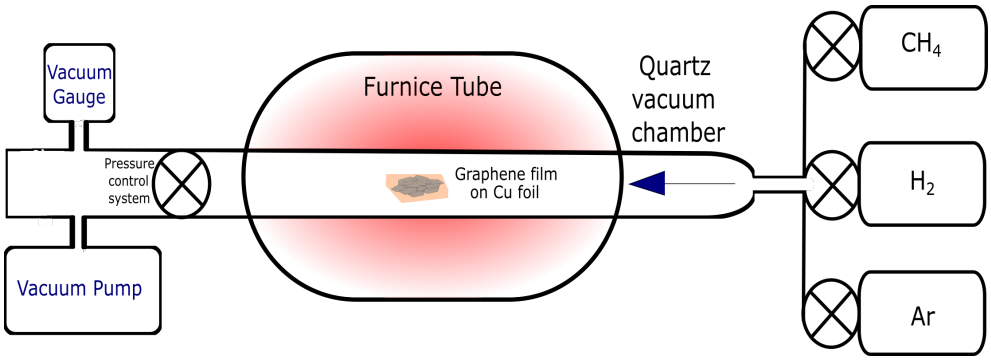

Figure 2.15: Schematic illustration of chemical vapour deposition furnace and its components

to flow into the quartz tube. The nucleation of graphene occurs when CH_4 decomposes into carbon radicals and carbon atoms dissolve onto the metal surface. The graphene films are grown onto a transition metal catalyst, usually copper or nickel.

The home-grown graphene monolayers in our experiments were grown by low-pressure CVD method on Cu substrate. The quartz tube was heated until target temperature of 960 °C and copper foil was annealed for 45 minutes under 2000 sccm $Ar(95\%)/H_2(5\%)$ flow. After pre-annealing process, 50 sccm CH_4 was applied together with 2000 sccm Ar/H_2 for 7 minutes. The base pressure of the quartz tube inside the furnace was 2×10^{-2} mbar.

2.3.2 Deposition of C_{60} molecules

In this work, the C_{60} molecules were deposited on the commercially purchased monolayer graphene samples from Graphenea Inc. These samples contain sufficiently clean, high quality monolayer graphene supported by Quantifoil® on Au-coated TEM grid. The grids that we used have a standard diameter of 3mm and contains holes with a diameter in a few micrometer range for suspension of the sample for S/TEM analysis.

The deposition of C_{60} fullerene on graphene was realized by a Mantis Hex deposition system from Korvus Technology. This HEX evaporator device consists of a vacuum chamber, three different deposition sources, a rotating/heating substrate stage on top of the chamber, an electronic control unit and vacuum turbo pump connected to the chamber. It is a versatile and flexible system that allows to deposit thin layers of molecules or atoms under high-vacuum at controlled deposition rate, pressure and temperature. As a deposition source it is equipped with magnetron sputtering source, an e-beam evaporator and a thermal boat source. In our experiments we used a thermal boat source to grow the C_{60} layers on top of the graphene monolayer suspended over TEM grid by thermal evaporation of crystalline C_{60} powder (Sigma-Aldrich, 99,9% purity). Thermal boat functions with resistive heating achieved by a current passing through a filament in high vacuum with a thermocouple attached to it to measure the temperature. Prior to starting the deposition measurement, the C_{60} powder in a thermo-electric boat was preheated to 200 °C at $\sim10^{-5}$ mbar chamber pressure and degassed for about two hours to remove contamination. After the degassing process, the base pressure in the chamber reached at around 2×10^{-6} mbar. The thermal boat was then heated slowly up to 480-500 °C by increasing the current in filament (during deposition: ∼73 A, (∼0.65 V). The fullerene

molecules were sublimated in high-vacuum ($\sim 10^{-6}$ mbar) at a deposition rate of $\sim$1 Å/s for $\sim$10 seconds. The deposition rate was controlled by a quartz crystal microbalance (QCM) which is used to monitor the amount of evaporated material by measuring the change in frequency of a quartz crystal resonator.

Prior to deposition, the monolayer graphene samples on TEM grids were annealed at 350-400 °C on a hot plate in air for around 30 minutes to remove the contamination. During the degassing process of C_{60} powder, the sample stage containing the TEM grids was heated to 200 °C for 2 hours for further annealing, then cooled to 100 °C and kept at this temperature for the deposition. Deposition is controlled by a shutter between the sample stage and evaporation source by opening and closing it manually when the desired deposition rate is reached. After the deposition, samples were removed from the chamber by venting the vacuum with N_2 atmosphere. No annealing of the samples at high temperatures was carried out after the deposition process.

2.3.3 Preparation of buckyball sandwiches

The final step of the sandwiching process of fullerenes between two graphene sheets was to add another layer of graphene on top of the deposited C_{60}. To do so we tried two methods. Firstly, a second TEM grid with monolayer graphene was placed on top of the C_{60} deposited graphene sample and then the two grids were adhered by a droplet of isopropyl alcohol (IPA) (semiconductor grade PURANAL, Sigma Aldrich). After the evaporation of IPA, the grids were separated from each other with the help of fine-tip tweezers. The sandwiching process was carried out at room temperature.

In this method the suspended sandwich structure could only be found in the regions where two grid holes partially overlap as shown in figure 2.16. Rest of the sample was not useful for characterization. Because the Quantifoil is a very thin, during the separation of grids some part of the foil was damaged or broken. We used both grids to investigate sandwich structures. With this method we successfully fabricated sandwich structures suspended on overlapping Quantifoil holes in both TEM grids and confirmed the new structure by several characterization methods. One of the main advantages of this method is that the overlapping of holes in Quantifoil makes it possible to easily find the location of the sandwiched regions. Fig 2.16 shows a TEM image of sandwiched structure in partially overlapping holes.

Most of the results shown in this thesis are obtained from the samples

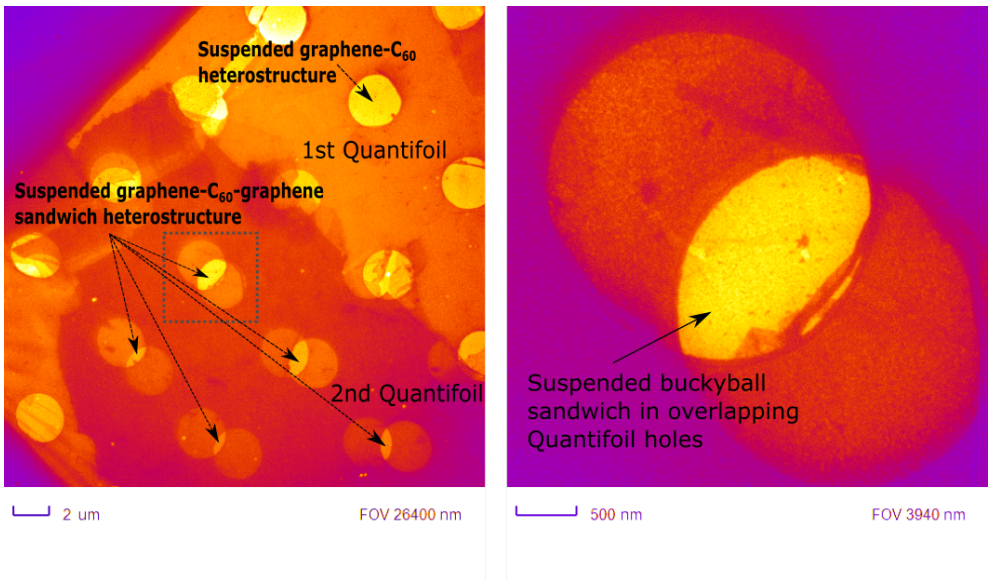

Figure 2.16: (a) Overview TEM image of sandwiched sample on a TEM grid and (b) magnified image of the selected area in dashed rectangle in panel a) showing the overlapping grid holes where the sandwich structure is formed. To enhance the contrast of the images ImageJ lookup table "Fire" was applied.

produced with this method. We also prepared and characterized C_{60} deposited monolayer graphene samples without sandwiching to serve as a reference to the sandwiched samples.

The second method we tried, was to fabricate the sandwich structure by adding another layer of graphene by simply transferring home-grown CVD graphene on top of the C_{60} deposited graphene on TEM grid. The transfer of graphene was achieved by polymer free transfer technique. In this technique, graphene grown on Cu foil is put in $FeCl_3$ aqueous solution in order to etch Cu. The free floating graphene flake is then moved using SiO_2/Si chip to de-ionized (DI) water to remove $FeCl_3$ residues and subsequently to IPA for cleaning. Finally the graphene flake is "fished" from IPA by the TEM grid with graphene and C_{60}. In this method most of the Quantifoil holes are expected to be covered by graphene layer resulting in a much larger sandwich area. Though this method seems more efficient and we were indeed able to produce large area sandwich structures, the samples were not clean, and we were not able to obtain high-quality images in STEM experiments. An example of a sample obtained by this method is presented in figure 2.17.

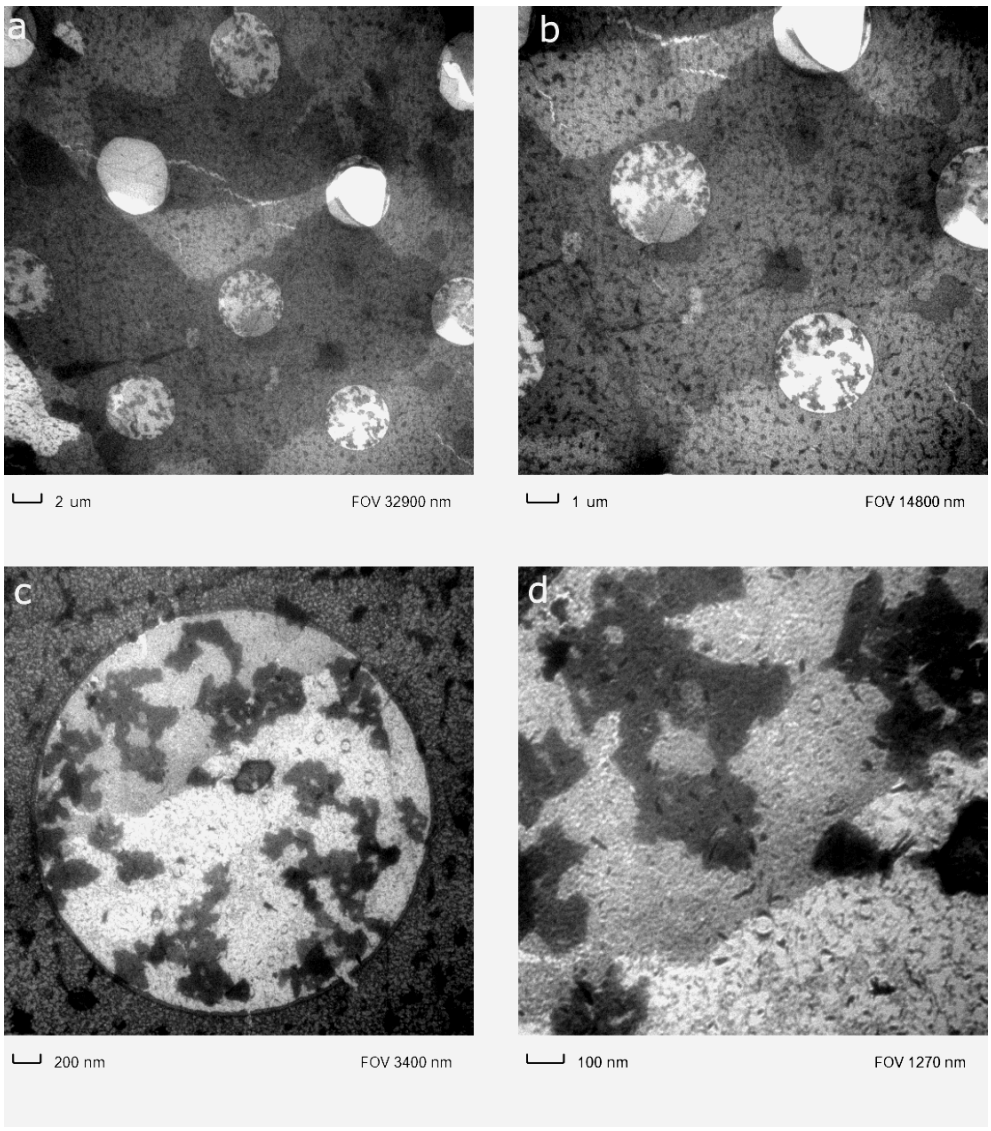

Figure 2.17: a) Overview TEM micrograph of sandwiched sample fabricated by adding a home-grown CVD graphene layer on top of commercially available graphene monolayer coated with C_{60}. (b), (c) and (d) are magnified images of (a).

2.3.4 Preparation of graphene-single walled carbon nanotube heterostructure

The carbon nanotubes were fabricated by using floating catalyst chemical vapour deposition method. For small-diameter tubes, carbon monoxide (CO) was used as the carbon precursor, decomposing on *ex-situ*-

generated iron nanoparticles at 880 °C [81]. The carbon nanotubes with larger diameter were fabricated at 1050 °C by ethylene precursor decomposing on nanoparticles formed *in-situ* from ferrocene vapour [82]. The as-fabricated tubes were dry-deposited [83] by thermophoresis directly on commercially available CVD graphene (Graphenea Inc.) suspended on perforated silicon nitride grids (Ted. Pella Inc.). The cleaning of graphene-carbon nanotube structures was carried out by 20 s of laser irradiation at 0.3 W excitation power under 10^{-7} Pa pressure [84]. After the cleaning the samples were transferred to the microscope column within the same vacuum system.

2.4 Atomistic simulations

2.4.1 Simulations used for the study of C_{60}-graphene heterostructure

Most simulations in this work were carried out with the Large-scale Atomic/Molecular Massively Parallel Simulator (LAMMPS) code [85], [86] using an Adaptive Intermolecular Reactive Empirical Bond Order (AIREBO)-potential augmented by a Morse potential for the intermolecular interactions (A-M) used as a pairwise force field to describe the covalent and vdW interactions, respectively [87], [88]. In order to understand the structure of the C_{60} molecular layer sandwiched between graphene monolayers and to study the intermolecular spacing, a model supercell was designed consisting of 7 rows of C_{60} molecules with periodic boundary conditions along the edges of underlying and overlying graphene layers. The misalignment angle between the graphene lattices was set to 11.6°, resulting in a moiré pattern periodicity of ∼12 Å matching the experiment results presented in chapter 3. This unit cell was repeated by 5 and 20 times, resulting in a model supercell consisting of 33820 carbon atoms, including the C_{60} molecules. The total potential energy was minimized by relaxing both layers without constraints until the forces were below 10^{-4} eV/Å. For estimating the C_{60} diffusion barriers, the nudged elastic band method was used with a spring constant of 10 eV/Å.

The obtained results were additionally compared with density functional theory (DFT) calculations for the bulk C_{60} crystals by using two different vdW functionals (C09 and DF2) [89], [90]. We relaxed the minimum single-molecule unit cells of both 3D and 2D FCC structures using the plane wave mode in the GPAW simulation package with 600 eV cutoff energy, and 5×5×1 and 5×5×5 Monkhorst-Pack k-point meshes for

the 2D and 3D cases, respectively.

To study the bonding of the fullerenes, two C_{60} were placed in the center of a 32×20×20 Å unit cell and atomic structure was relaxed by using the C09 functional in the GPAW LCAO mode [91]. To study the effect of irradiation on apparent bond length, first one C atom was removed from the second C_{60} and then the structure was relaxed, and then further another C atom was removed from the first C_{60} and the structure was relaxed again, resulting in both single- and triple-bonded dimers. For the C_{60} - C_{59} system, molecular dynamics simulations were further run in the LCAO DFT mode to simulate the rotation of the C_{59} caused by an electron impact on one of the carbon atoms.

2.4.2 Simulations used for the study of carbon nanotube-graphene heterostructure

Simulations were performed to investigate the adsorption of SWCNTs on both graphene and graphite. The AIREBO potential [88] was employed to describe the covalent bonding in nanotubes and graphene, while vdW interactions were included by augmenting the model with a Morse potential [87]. For the nanotube, the torsion component of the AIREBO potential was turned off since it matched better with the experimental results and the Morse potential parameters were identical to the AIREBO Morse potential [87]. All structural minimization process were performed using the LAMMPS package [85], [86].

For each carbon nanotube, the graphene lattice was oriented so that it commensurates with a single unit cell of the chiral nanotubes, necessary to enforce the periodic boundary conditions along the axis. For the (13, 3) and (30, 5) nanotubes, the rotated graphene unit cell was multiplied perpendicular to the axis respectively by 12 and 28 times. Hence, the total width of graphene for the (13, 3) tube was about 64 nm and for (30, 5) about 66 nm. To match the graphene curvature with the reconstructed results the bounding box of the cell was shrunk respectively by 0.7 and 0.8% for (13, 3) and (30, 5) tubes. The nanotube eccentricity was assigned by comparing the diameters of a relaxed nanotube in vacuum and on the surface.

2.4.3 STEM image simulations

In STEM the image contrast is dominated by the scattered electrons and can be investigated by image simulations. The atomic structure of the specimen can be estimated by evaluating the scattered intensity at

each probe position by calculating the exit wave function. The STEM image simulations can also be used for interpreting the crystal structure of the studied material and for estimating the thickness of layers from the intensity contrast.

The STEM simulations presented in this thesis were performed using 2.31 QSTEM software with chromatic aberration coefficient of 1 mm, a spherical aberration coefficient of 1 μm, an energy spread of 0.48 eV. The MAADF detector angles set to the experimental range of 60-200 mrad and the illumination semi-angle to 35 mrad.

Chapter 3

Results

This chapter is dedicated to the results that were achieved during the course of my thesis work and that were published in peer-reviewed scientific journals. The first section of the chapter (Section 3.1) is devoted to the analysis of buckyball sandwiches and non-sandwiched graphene-C_{60} heterostructure. The second section (Section 3.2) focuses on graphene-single walled carbon nanotube (SWCNT) heterostructure.

3.1 Buckyball Sandwiches

The content of this section is based on the first article of the List of Publications.

Fullerene molecules are usually encapsulated before studying their dynamical properties and mutual bonding by means of transmission electron microscopy [92], [93]. One successful strategy for this aim is to use carbon nanotubes to wrap the C_{60} molecules in a pea-pod-like structure. In carbon pea-pods C_{60} molecules have been studied in a confined and well-defined space inside a nanotube without the need of a suspension [7], [9]. Perhaps, the main drawback of this approach is the constraint of C_{60} molecules along only one spatial dimension. However, C_{60} molecules have also been reported to self-assemble into hexagonally close-packed islands and exhibit epitaxial ordering on graphene and some transition metal substrates [94], [95].

Here, we present the first example of suspended buckyball sandwich structure reported to date, where C_{60} molecules are encapsulated between two graphene monolayers at room temperature. The most interesting and intriguing result of this thesis is the creation of a new organic nanostructure: a monolayer of C_{60} sandwiched in graphene monolayers.

The results presented in this section show that individual fullerene molecules can truly be observed at atomic resolution. Previously, graphene encapsulation has been used to study small metal particles or other 2D material systems by high resolution electron microscopy [96],[97],[98]. Graphene is known to reduce the amount of radiation damage of the encapsulated specimen and provide a sample support with a well-known structure that can be later easily subtracted from the image [97],[98]. Moreover, we found out that graphene sandwiching provides a "clean" view onto the molecules: in sandwiched regions only such contamination was observed that is typical to graphene in TEM imaging, whereas without the sandwiching no clear images of the fullerenes could be obtained. The sandwich further functions as a nanoscale reaction chamber, that provides more degrees of freedom than fullerene cage or a 1D "test tube" inside a carbon nanotube, creating a "petri dish" to investigate the structure and characteristics of the individual molecules trapped between the layers [99],[93].

In this section we first introduce the morphology of the samples followed by analysis of C_{60} multilayers both in sandwiched and non-sandwiched samples. Then we move to detailed study of C_{60} monolayers in sandwich, their dynamics and the interaction between the C_{60} molecules. We utilized STEM, TEM, electron diffraction, and Raman spectroscopy to verify successful sandwiching and to characterize the samples.

3.1.1 Morphology of Samples

Large-scale STEM overview micrographs of C_{60} on graphene and in sandwich structure are shown in figure 3.1 (a) and (b), respectively, observed in Nion UltraSTEM100. In both cases, fullerenes form islands with different shapes, sizes and thicknesses. In these samples, the size of the islands range from a few tens of nanometers up to one hundred nanometers in diameter, while in some other samples larger islands were also observed (up to 500 nm in diameter). From the contrast difference of the presented STEM image we estimated the thicknesses of islands to vary from single up to $\sim$10 layers.

The first confirmation of the sandwich structure is verified by means of electron diffraction pattern (EDP) obtained using LVEM-5. The results are shown in figure 3.2 (a), and (b). The diffraction pattern shown in (a) belongs to non-sandwiched C_{60}-graphene structure and in (b) represents the sandwiched structure. The corner points of the superimposed hexagons drawn by dashed lines on EDPs, corresponds to the alignment

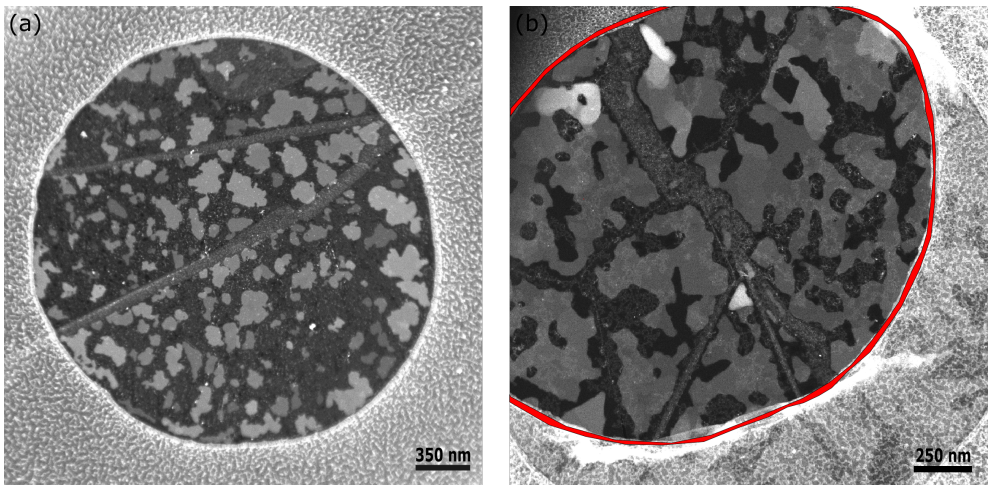

Figure 3.1: **STEM overview images.** (a) STEM micrograph of a graphene monolayer deposited with C_{60} and (b) of a buckyball sandwich. The overlapping holes of the TEM grid support films are highlighted in red.

of the C_{60} crystallites and and the graphene diffraction spots in reciprocal space. The diffraction points emerge from monolayer graphene and deposited C_{60} in figure 3.2 (a) and as expected, from two separate layers of graphene and C_{60} in figure 3.2 (b). The Bravais-Miller indices on some diffraction spots represent the set of planes in hexagonal lattice. The EDP in figure 3.2 (b) also reveal the misalignment of graphene layers. The same triangular symmetry shared by both lattices of graphene and C_{60} crystallites that is depicted in figure 3.2 (c) and (d), allows us to use simple Euclidean geometry to calculate the relative bulk spacing in C_{60} crystallites (the distance between the centers of the neighbouring molecules) with respect to the well-known graphene lattice constant of 2.46 Å. We obtained the same result for C_{60} spacing in both sandwiched and non-sandwiched samples to be 10.4±0.3 Å, which is in good agreement with the previously obtained results of lattice constants in bulk C_{60} crystallites by electron and X-ray diffraction techniques [100], [101], [102]. However, as we show later, the spacing of C_{60} monolayers in sandwich is different.

Raman spectra of both samples given in figure 3.3 provides additional evidence of the sandwiched heterostructure. Here, we compare the prominent Raman features of sandwiched and as-deposited C_{60} crystallites. The main Raman peaks are the pentagonal pinch mode at ∼1469 cm^{-1} (originating from tangential in-phase oscillations of pentagonal rings),

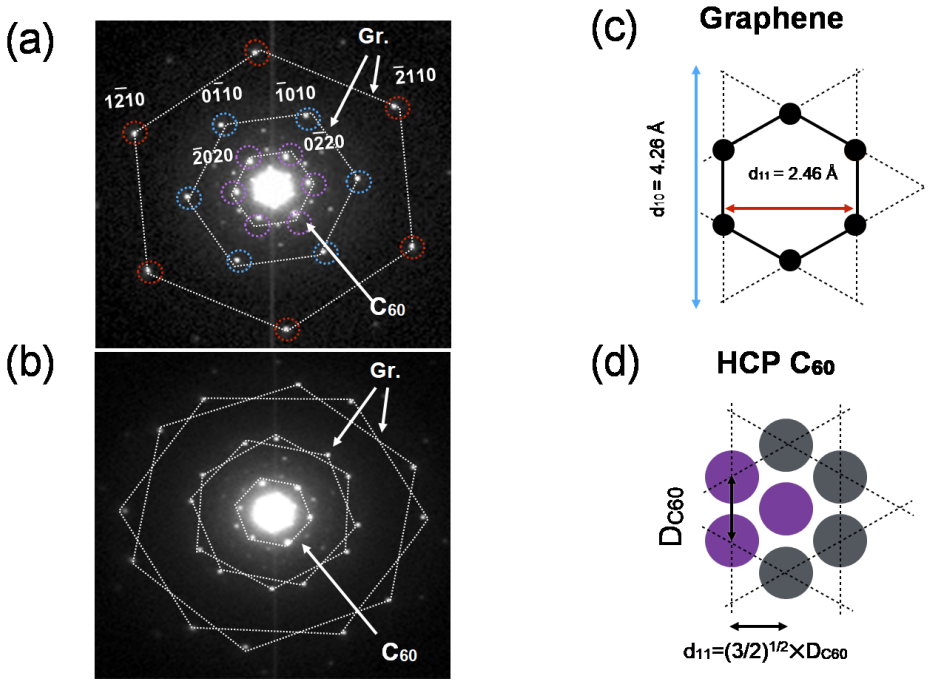

Figure 3.2: (a) Electron diffraction pattern of graphene monolayer deposited with C_{60} and (b) of a sandwich structure, representing an average signal from $\sim 7\times 10^4$ nm^2. The coloured dashed circles denote the Miller-Bravais indices of the diffraction components of graphene (blue and red) and C_{60} (purple). (c) The triangular symmetry of graphene and (d) of C_{60} crystallites. The dashed lines indicate the (111) Bravais lattice planes, and colouring corresponds to the colours in (a) and (b).

the squashing mode at $\sim$273 cm^{-1} (from sphere to rugby ball-like shape oscillations) and breathing mode at $\sim$497 cm^{-1} (corresponding to radial contraction and expansion of molecules). Remarkably, all of these modes of C_{60} were suppressed by adding a sandwiching layer: squashing mode by $\sim$78%, and pentagonal pinch mode by $\sim$72%, while breathing mode, surprisingly, fell below the noise level which is usually more pronounced than breathing mode in suspensions [103].

The Raman modes of graphene were also affected by sandwiching. In figure 3.3, the G mode related to the first order hexagonal lattice vibration appears at $\sim$1580 cm^{-1}, the 2D mode related to second-order vibrations appear at $\sim$2690 cm^{-1}, and the D mode related to defects

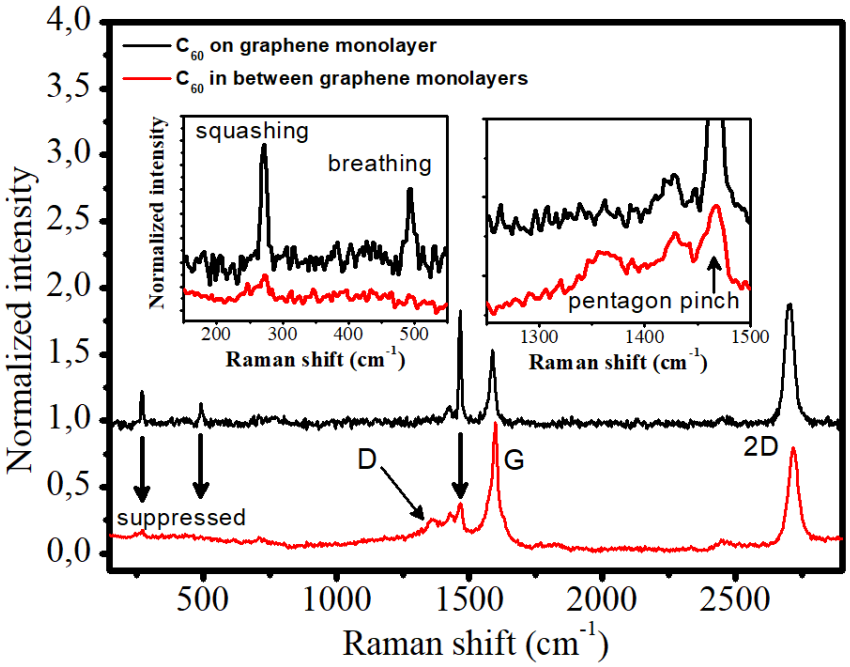

Figure 3.3: Raman spectra of buckyball sandwich denoted by red colour and C_{60} on graphene denoted by black colour. The insets show the C_{60} peaks for both structures in greater detail.

at ∼1360 cm^{-1}. After sandwiching the relative intensity of the G mode becomes pronounced whilst the 2D mode loses relative intensity and dispersed. We observed alteration in the relative intensities of G and 2D modes of graphene. We assume that the dispersion in 2D mode occurred due to the interlayer coupling resulting in the FWHM increasing from 44 to 50 cm^{-1}. The disorder related D mode was detected exclusively in sandwiched graphene layers. Although speculative, we assume the D peak emerges from the structural defects caused by peeling procedure during sample preparation inducing large scale folding and ripping.

3.1.2 C_{60} Multilayers

After the initial characterization of the samples and being confident that we had successfully created sandwich structure, we proceeded to high-resolution STEM. For a more comprehensive assessment of the synthesized structures, we first discuss the observed C_{60} multilayers. It is know that in Euclidean space, the maximum packing density of equal spheres is ∼0.74, which also holds for quasi-spherical C_{60} molecules after taking

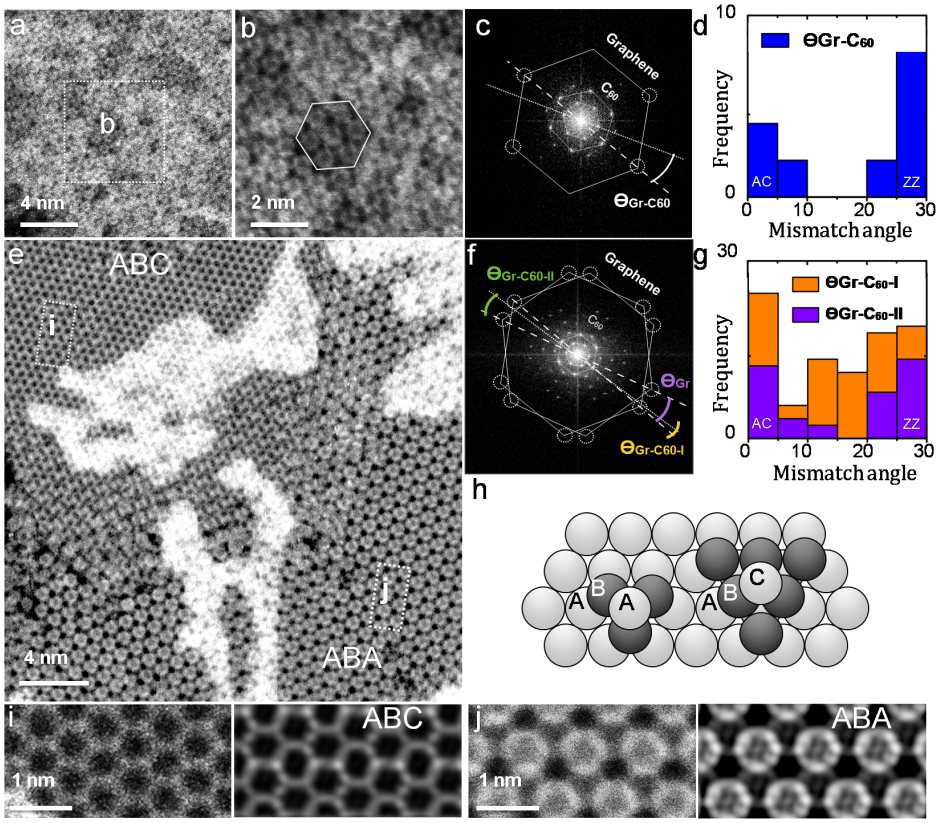

Figure 3.4: **Structure of C_{60} multilayers.** (**a** to **d**) multilayer in non-sandwiched structure, (**e** to **g**) in sandwiched structure. (a) STEM image of a multilayer area covered with carbon contamination. The relatively clean area marked by [b] shown in (b) still contains a disordered amorphous carbon coverage. (c) A Fourier transform of (b) showing the orientation of monolayer the C_{60} and monolayer graphene (111) planes in reciprocal space. (d) Histogram showing the frequency of relative orientation of C_{60} and graphene (111) planes (data gathered from EDPs). (e) Multilayer regions in buckyball sandwich exhibiting two apparent stacking orders. (f) A Fourier transform of (e) showing the orientations of the two graphene monolayers and C_{60}. (g) Stacked histogram plotting the mismatch angle distribution between graphene layers and fullerenes. (h) A schematic demonstration of the ABA and ABC stacking orders. (i) Close-up image of the area marked as [i] in panel (e) indicating a hexagonal pattern that accurately matches with the STEM image simulation of ABC stacking shown on the right. (j) Close-up image of the area marked as [j] in panel (e), precisely matching with the simulated ABA stacking order given on the right. Figure based on Ref. [104].

the vdW diameter into consideration. Denser packing not only provides symmetry, but also minimizes the free surface energy, favouring a certain configuration over others. Lowest-energy packing is achieved by stacking hexagonally close-packed (HCP) monolayers either in an ABA configuration (every second layer being identical) or in an ABC configuration (every fourth layer being identical) as illustrated in figure 3.4 (h). The multilayer regions that we observed all exhibited one of these two patterns.

The analysis of high-resolution STEM images revealed self-assembled, continuous, and well-organized close-packed layers of C_{60} both on monolayer graphene and in sandwiches. For the analysis relatively clean, low-contamination areas were taken into account. Figure 3.4 (a) shows a representative MAADF STEM image taken at FOV of 34×34 nm^2 from non-sandwiched C_{60}-monolayer graphene structure with 4 μs exposure time per pixel. For more detailed view, figure 3.4 (b) shows a higher magnification image from the selected region marked as [b] at FOV of 8×8 nm^2. The small FOVs below 16×16 nm^2 have drawback that often the adjustment of focus was necessary, exposing the lattice to additional electron irradiation. Considering the C_{60} molecules were held in place solely by weak vdW forces, due to the influence of scanning electron probe, and probably also the vibrations, the achievable spatial resolution was relatively poor. Taking images of beam sensitive areas is always a trade-off between spatial resolution and influencing the observed structure. Moreover, the layers were always covered with thin amorphous carbon contamination which is a well-known issue in electron microscopy. Fortunately, we were still able to observe the arrangement of C_{60} structure and discern the round fullerene molecules clearly. The highlighted region 3.4 (b) resembled a layer of HCP molecules with ABA stacking. It should be also noted that, in non-sandwiched samples only multilayers of C_{60} could be observed.

The STEM micrograph representative of the sandwiched multilayers is shown in 3.4 (e). In contrast to non-sandwiched samples, the sandwiched samples exhibited a remarkable beam stability and much clearer contrast, as evident by the image quality in figure 3.4 (e). The improvement in STEM images is attributed to the covering graphene monolayer on top of the C_{60} fullerenes which functions as a protection shield from the e-beam irradiation and provides more stability for fullerenes. As expected, the mobility of fullerenes is constrained in two dimensions in the sandwich structure, hence making C_{60} less mobile under the e-beam, compared to a non-sandwich structure. It is also noteworthy to mention that the perfectly clean regions for STEM imaging could only be found in

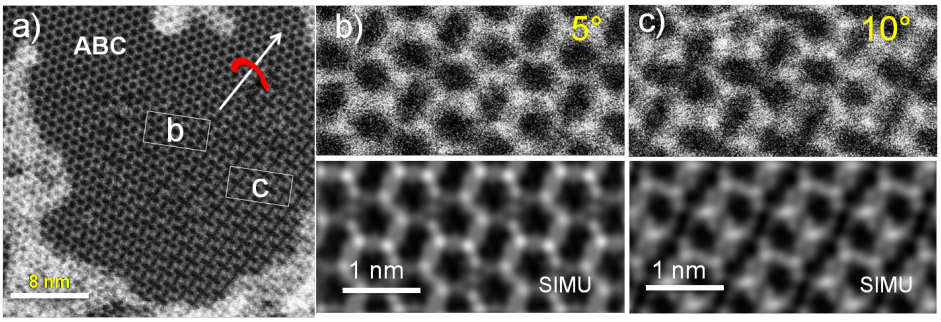

Figure 3.5: **STEM images and simulations of tilted ABC stacking.** (a) STEM image at a FOV of 32×32 nm^2 of an ABC stacked C_{60} multilayer curved around the "axis of curvature" denoted as an arrow. (b) Cut-out of the area marked as [b] in panel a) and corresponding simulation at 5° tilt angle at the bottom. (c) Cut-out of the area marked as [c] in panel a) and corresponding simulation at 10° tilt angle at the bottom. Figure based on Ref. [104].

sandwich structures. Based on the STEM contrast and simulations and by taking C_{60} monolayers and graphene as a reference (to be mentioned later), the structure in 3.4 (e) could be determined as a triple-layer of C_{60} fullerene with an HCP structure.

The presence of the graphene layers in figure 3.4 (a) and (e) remains hidden and is not directly observable by naked eye. However the traces of the graphene lattice can be extracted numerically by calculating the Fourier transform (FT) of the STEM images. An FT of a real space lattice is similar to an EDP in reciprocal space. An EDP is formed by physical interference of electron wave functions whereas FT is formed by decomposing an image into frequency components. We therefore determined the C_{60} spacing in monolayers and relative lattice orientations directly from STEM images by using FT, similar to what we did earlier by using EDPs. The FT images of figure 3.4 (b) and (e) are presented respectively in figure 3.4 (c) and (f), in which the dashed circles are used to indicate the positions of the discernible graphene diffraction spots in frequency, and solid hexagons are used to indicate the orientations of C_{60} and graphene (111) planes in frequency domain. The FT of the graphene lattice can also be used to measure the C_{60} spacing in multilayers. Taking the accurately known graphene lattice constant as a reference, the C_{60} spacing was measured to be 10.0 ± 0.3 Å in both cases. This value is

consistent with previously obtained spacing value from TEM diffraction patterns in section 3.1.1.

We further studied the epitaxial relation between the C_{60} crystallites and graphene lattice directions by systematic investigation of misorientation angle between C_{60} and graphene lattice from electron diffraction patterns. The histogram shown in figure 3.4 (d) represents the mismatch angle distribution gathered statistically from different diffraction patterns from randomly selected areas of the non-sandwiched specimen. Figure 3.4 (g) shows a combined histogram data for misorientation angle between C_{60} and first and second layers of graphene in a sandwiched sample. The histogram in figure 3.4 (d) shows that the C_{60} crystallites clearly tend to grow epitaxially on graphene layer, following either zigzag (at 0° mismatch angle) or armchair (at 30° mismatch angle) directions of graphene lattice. This tendency of C_{60} on graphene has been earlier reported and explained by *ab initio* calculations of vdW-favoured adsorption configurations [94]. However, when the second layer of graphene is introduced at a random orientation angle as a result of sandwiching, the preferred registry is no longer available for C_{60} molecules with second graphene layer, which is expected to result in random registry. This behaviour can be confirmed by the stacked histogram in figure 3.4 (g) showing the plot of the smaller (Θ_{Gr}-C_{60}-I) and the larger (Θ_{Gr}-C_{60}-II) misorientation angles corresponding to two graphene layers in sandwiched structures. The distribution of the smaller angle is close to the result shown in 3.4 (d) of a non-sandwiched sample, while the larger angle has a more uniform distribution indicating random variation.

Simulations were also conducted to confirm the identity of the multilayer structures. The details for the STEM simulations in this thesis are given in section 2.4.3. Figure 3.4 (h) shows a constructed tri-layer for STEM image simulations. Both our simulations and earlier work show that an ABC stacked multilayer exhibits a honeycomb-like periodicity similar to the one seen in the upper left corner in figure 3.4 (e). The simulation and the region marked with [i] are compared in figure 3.4 (i), clearly confirming ABC stacking order. The lower right section of the figure 3.4 (e) displays a different contrast of C_{60} than the upper left part. The area marked with [j] in 3.4 (e) is shown in (j) together with the ABA trilayer simulation next to it. Again the simulated TEM image perfectly matches the experimental observation, identifying ABA stacking order. Similarly, the C_{60} multilayer in non-sandwiched specimen in figure 3.4 (b) can be identified as ABA stacked HCP lattice.

The STEM images of C_{60} multilayers occasionally revealed patterns resembling neither ABA nor ABC stacking shown in simulation images

above. An acceptable explanation was found by tilting the ABC stacked C_{60} trilayer with respect to the simulated electron beam.

STEM images represent a 2D projection of a 3D structure. The projection therefore appears differently when the sample is tilted. Our simulations indicate that in some regions the specimen is curved in an out of plane directions and facing the e-beam at different angles at different locations. An example STEM image taken from such an area is shown in figure 3.5 (a). We reasoned that C_{60} multilayer is slightly bent around the quasi "axis of curvature" pointed as an arrow in figure 3.5 (a). The sample plane is perpendicular with respect to the incident electron beam at the top left part, and inclined by about 5° at [b] and 10° at [c] as shown in figure 3.5 (b) and (c). The simulation images with corresponding applied tilt angles are given at the bottom of the 3.5 (b) and (c). Here again, we observe the simulated images being in good agreement with the experimental contrast.

3.1.3 C_{60} Monolayers

In this section, we investigate the C_{60} monolayers encapsulated within graphene sheets. The resulting sandwich structures contain atomically clean large areas, allowing direct study of fullerenes through atomic-scale STEM analysis. As mentioned in previous section (3.1.2) the sandwiched C_{60} show remarkable stability under the electron beam irradiation, similar to fullerenes encapsulated in carbon nanotubes [105]. We also note that the monolayer of C_{60} could only be observed in sandwich structures.

Based on high-resolution STEM images, it is easy to distinguish between monolayer and multilayer areas, with an example image given in figure 3.6 (a). Figure 3.6 (b) shows the atomically resolved close-up image from the region marked as [b]. Here we see that, the individual buckminsterfullerene molecules of a highly-ordered 2D lattice can indeed be imaged at atomic resolution. In a 2D configuration each fullerene molecule is surrounded by 6 nearest neighbours as compared to 12 nearest neighbours in crystalline bulk C_{60} [35]. Figure 3.6 (c) shows the Fourier transform of the graphene lattice in figure 3.6 (b). From the FT image we could identify the two graphene monolayers and the fullerene lattice. Additionally we measured the misorientation angle between the two graphene layers to be $\theta_{Gr} \approx 11°$.

Once again using the graphene lattice as a calibration standard, we measured the C_{60} lattice spacing in crystalline monolayer regions and obtained a value of 9.6 ± 0.1 Å. Surprisingly, this spacing is 4 to 5% smaller than those for the bulk 3D C_{60} crystals [106], [107]. This spacing

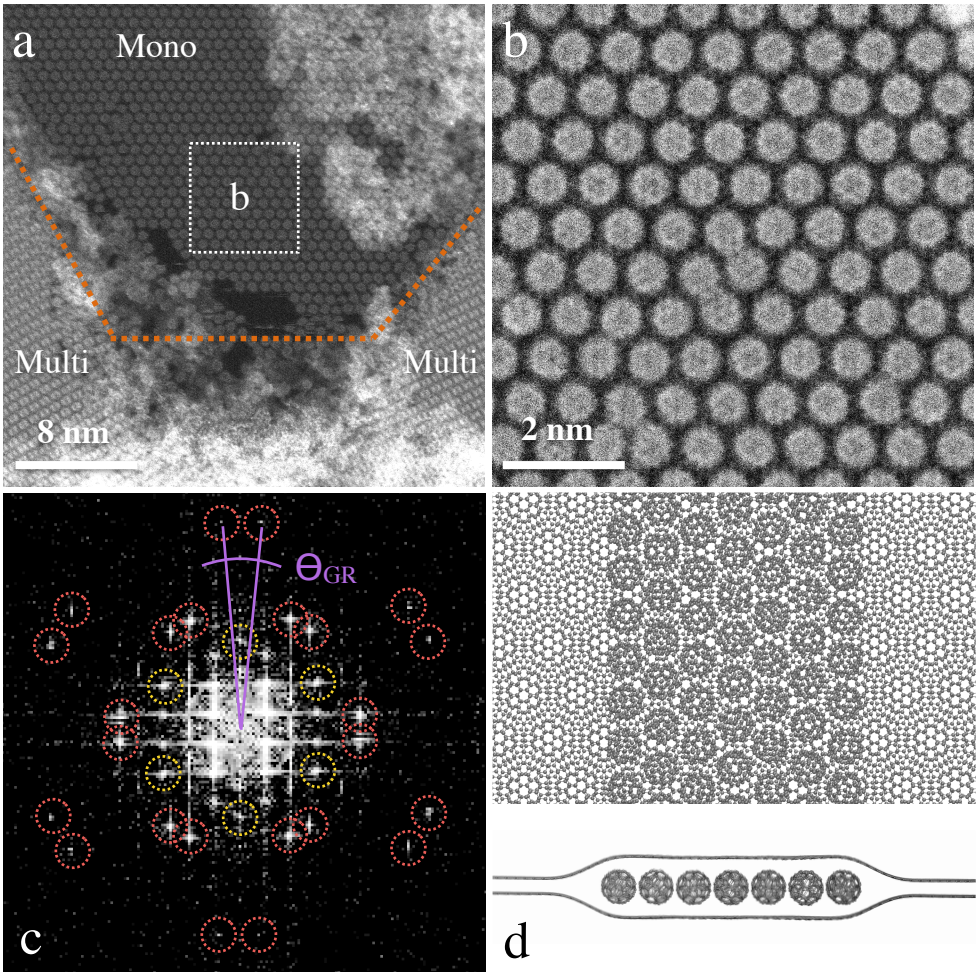

Figure 3.6: **C_{60} Monolayer in buckyball sandwich**. (a) Sandwich structure with both monolayer and multilayer C_{60} regions at FOV of 32×32 nm^2 and (b) a higher magnification of the area marked as [b] at FOV of 8×8 nm^2. (c) Fourier transform of (b), with graphene pattern marked by red dashed circles and some of the fullerene reflections marked in yellow. (d) Model of a monolayer C_{60} sandwiched between two graphene layers (top and side views). Figure based on Ref. [104].

is also smaller than in 1D carbon pea-pods where C_{60} are aligned in 1D, whose reported values vary from 9.7 to 10.0 Å (arguably affected by the endohedral metal atoms present in some studies) [105], [108], [109].

To understand this difference in C_{60} spacing, atomistic simulations were used to calculate and compare the equilibrium lattice constants of

the molecules in bulk 3D and 2D face-centered cubic (FCC) C_{60} lattice and in a 2D sandwich heterostructure. Figure 3.6 (d) shows the simulated sandwich structure consisting of 7×20 array of HCP C_{60} molecules in-between two graphene nanoribbons with a misorientation angle of $\theta_{Gr}\approx 11^\circ$ that we used to study the intermolecular distance in C_{60}. The details of the simulations are given in section 2.4.1. In case of 3D bulk C_{60}, we found a zero Kelvin equilibrium distances of 9.65 Å (A-M), 9.86 Å (C09), and 10.03 Å (DF2), while for an infinite 2D lattice, the distances found were 9.62 Å (A-M, consistent with ref. [110]), 9.91 Å (C09), and 10.02 Å (DF2). Although DFT gives slightly larger values than the intermolecular potential, solely by dimensionality of the C_{60} crystallites, it was not possible to explain the observed monolayer spacing. However, in the simulated sandwich system (cross-section shown at the bottom in fig. 3.6 (d)), the A-M calculated average equilibrium distance was significantly shorter at 9.22 ± 0.15 Å (standard deviation due to directional anisotropy), which indicates a contraction of 4.7% compared with the calculated bulk value. Hence, despite the offset in the simulated distance values, they do agree with the experiment that the interaction with the graphene layers in sandwich structure compresses the C_{60} lattice. Straining the graphene layers in the simulation did not significantly influence the spacing, as discussed below.

STEM images of the fullerenes at the edges of the monolayer shown in figure 3.7 (a), provide an additional evidence that the fullerenes are located in-between the graphene layers as opposed to e.g. fullerenes on top of a bilayer graphene. In regions free of fullerenes, the two graphene monolayers form a rotated bilayer and exhibit the characteristic moiré interference pattern in MAADF images. It can be seen that the single patterns observed in figure 3.7 (a) consist of periodic spots of enhanced intensity as highlighted by the dashed circles in figure. Figure 3.7 (b) and (c) shows the STEM simulation for a relaxed and strained structures and their cross-section model beneath them, respectively, as a comparison to the experimental image. In these images it is shown that the observed contrast in moiré pattern is due to a non-linear effect enhancing the intensity when two atoms are located at the same projected position and separated by no more than about ∼5 Å in the incident beam direction. This effect is observed on all bilayer areas but changes notably near the edge of the fullerene monolayer. At the proximity of C_{60} edges, the graphene sheets get apart from each other, causing a visible loss in moiré contrast.

We assume that suspension due to an uneven edge has an influence on the appearance of the moiré pattern. Figure 3.7 (d) shows a STEM

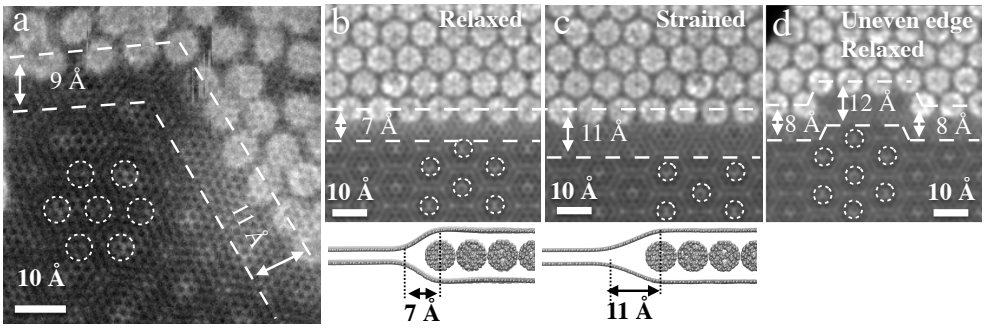

Figure 3.7: **Moiré effect at the edges of the C_{60} monolayer.** (a) Experimental image, with the non-linear contribution of the moiré pattern marked with dashed circles indicating a presence of twisted bilayer graphene. The dashed lines highlight the distance from the first C_{60} row to the beginning of the visible moiré pattern. (b) Simulated STEM MAADF image for the relaxed structure, showing slightly smaller distance compared to experiment and its cross-section model at the bottom. (c) Simulated STEM image of strained structure with its cross-section model at the bottom (under 330 MPa of lateral tension in vertical direction) and (d) relaxed structure with an uneven edge, both being in good agreement with the experiment.

simulation of a relaxed structure with three missing molecules at the edge, causing the distance to the moiré pattern to vary from 8 to 12 Å, consistent with the observed distance that varies from 9 to 11 Å. Moreover, the lateral extent corresponding to moiré-edge distance (fig. 3.7 (a)) gives an indication that the graphene layers might be under strain. This argument is tested by the simulations given in figure 3.7 (b) and (c) and it shows that adding strain to relaxed simulation enlarges the distance between fullerene edge and moiré of the rotated bilayer graphene. In figure 3.7 (b) a 330 MPa of lateral tension (vertical in the simulation image, horizontal in cross-section image) is applied to sandwich structure, resulting in 11 Å distance from moiré from to edge, compared to 7 Å in the unstrained cross-section model. Thus, the strained model and relaxed uneven edge both provide a good match to the experiment. The tension, however, does not seem to influence the intermolecular spacing.

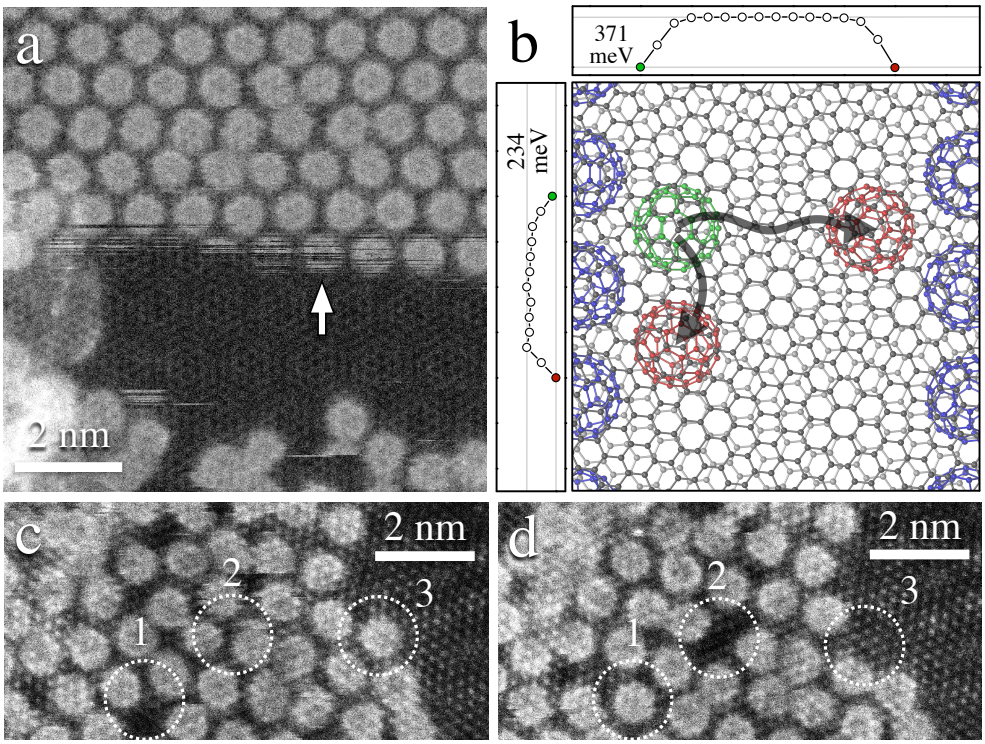

Figure 3.8: **Dynamics of sandwiched C_{60}.** (a) An oscillating C_{60} at the boundary of the sandwiched fullerene monolayer. At the position indicated by the arrow, molecule disappears and appears 17 times during 100 scan lines. (b) Nudged elastic band paths and energy barriers for fullerene diffusion along the edge of C_{60} monolayer (vertical) and from one edge of the gap to another (horizontal). (c and d) A disordered monolayer showing a void propagating from location 1 to 2, and the C_{60} molecule at location 3 escaping outside the field of view between the two consecutive frames. Figure based on Ref. [104].

3.1.4 Edge dynamics and diffusion in sandwiched C_{60} monolayer

Compared to 3D bulk form and 1D carbon pea-pods, the 2D buckyball sandwich shows different structural properties such as different number of nearest neighbours and reduced lattice spacing. As a result the intermolecular interactions and dynamical behaviour of the C_{60} molecules are expected to be different in buckyball sandwiches and this new heterostructure presents dramatically different environment for fullerenes. As an example, inside the pea-pod, the C_{60} cannot pass each other and

thus diffusion is entirely prevented. However, in sandwich this is not the case, and the molecules can and do diffuse as we have observed.

The encapsulation of the fullerenes allows the direct observation of molecular dynamics in high-resolution STEM images and image sequences. Individual fullerene molecules are found to be highly mobile at the boundary of the C_{60} monolayers. Figure 3.8 (a) shows a MAADF STEM image of a sandwich region where a gap without fullerenes is observed, while moiré pattern contrast stays constant, indicating that graphene layers remain equally separated. Here we also observe some oscillating C_{60} at the partially filled outermost row, which occupied and vacated edge sites multiple times during the acquisition of subsequent lines of the scanned image, resulting in the "interlaced" appearance of C_{60} molecules. As an example, the C_{60} molecule marked by an arrow in figure 3.8 (a) has disappeared and reappeared at least 17 times during the acquisition of 100 scan lines in $\sim$1 second at this region of the image. However, the molecule remained typically stationary during each single scan line which take $\sim$1 ms to traverse across the molecule. Apparently, it is possible even to quantify the single-molecule diffusion in the sandwich structure by using direct STEM imaging. Regardless of their mobility in this region, it seems that the molecules remain confined inside the graphene wrap and cannot escape completely.

To understand the observed dynamics, the related diffusion barriers were also calculated using the nudged elastic band method. For the atomistic simulations the same approach was used described in section 2.4.1 by using the same supercell model. Here however, part of the fullerene-containing area was cut out of the model in order to create a gap inside the fullerene monolayer and fixed the outermost rows of fullerenes and edges of the graphene layers accordingly. The barriers were calculated by using the nudged elastic band method with a spring constant of 10 eV/Å [111]. In figure 3.8 (b) two possible diffusion paths are described for C_{60}: one for the diffusion along the edge of the monolayer (234 meV) and the other for the diffusion from one edge to another across the gap (371 meV). The green molecule represents the diffusing C_{60} at the edge and red molecules indicate the two possible final positions of the green molecule. The values are in reasonable agreement with the earlier study of molecular diffusion process in C_{60} crystals [112], [113]. The required diffusion energies are easily available from the electron beam, but these energies may also be activated thermally at room temperature. From the second path in the figure 3.8 (b), the barrier for moving the C_{60} molecule inside the gap in the sandwich structure was estimated to be less than 5 meV. This explains why completely isolated fullerene molecules were

never observed in the experimental images.

Figure 3.8 (c) and (d) shows a STEM image sequence of disordered C_{60} monolayer region. Here we observe different dynamics of molecules. Interestingly, the voids in the C_{60} arrangement can move inside the lattice. For example, a void marked with dashed circle and 1, propagated from position 1 to 2 between the two shown frames, and the single molecule escaped outside the field of view from location marked as 3. Nevertheless, this edge appears to be more stable and tightly constrained inside the graphene sandwich, displaying no oscillations like those seen on the edges of fully crystalline regions of fullerenes 3.8 (a).

3.1.5 Rotation and bonding of C_{60} in sandwich structure

In this section we study the rotation and bonding of sandwiched C_{60} molecules during STEM imaging under the electron irradiation by analysing the time series of images. For imaging a 60 keV electron probe with a 25 pA current was scanning a FOV of 4×4 nm^2 acquiring a frame every 60 seconds. The dose equivalent between the frames per frame was hence $\sim 8.2\times10^6$ $eÅ^{-2}$. At this energy level at least three types of structural modifications are possible: a knock-on damage of the C_{60}, bonding between C_{60} molecules, or bonding between C_{60} and graphene. In an earlier study it was shown that the C_{60} knock-on damage results in the formation of C_{59} on the first step, leaving the molecule with a reactive dangling bond next to the vacancy [114]. We note that, graphene knock-on damage is not expected here because of its suppression at this energy level since the electron beam energy is below the graphene knock-on threshold [19], [18].

Figure 3.9 (a - c) shows the STEM MAADF images of the unfiltered, as-recorded time/electron dose sequence of sandwiched C_{60} monolayer. Here we observe that the graphene lattice is clearly resolved and some fullerenes undergo structural changes. However, the lattice contrast of the underlying and overlying graphene layers overlap with the intrinsic contrast of the fullerenes. To enhance the image contrast and reveal atomic-scale details of the C_{60} molecules we eliminated graphene lattice mathematically by using Fourier filtering demonstrated in figure 3.9 (d-f). Figure 3.9 (d) shows the Fourier filtered image of 3.9 (a) as an example. Fourier transfer image of a) is given in 3.9 (e) and figure 3.9 (f) shows the graphene components. In Fourier filtering, first we get the FT image of the experimental contrast, then remove the unwanted frequency

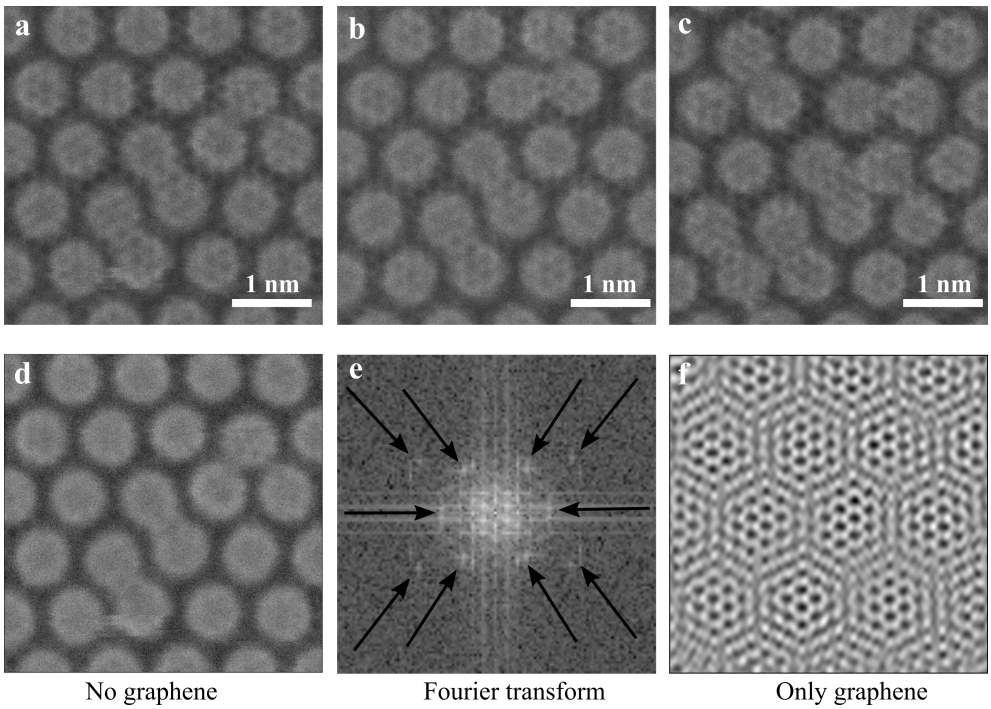

Figure 3.9: **A sequence of as-acquired STEM images and Fourier filtering.** (a-c) A series of as-recorded MAADF STEM images of sandwiched C_{60} monolayer at a FOV of 4×4 nm^2. (d) Fourier filtered image of (a). The lattice of graphene is removed by masking the corresponding spots in the FT image. (e) Fourier transform image of (a). The arrows indicate the frequency components of graphene. (f) The periodic components of graphene.

components from FT image, and finally inversely transform the modified FT image.

The Fourier-filtered and contrast enhanced version of the dose/time sequence images are given in figure 3.10 (a to c). A quite remarkable feature of the image in figure 3.10 (a) is that beyond the spherical symmetry no structure can be discerned for the isolated fullerenes, although the graphene lattice is structurally resolved in the unfiltered images. It is well known that in FCC structured 3D bulk C_{60}, the molecules perform nearly free rotations at room temperature [102], [115]. The C_{60} molecules confined inside a single-walled carbon nanotubes (i.e nano-peapods) are also shown to exhibit quasi-free rotations at room temperature [116], [117]. Considering that the absorption energy of C_{60} on graphene is ∼0.9 eV and different absorption geometries are separated by <0.1 eV,

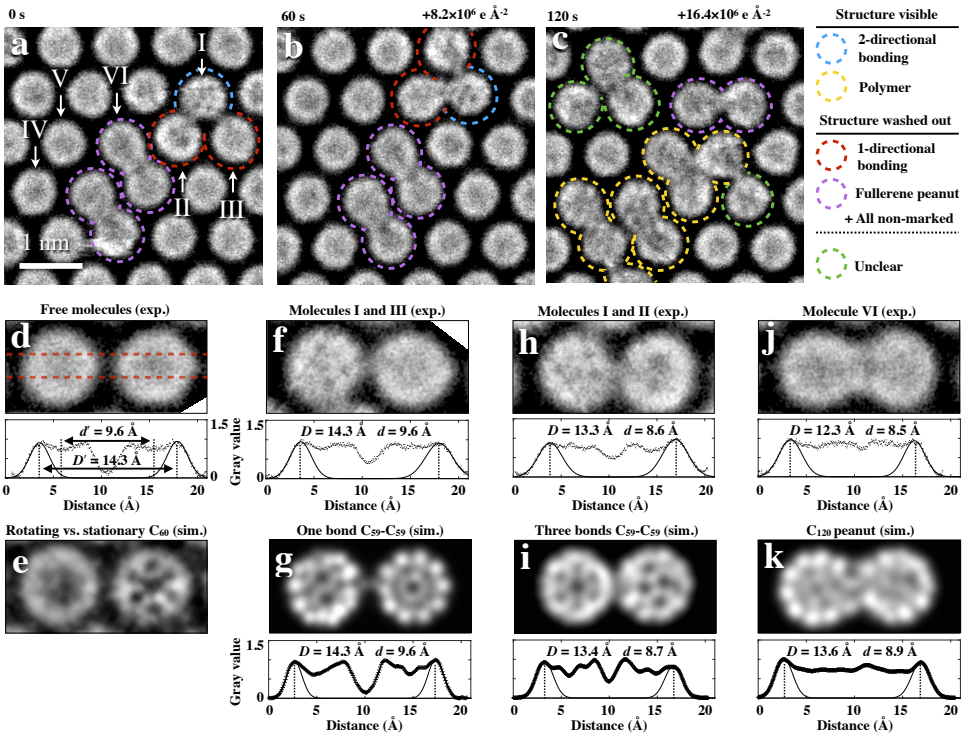

Figure 3.10: **Fullerene reactions.** (a-c) A Fourier-filtered dose/time series of a monolayer C_{60} sandwich. The images are smoothed to reduce the pixel noise and contrast-enhanced to maximize the visibility of the C_{60} internal structures (images with different contrast settings are shown in figure 3.11 (a to i)). The blue dashed lines highlight the fullerenes that appear to be locked in position by two-directional bonding, showing a visible internal contrast and those stationary due to polymerization are marked with yellow colour. The dimers (purple) and molecules with one-directional bond (red) still seem to be moving, obscuring their internal contrast. (d) STEM image of a pair of rotating C_{60} [IV, and V in (a)] and a simulation image of a rotating (left) and a stationary (right) C_{60} in (e). (f) A loosely bound pair of fullerenes and corresponding simulation of C_{59} - C_{59} dimer with single bond in (g) and a tightly bonded pair and its simulation as C_{59} -C_{59} dimer with triple bonds in (h) and (i). A typical peanut dimer in (j) and a simulation image of C_{120} in (k). The red dashes in (d) correspond to the integration width of the line profiles plotted in (d) to (k). The parameters of the simulations are described in section 2.4.1. Figure based on Ref. [104].

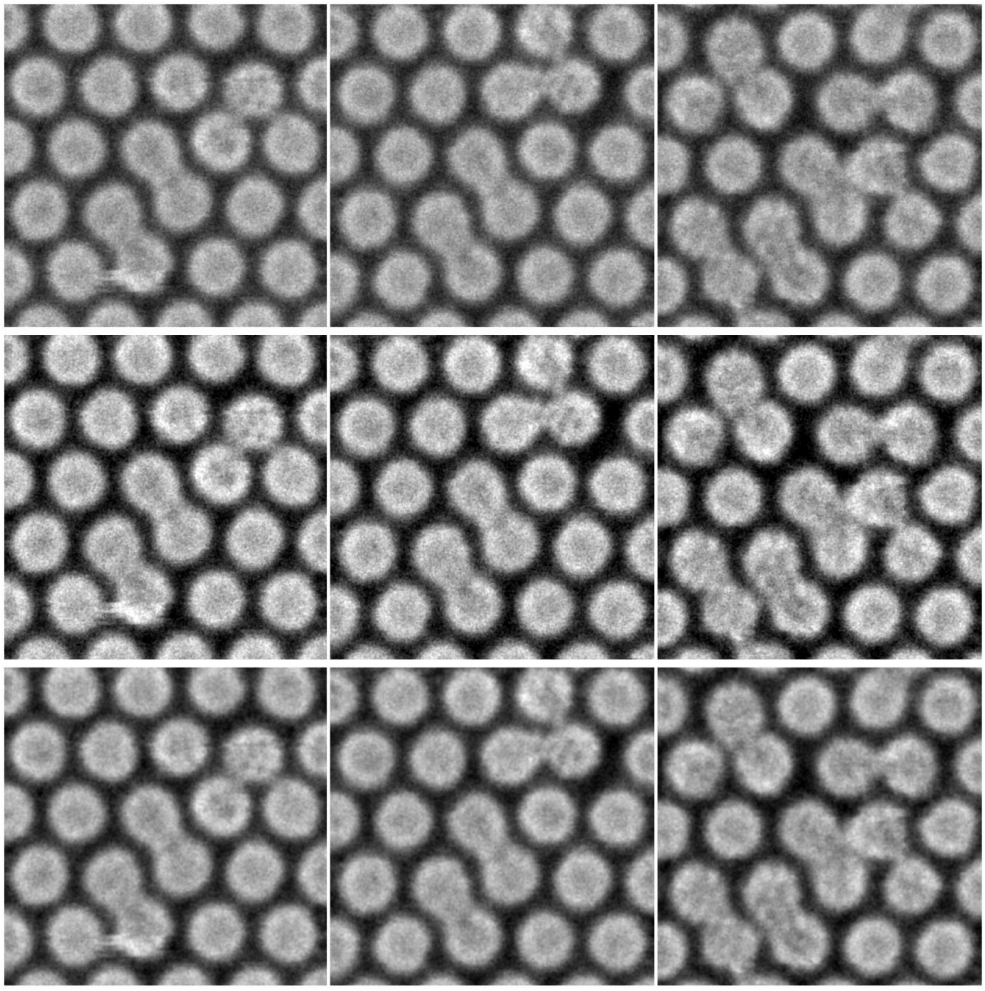

Figure 3.11: **Fourier-filtered STEM images of rotating and fusing fullerenes.** These are the same images as in figure 3.10 (a to c) , only shown without overlay and in each line with different contrast enhancement. The FOV is 4×4 nm^2.

even the encapsulation between the graphene layers should not prevent the C_{60} rotation under our experimental conditions [118], [94]. Based on these studies and our observations, we attribute the lack of internal structure of individual fullerenes to their rotation during the imaging. In STEM, additional to thermal activation, the rotation of C_{60} molecules could also be activated by electron irradiation. Due to this constant rotation, none of the isolated fullerenes show internal structure in our STEM images unless they are fixed to their position by some kind of bonding or fusion.

Confinement of fullerenes in 2D sandwich provides a unique environment for intermolecular reactions and bonding. These interactions can be visualized by monitoring time/electron dose-dependent changes in the atomic positions of the bonding or fusing molecules in high-resolution STEM. Such image sequences may provide information that is not easily available by other experimental techniques. Throughout the sequence in figure 3.10 (a to c), all isolated C_{60} molecules (unmarked objects) display only spherical symmetry, whereas in clustered molecules that are marked with the yellow dashed lines, the internal structure is evident. As the electron dose increases with time, some C_{60} fullerenes clearly start to form bonds or fuse together with the neighbouring molecules. As a result of bond formation and fusion, these fullerenes become "locked" into a certain position that allows their internal structure to be resolved. To demonstrate clearly that some of the fullerene molecules –mostly the merged ones–display internal contrast, while others do not, additional filtered images are presented in figure 3.11 with three different contrast settings (the best visibility may depend on the settings of the printer or monitor). The bond formation and fusion process is a direct observation of fullerene polymerization, which has been reported in earlier studies where polymerization was induced by ultraviolet light and electron beam irradiation of 3D C_{60} crystals and for C_{60} molecules confined in carbon nanotubes [119], [120], [105].

In high-resolution images, we repeatedly observed peanut-shaped dimers [120] and triangular trimers in the electron irradiated fullerene sandwich. Quite remarkably, some fullerene molecules seem to form a bond with neighbouring molecule without fusing together, especially the ones that are indicated with blue and red dashed lines in figure 3.10 (a) and (b). For example, in the C_{60} trimer marked with I, II, and III in figure 3.10 (a), the molecule I that is linked to two neighbours is apparently locked in its position and can not rotate and therefore its internal structure is clearly visible. However, the other two molecules of the trimer, marked by II and III, are presumably bonded from one side only and can still rotate or oscillate around a ground state, because their internal structure is smeared out. We used also STEM simulations to compare the appearances of the rotating and locked fullerenes. The result is presented in figure 3.10 (e) revealing the quite distinct appearances of rotating and locked fullerenes. The molecule on the left side is a rotating fullerene that is an average of a hundred random orientations, and the one on the right side is a locked C_{60} (to mimic the experimental contrast first the graphene was included in the simulation and later Fourier filtered). Based on their internal contrast, we conclude that the C_{120} dimers or "peanuts"

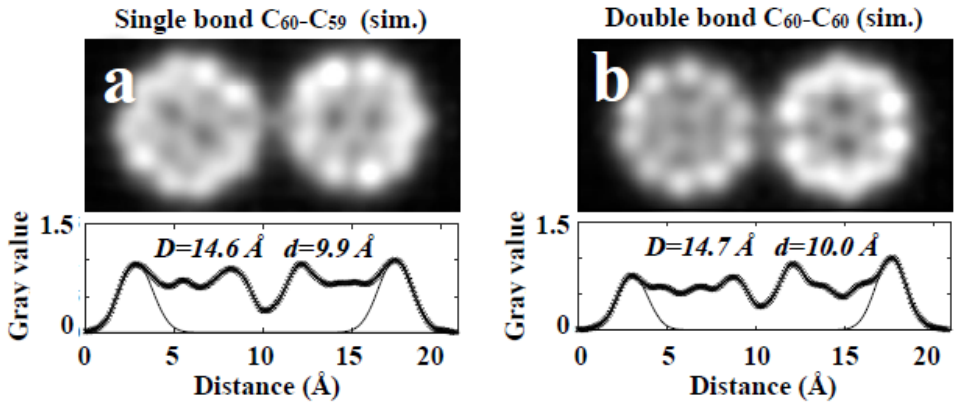

Figure 3.12: **STEM simulations of merged fullerenes.** (a) STEM simulation of singly bonded C_{60}-C_{59} dimer and (b) of a C_{60} - C_{60} pair with a double bond. Simulation parameters are described in section 2.4.1. Figure based on Ref. [104].

highlighted by purple dashed lines in figure 3.10 (a to c), exhibit rotation around their longitudinal axis that smears out any internal structure. This can be confirmed by the clear difference in internal contrast between the purple-marked dimers and polymerized C_{60} with additional cross-linking marked with yellow.

Simulations were also used to study the bonding. By using the C09 functional in the GPAW finite difference mode (0.19 Å grid spacing, Gamma point only), two C_{60} were placed in the center of a 32×20×20 Å unit cell and their atomic structure was relaxed [91]. To understand the impact of electron irradiation on apparent bond length, first one C atom was removed from the second C_{60} and then the structure was relaxed and then further one atom was removed from the second C_{60} followed by the relaxation of the structure, resulting in both single- or triple-bonded dimers. For the C_{60} - C_{59} structure, molecular dynamics (MD) simulations were further run in the linear combination of atomic orbitals (LCAO) DFT mode (15 eV kinetic energy) to simulate the rotation of the C_{59} caused by an electron energy input on one of the carbon atoms.

We assume that as in the case of a double or a triple bond, a single bond between two fullerene molecules should be able to make the structure rotationally stiff because of the overlap of the π-orbitals on connecting carbon atoms. However, the energy available from the electron beam can surpass this barrier. A DFT molecular dynamics simulation of a dimer was run where one molecule is prevented from rotating by fixing

atoms on its back wall, and one atom on the side of the other molecule is given relatively high kinetic energy (15 eV), imitating an electron irradiation effect. This emulates the case where a fullerene is bonded by a single C - C bond to an already rotationally locked neighbour. This result shows that even if the single bond is preserved, in contrast to the locked molecule the second molecule rotates noticeably under the electron irradiation. For the resulting simulated movie, the reader is referred to the supplementary section of the article presented in the first entry in the List of Publications [104].

We further investigated dimeric bonds in fullerenes by measuring the apparent center-to-center distances (d) of paired molecules in figure 3.10 (a). For comparison, figure 3.10 (d) shows a pair of free isolated molecules denoted as IV and V, whose center-to-center distance (d') is set to 9.6 Å based on the average C_{60} spacing in the monolayer. To measure the d of linked molecules, Gaussian line shapes were fitted to the outer edge of the intensity profiles and peak-to-peak distance (D) was used to calculate $d = d' + D - D'$, where D' is the reference distance measured for adjacent isolated fullerenes. Figure 3.10 (f) shows what is likely a singly bonded C_{59} - C_{59} dimer with d = 9.6 Å (molecules I and III in figure (a)), quite similar to its simulated version in figure 3.10 (g). Additionally, we simulated the spacing of a singly bonded C_{60} - C_{59} and C_{60} - C_{60} dimers with double bonds, yielding slightly larger values of 9.9 Å and 10.0 Å, respectively as shown in figure 3.12 (a) and (b). A seemingly more tightly bonded pair of C_{60} molecules marked as I and II is compared with its simulation equivalent in figures 3.10 (h) and (i). We interpret this as a pair of C_{59} molecules linked with three bonds, on the basis of the measured d = 8.6 Å, matching well to a simulated value of 8.7 Å. Figure 3.10 (j) and (k) shows the comparison of the peanut structures, where we observe that the experimental structure (molecule VI) is slightly smaller than the simulated one, 8.5 versus 8.9 Å. However, we note that there might be many possible structures of stable fullerene peanuts with less than 120 carbon atoms. In case of the molecules marked with green colour, due to the subtle contrast between molecules it was not clear if bond formation took place. Based on the interaction of some fullerenes, it is observed that the bonding between C_{60} can be reversible whereas polymerization seems to be irreversible.

3.1.6 Conclusion

In this work, we have created and characterized a 0D/2D mixed dimensional heterostructure of C_{60} fullerenes encapsulated in-between two

graphene monolayers. The C_{60} monolayers inside the sandwich structure exhibit a lattice spacing of 9.6 Å, which is ∼4-5% smaller than those for the bulk crystals. We were able to observe the dynamics of the molecules, with weakly bound fullerenes oscillating between different positions at the boundaries of the crystalline molecular C_{60} monolayer, along with mobile vacancies in a disordered 2D fullerene structure where the graphene layers are suspended over areas in the nanometer range. Lastly, we observed the individual rotating C_{60} molecules becoming dimers with suppressed rotation under electron irradiation and further transforming into molecular clusters locked into their position, allowing the internal structure to be revealed. The graphene sandwich thus provides a nanoscale reaction chamber, protection from radiation damage to some degree, a clean interface to the microscope vacuum, and a low-contrast background that can be eliminated from the image.

3.2 Self-alignment and deformations in graphene-carbon nanotube heterostructures

This section is dedicated to the graphene-carbon nanotube van der Waals (vdW) heterostructures and their self alignment and deformations at the atomic scale. The content of this chapter is based on the second entry of the List of Publications.

The vdW heterostructures typically combine graphene and other two- or lower-dimensional molecules into vertical stacks [5], [121], [122]. The main idea behind this concept is to conserve the covalently-bonded structure of the molecules that interact with each other mainly through vdW bonding, while the electronic and plasmonic coupling between the layers remains relatively strong and yields the formation of a completely new class of functional (meta-)materials [5], [122, 123, 124, 125, 126]. It is noteworthy that, regardless of the weak vdW interactions the lattice mismatches in these structures can result in particular morphological changes [127], [128].

The fabrication of 2D heterostructures is usually achieved either by directly stacking the sheets on top of each other [5] or via epitaxial growth [129], [130], [131], [132], [133]. Moreover, tendency to maximize the contact area apparently generates self-cleaning within the stacked layers, producing atomically clean and observable interfaces. It is however much more challenging to realize ordered, sufficiently clean, and thin layers of low-dimensional nanostructures owing to their high chemical reactivity. Due to this, the attempts to explore these materials experimentally and explain the fundamental phenomena governing the interlayer interactions in the atomic scale still remains a challenge.

3.2.1 SWCNT-graphene heterostructure: First observations

In this study SWCNTs were dry-deposited on suspended monolayer graphene to form a 1D/2D molecular hetero-interface. We investigate stacking behaviour of SWCNTs onto graphene and the effects of the absorption on morphology of materials using the STEM and three dimensional reconstructions of the interfaces. The SWCNTs are hollow cylindrical tubes and it has been shown that during the interaction with substrates they can undergo deformations [134], [135], [136]. Although their covalent molecular structure remains preserved during this process, it is expected

to affect their electronic properties [137]. Similarly, in one of the earlier experiments it was demonstrated that simply by changing the angular alignment of the atomic lattices, the contact resistance between a carbon nanotube and a graphene substrate can be modified by an order of magnitude which indicates that relative orientation has a strong influence on electronic coupling of these heterostructures [138].

The heterostructures presented in this research were produced by a method illustrated in figure 3.13 (a). The procedure comprises following steps: the synthesis of carbon nanotubes by floating catalyst CVD [81], [82], a direct deposition onto monolayer graphene [83] and cleaning the specimen by laser irradiation in vacuum [84] before the STEM analysis. Figure 3.13 (b) shows the overview bright-field micrograph of a typical sample. At this magnification the nanotubes are not visible. Figure 3.13 (c) shows the MAADF STEM image magnifying the small region given in bright-field image in (a). Here we see that, the sample contains large atomically clean areas of up to 1 μm^2 in size, which we attribute to effective laser cleaning. In a given field of view (FOV), we found several SWCNTs (shown by red arrows in fig. 3.13 (c)) in direct contact with the graphene monolayer, preserving their orientations over hundreds of nanometers. This contact can be evidenced by the common focus of graphene and nanotubes based on the convergent probe configuration in STEM system, such that for the different atoms or molecules to appear sharp simultaneously, they need to be within the depth of field of approximately 2-3 nm and at this range it is the vdW forces that brings the molecules together.

The determination of the alignment of the nanotubes on monolayer graphene surface is relatively straightforward based on the high-resolution STEM images. The nanotubes on graphene adopt either well-aligned or meandering configurations, which are directly visible in our STEM observations as in figure 3.13 (c). In further analysis, however, we will focus on the well-aligned segments that demonstrate the highest possible periodicity because their structure can be identified more precisely.

For comparison we also show an example image of a non-cleaned sample in figure 3.14 (a) and (b). Surface contamination generally originates from the CVD process, transferring of layers and heterostructures and the environment, which is a major issue in fabrication of 2D materials [140], [141]. Regardless of our intrinsically clean synthesis [81], [82] and deposition procedure used for SWCNTs [83], the heterostructures synthesized on commercial CVD graphene were covered by contaminating material shown in figure 3.14. This figure shows how the samples typically look before the high power laser treatment for annealing [84]. Here,

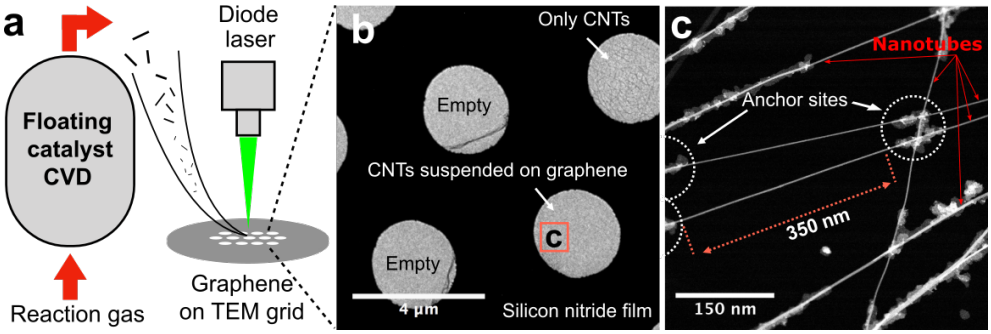

Figure 3.13: **SWCNT-graphene heterostructure.** (a) Schematic of fabrication of heterostructure by thermophoretic deposition of floating catalyst CVD SWCNTs on graphene and laser cleaning process in vacuum. (b) Bright-field overview of a typical specimen on TEM grid after laser cleaning. (c) STEM MAADF image from the region marked as [c]. The carbon nanotubes on graphene monolayer are observable at this magnification (indicated by red arrows). Figure based on Ref. [139].

the clean graphene spots, identified as black contrast values are about 5-20 nm in size. Although this much size is sufficient for observation and identification of 2D materials, in case of SWCNTs the structural determination is strongly hindered and the topographic features around them are concealed. As obvious from this comparison, unlike non-cleaned samples, the laser cleaned heterostructures are devoid of contamination that hinders the view during the STEM analysis and their atomic structure can be directly determined. The laser cleaning process of the samples is described in section 2.3.4.

3.2.2 Chiral index assignment for graphene-suspended carbon nanotubes

SWCNTs are uniquely identified by reference to their chiral indices (n, m), which entirely determine their structural and electronic properties as mentioned in section 2.1.4. Therefore, it is of crucial importance to precisely determine chiral indices of a carbon nanotube. The chiral indices can be identified from the electron diffraction patterns [3], atomically-resolved experimental images [142] or their Fourier transforms (FTs). The determination of (n, m) of a SWCNT from diffraction patterns using a TEM has many possibilities [143], [144] [145], [146], [147]. This method is basically based on the measurement of the diameter from the exper-

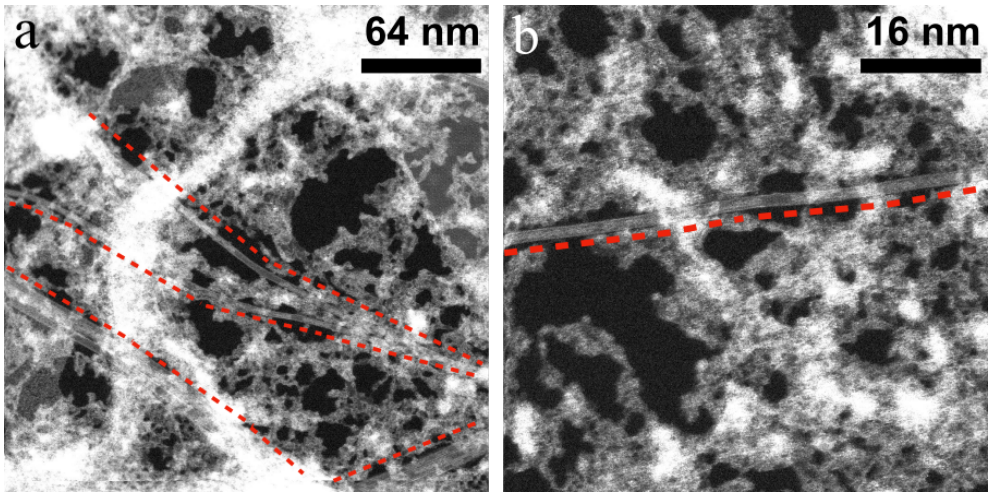

Figure 3.14: **STEM images of non-cleaned heterostructure.** (a) As-synthesized example of dry-deposited SWCNTs on commercial monolayer graphene at FOV of 256×256 nm^2 and (b) at FOV of 64×64 nm^2. The dark contrast in these images is clean graphene. The locations of carbon nanotubes are highlighted by red dashed lines to guide the reader's eye. Figure based on Ref. [139].

imental image, and the chiral angle θ_{chiral} in reciprocal space through the analysis of EDPs [147]. However, all modern implementations rely on the structural representation of a SWCNTs in the reciprocal space, extracting the structural parameters based on the relative positions of the characteristic diffraction spots [148], [146], [144].

In this work, instead of using electron diffraction, atomic-resolution STEM images and their Fourier transformations such as those shown in figure 3.15 (a-c) were employed to assign the chiral indices of the nanotubes. In STEM experiments sample tilt was eliminated by bringing the 64×64 nm FOV completely into focus by rotating the sample in a standard Nion double-tilt holder. With our ∼2-3 nm depth of view, this corresponds to a maximum tilt angle of less than 5°, providing good unambiguity in determining the chiral indices (n, m). The diameters of the nanotubes were measured from images recorded by setting the scan direction perpendicular to the carbon nanotube axis, in order to minimize spatial inaccuracies arising from scan distortions (i.e variations in the vertical scan speed) or drift. For reliable (n, m) determination, both parallel and perpendicular scans were used and compared.

In figure 3.15 (a) we observe a atomically-resolved STEM MAADF image of a SWCNT-graphene interface and its close-up in (b) which

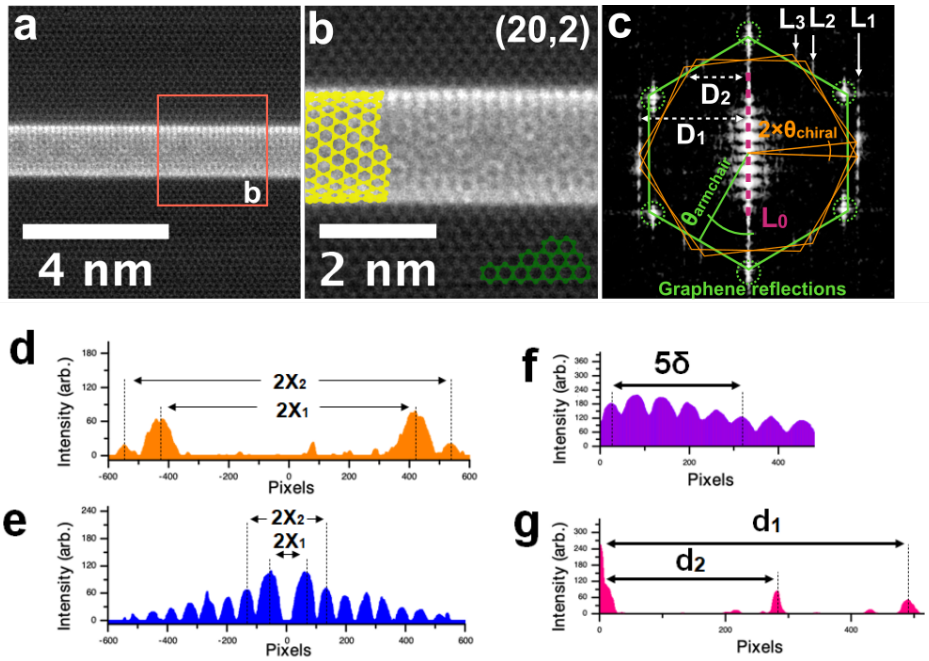

Figure 3.15: **SWCNT-graphene interface and Fourier transform analysis.** (a) Atomic-resolution STEM MAADF image of a nanotube in contact with graphene at a FOV of 8×8 nm^2 and (b) a close-up image of the region marked as [b]. The chiral indices obtained from the FT correspond to (20, 2). (c) The Fourier transform (FT) of image in panel (a). The L_i and d_i indicate the positions of layer lines and their distances from equatorial line L_0. (d-e) The intensity profiles along the layer lines L_1 and L_2. (f) The intensity profile along the L_0 and (f) perpendicular to L_0. Figure based on Ref. [139].

represents the region marked as [b]. The FT image of figure 3.15 (a) is presented in figure 3.15 (c) which includes patterns from both graphene and SWCNT lattices. This dual contribution from both materials creates a mixed contrast in real space image, therefore structural identification requires data analysis in Fourier space. Layer lines L_1, L_2 and L_3 and the equatorial line L_0 in figure 3.15 (c) originate from the lattice of the carbon nanotube, and the graphene components (shown in green colour) arise from the atoms in the background. The intensity oscillations along the lines L_1, L_2 and L_3 and their equatorial spacing $d_{1...n}$ are mathematically related to the structure of the nanotube, where each layer line is described by single Bessel function [149]. Considering that SWCNTs may compress

radially on the graphene surface and consequently exhibit an ill-defined diameter [134], the best way to determine their structure is to analyse the layer line spacing [148] and the oscillations along the lines [144] separately and comparing the experimental images with STEM simulations [150]. Following this procedure, first the chiral indices of the SWCNT given in figure 3.15 (a-b) were determined and then the robustness of this method was tested in the presence of radial deformations.

The chiral indices are related to the structure of a carbon nanotube in three-dimensional reciprocal space, described by a set of Bessel functions [145]. When intersected by Ewald's sphere, these functions are represented by a number of reflection layer lines that encode the structure of the nanotube. In earlier studies, it has been shown that the axial distances of the layer lines ($L_{1...n}$) from the equatorial line L_0 are directly related to the chiral indices (n, m) [148], and so are the square of a Bessel functions dominating the intensity distribution along each layer line [144], [146]. Figures 3.15 (d) and (e) plot the intensity profiles along the layer lines L_1 and L_2. By measuring the relative distances of the first and second maxima we can find out the order of the Bessel function along the reflection layer line by calculating the ratio $J_n(x) = X_2/X_1$, yielding the chiral indices [144]. In a similar approach, we can also use the line spacings, d_1 and d_2 to measure (n, m), for which the related intensity profiles are plotted in figures 3.15 (f) and (g). The calibration of this method is carried out by the period of oscillation along the equatorial line, δ, proportional only to the separation of the tube wall, making it susceptible to radial aberrations.

A calculation of X_2/X_1 along L_2 results in 1.244 ± 0.005 and along L_1 2.202 ± 0.005, the deviations arising due to peak positions. These results match best to $n = 20$ and $m = 2$, with a second best match of $n = 21$ and $m = 2$. Similarly, using the d_i to determine the structure, yields $n = 20.39 \pm 0.1$ and $m = 1.95 \pm 0.1$.

In order to evaluate the robustness of this method against radial deformations [144], the STEM simulations were performed for SWCNTs compressed radially by 0%, 3%, and 6% and the chiral indices for these SWCNTs were determined. The parameters of STEM simulations are given in section 2.4.3. To achieve radial compression, the SWCNTs were forced into an elliptical shape by moving every atom in the original structure to match the ellipses of different eccentricities. Figures 3.16 (a to c) show simulated images and corresponding FTs of (20, 2) SWCNTs radially compressed respectively by 0%, 3%, and 6%. Starting with the non-compressed tube, we get $X_2/X_1 = 1.246 \pm 0.001$ along L_2 and 2.177 $\pm$ 0.001 along L_1, matching almost perfectly to $n = 20$ and $m = 2$. Like-

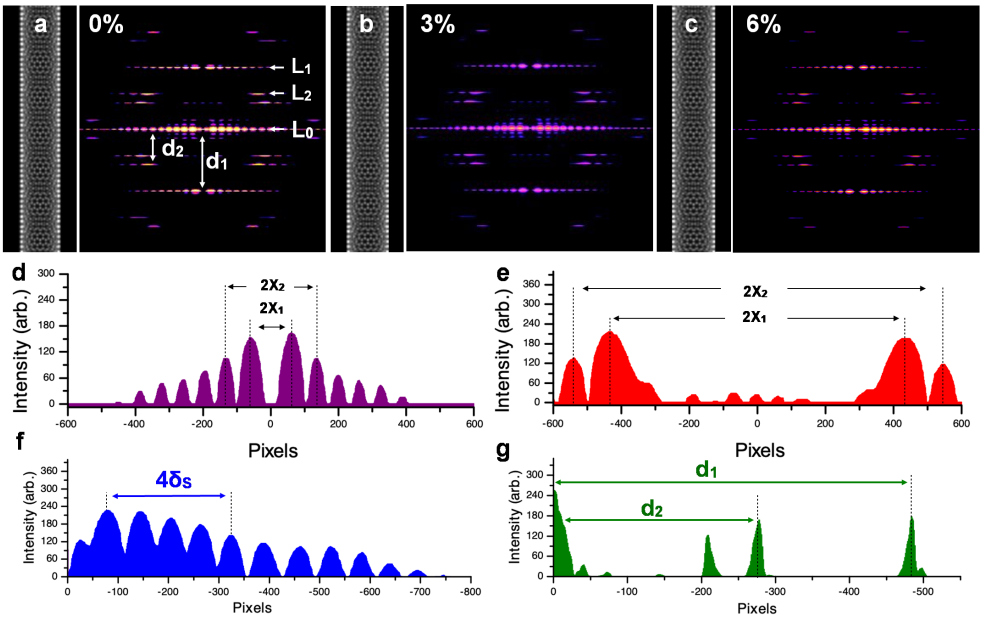

Figure 3.16: **Fourier transform analysis of simulated images.** (a) Simulation image of a (20, 2) nanotube and its Fourier transform. (b-c) simulated images of 3% and 6% radially compressed (20, 2) SWCNTs and their corresponding FTs, respectively. (d-e) The intensity profiles along the layer lines L_1 and L_2. (f) The intensity profile along the L_0 and (g) perpendicular to L_0. Figure based on Ref. [139].

wise, the reflection layer line spacing yields $n = 20 \pm 0.001$ and $m = 2 \pm 0.001$.

For the 3% and 6% radially compressed SWCNTs similar calculations were performed yielding $X_2/X_1 = 1.243 \pm 0.001$ and 1.223 ± 0.001 along L_2 and 2.209 ± 0.001 and 2.182 ± 0.001 along L_1, respectively. The best match for chiral indices in both cases was (20, 2) and the second best match was (21, 2). From relative layer line spacing we obtained $n = 20.32 \pm 0.01$ and $m = 1.97 \pm 0.01$ for 3% compressed SWCNT and $n = 20.52 \pm 0.01$ and $m = 1.94 \pm 0.01$ for 6 % compressed SWCNT. Hence, as expected, it appears that the layer line spacing is somewhat sensitive to radial deformations. Nonetheless, we can identify our example SWCNT at high confidence to be (20, 2) exhibiting only small amount of eccentricity. In case of unclear values of (n, m), however, it might be necessary to run extensive simulations to determine the correct structure. As an example of this, figure 3.17 presents the comparison between the experimental FT (figure 3.17 (a)) and the closest match-

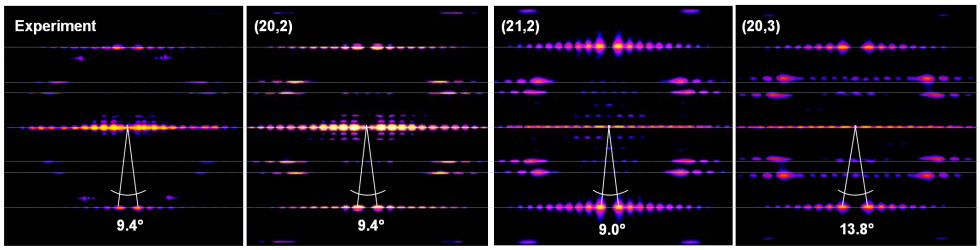

Figure 3.17: **Comparison of experimental and simulated FT images.** (a) The FT acquired from an experimental image of a (20, 2) nanotube. (b-c) FTs of simulated images of (20, 2) and (21, 2) SWCNTs, respectively and (d) the FT of a simulated (20, 3) SWCNT for comparison. Figure based on Ref. [139].

ing chiral indices (figures 3.17 (b) and (c)) obtained from simulations, showing that (20, 2) matches much better than (21, 2). The FT of a simulated (20, 3) SWCNT is also presented in figure 3.17 (d) for further comparison. Additionally, from the experimental and FT images given in figure 3.15 (a-c), the nominal diameter (D_N) of (20, 2) SWCNT was measured to be 16.51 Å and its chiral angle (Θ_{chiral}) to be 4.7°.

Using this method, the structure of any suspended SWCNT can be determined from an atomically-resolved high signal-to-noise ratio image. For example, the SWCNT in figure 3.18 (a) was determined to be a (19, 1) tube having expectedly a slightly smaller diameter of 15.28 Å. A particularly interesting example of a (6, 6) armchair SWCNT with an extremely small diameter of 8.18 Å is presented in figure 3.18 (b-c), apparently in perfect alignment with the underlying graphene lattice. Since FT represents the frequency components of a real-space experimental image in all directions, the orientation of any periodic configuration can be extracted from it. Based on this, we can calculate the relative orientation of graphene and SWCNT lattices – even though we can not distinguish between the contributions from top and bottom surfaces of the SWCNT – by measuring, e.g. the angles Θ_{chiral} and $\Theta_{armchair}$ (an angle between the tube axis and the closest graphene armchair edge) in Fourier space given in figure 3.15 (c). For example, the same (20, 2) SWCNT exhibits a helicity of 4.7°, indicating that the armchair edge is rotated by this amount with respect to the tube axis and from its FT image we can see that $\Theta_{armchair}$ is exactly 30°. As a result we get the misalignment angle of 25.3° for the (20, 2) SWCNT and 0° for the (6, 6) SWCNT.

Next, we carried out a systematic analysis of 24 distinct heterostructures for which we were able to reliably determine the corresponding

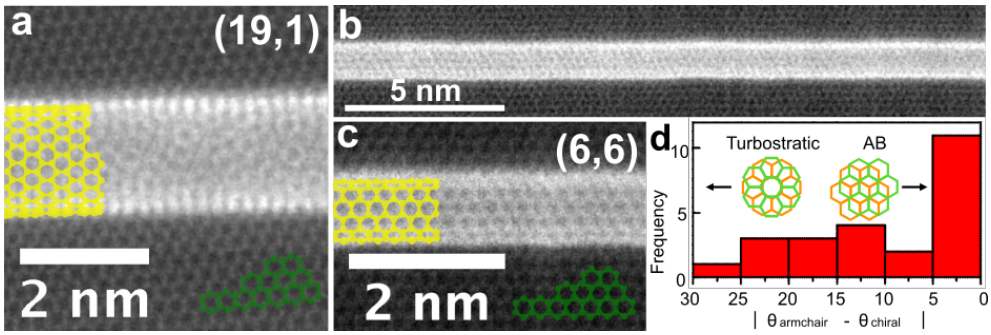

Figure 3.18: (a) A STEM MAADF image of a (19, 1) SWCNT. (b, c) A (6, 6) armchair SWCNT completely aligned by AB stacking with graphene, i.e. $|\theta_{armchair} - \theta_{chiral}| = 0°$. (a) A histogram of measured stacking angles for 24 different heterostructures. 30° represents turbostratic stacking and 0° AB stacking. Figure based on Ref. [139].

orientation angles by calculating $|\theta_{armchair} - \theta_{chiral}|$. The distribution plot of these angles is shown in figure 3.18 (d). Surprisingly, we observe a non-uniform distribution of the angles, with AB or Bernal type configuration being the energetically most favourable stack type, indicating a self-alignment in preferred orientation. The insets in figure 3.18 (d) illustrates the AB stacked and turbostratic structures. This result implies that, SWCNTs on monolayer graphene surface are not randomly oriented even though the deposition on substrate was random [83].

Even though nanotubes have been previously reported to grow epitaxially on graphite step edges [151], here we suggest that the possible explanation for this seemingly non-spontaneous behaviour of SWCNTs could be originating from the laser treatment procedure which is able to provide the required thermal energy for the nanotubes to self-align while at the same time removing the contamination. Approximately 55% of the heterostructures remain disordered, which could possibly be influenced by the residual contamination covering the nanotube junctions, such as those presented in figure 3.13 (c) (marked as anchor sites). Presumably nanotubes reach a (constrained) energy minimum within the potential landscape of graphene and align over relatively long distances in favoured orientation. Interestingly, the aligned SWCNTs not only possess the highest achievable symmetry but also make it possible to directly extract the nanotube handedness based on the graphene orientation [151].

3.2.3 Radial deformations, eccentricity and adsorption energy in SWCNT-graphene heterostructure

Van der Waals forces, being among the weakest intramolecular forces, are generally much weaker among the intramolecular bonds. Both graphene and carbon nanotubes are known to be mechanically strongest materials ever discovered [28], [152], therefore from scientific point of view, it is interesting to observe how the "strongest" materials interact with each other in the presence of "weakest" forces. The contact between the nanotubes and the graphene, governed by vdW forces, certainly induces structural and morphological changes for both materials. Precise knowledge of these changes backed by experimental results, plays an important role in understanding the physics of the nanotube-graphene heterostructure and further engineering of it. Here we explore this interaction and focus on the response of the graphene-SWCNT heterostructure to dispersion forces in detail. We first focus on the observations on carbon nanotubes and then move to graphene.

Although carbon nanotubes are known to have extremely high tensile strength and Young's modulus in axial direction [152], they are shown to be rather soft and flexible in radial (transversal) direction [153],[154], [155]. As a matter of fact, in a seminal study on molecular mechanics, it has been reported that vdW forces alone can induce radial deformations between two adjacent multi-walled carbon nanotubes [136]. There have also been several attempts to study radial deformations caused by substrate contact and environment and their influences on mechanical and electronic properties of SWCNTs [134], [156], [157], [158], [159], [160], [135]. Nevertheless, a comprehensive study of the radial deformations of SWCNTs are yet to be conducted. Majority of the experimental investigations have been limited to scanning probe techniques [134], [154], [161], [150], [162]. There are several drawbacks of this method, such as the problems caused by tip deconvolution, the vdW distance to the substrate, surface roughness [150] and the measurement being relatively invasive [160] and extremely demanding for structural determination [163]. In contrast, the heterostructures we present in this study provide the first atomically-resolved, clean view to study the SWCNT-graphene interface and its structure by using a convergent electron probe that is free of the above-mentioned hindering factors. Furthermore, thanks to the well-known lattice parameters of graphene, the image scale can be calibrated in Fourier space with high accuracy and consequently, the apparent diameter of nanotubes (D_A) can be obtained at sub- Å precision.

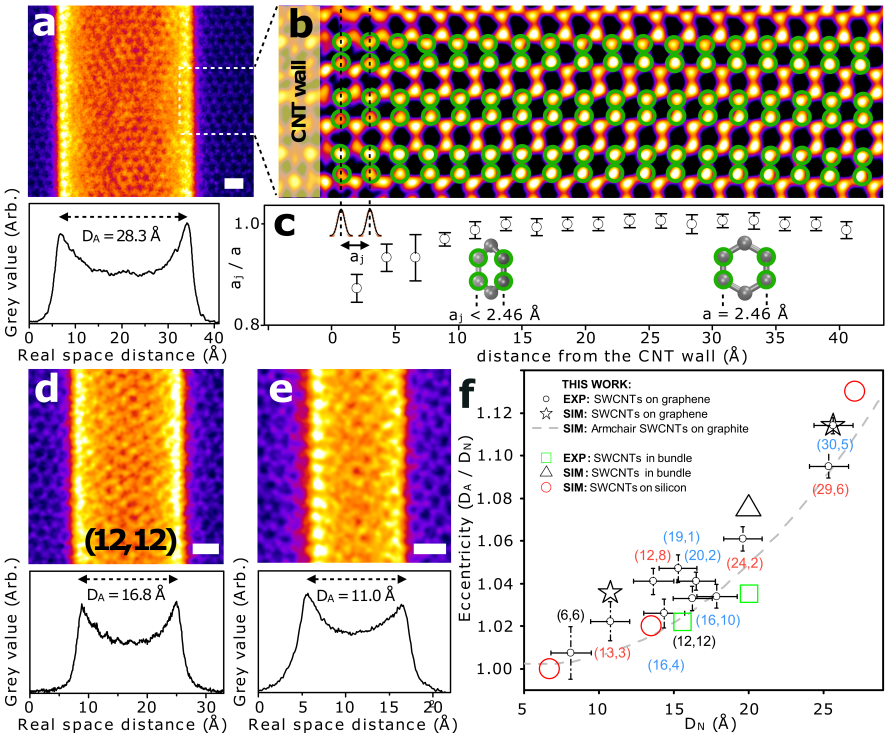

Figure 3.19: **Deformations in SWCNT** (a) STEM MAADF image of a large diameter (30, 5) SWCNT on graphene, with a line profile at the bottom, revealing its apparent diameter. (b) Fourier-filtered close-up image of graphene lattice next to the (30, 5) SWCNT with (c) corresponding interatomic distances a_j as a function of the distance from the SWCNT wall. (d-e) Close-up images of (12, 12) and (13, 3) tubes with their line profiles. (f) The calculated eccentricity($\varepsilon = D_A/D_N$) of SWCNTs suspended on monolayer graphene. All three scale bars have the same length of 0.4 nm. In figures (a), (b), (d) and (e) the ImajeJ lookup table "Fire" is applied, in order to enhance the contrast. Figure based on Ref. [139].

A radial deformation of a tube-shaped object can be characterized by its eccentricity (ε) which can be described as the ratio of the major and minor axes of the ellipse it forms. In this work, we use a slightly different definition of eccentricity (ε) such that

$$\varepsilon = D_A/D_N$$

where D_A is the apparent diameter and D_N represent the nominal diameter of the tube. For this direct comparison we have chosen three tubes

with chiral indices of (13, 3), (12, 12) and (30, 5) with nominal diameters of 10.79, 16.29 and 25.67 Å, shown in figures 3.19 (a), (d) and (e). Here, the contrasts of the high-resolution STEM MAADF images have been enhanced for better visualization. The chiral indices were determined using the method explained in the previous section. To determine the eccentricity of these SWCNTs, we analysed the wall separation by fitting the Gaussian line shapes to the nanotube cross-sectional intensity profiles that are shown below the real-space STEM images in figures 3.19 (a), (d) and (e). Here we observe that the small diameter (13, 3) nanotube appears quite rigid, undergoing only a small amount of deformation of $\varepsilon = 1.022$. The slightly larger (12, 12) nanotube exhibits respectively more flattening with an eccentricity of $\varepsilon = 1.033$. The highest deformation was observed in (30, 5) nanotube with an eccentricity of $\varepsilon = 1.114$. In total, we investigated the deformations in 10 different structurally identified SWCNTs, with the results gathered in figure 3.19 (f). Here, for comparison some experimental and computational results from the earlier studies are also included. Experimental results of SWCNTs in bundle from ref. [135] are marked with green rectangle and simulations of SWCNTs in bundle from ref. [134] are marked with black triangle, and simulations of SWCNTs on silicon substrate [136] are marked with red circle.

These results show that neither the electronic type of the nanotube (semiconducting or metallic) nor the chiral angle is correlated with the amount of deformation in SWCNTs, which is in good agreement with the earlier theoretical predictions [164]. Despite the accuracy of our method, however, the data given in figure 3.19 (f) shows large variation in eccentricity ε values. Surprisingly, compared to the data reported separately for bundled SWCNTs [135] or on bulk substrates [134], deformation of SWCNTs on graphene appears to be greater.

To understand this discrepancy, atomistic simulations were performed to investigate the adsorption of SWCNTs on both graphene and graphite. The details and parameters of the simulations are presented in section 2.4.2. Simulations were performed on (13, 3) and (30, 5) SWCNTs suspended on graphene which are marked with star symbols in figure 3.19 (f) and a number of armchair tubes suspended on graphite, as indicated by dashed lines. The simulation of graphite was imitated by completely fixing the monolayer graphene on its position. The graphene structure was oriented for each carbon nanotube such that it is commensurate with a single unit cell of the chiral nanotubes. This was necessary to enforce the periodic boundary conditions along the axis. The rotated graphene unit cell for the (13, 3) and (30, 5) tubes was multiplied perpendicular to the axis by 12 - and 28 - fold, respectively. As a result, the total width of

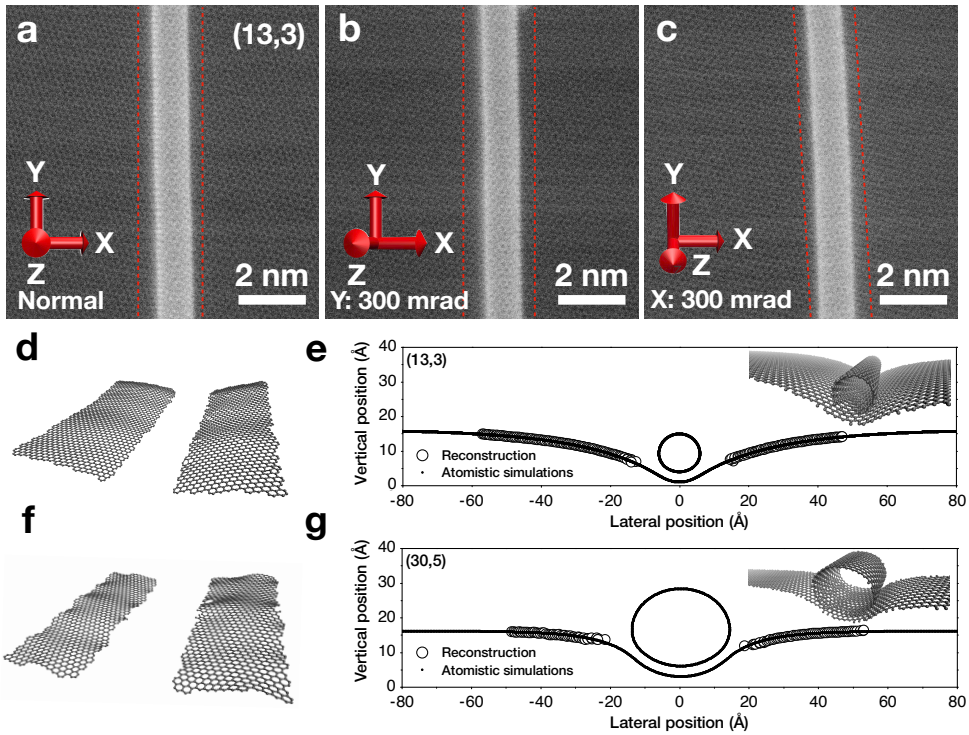

Figure 3.20: **Deformations in graphene** (a) Atomically-resolved, zero-tilt projection of the (13, 3) nanotube suspended on graphene. (b) Projection of the same site in (a) rotated around the x-axis by 300 mrad and (c) around the y-axis by 300 mrad. (d) Reconstructed model of graphene lattice around (13, 3) tube from two different viewpoints and (e) cross-section of fitted atomistic simulations. Inset shows the reconstructed 3D model. (f) Reconstructed graphene lattice around the (30, 5) nanotube and (g) corresponding fitted simulation image. Inset shows the 3D model. The experimental points in (e) and (g) are average positions of atoms perpendicular to the tube axis. Figure adapted from Ref. [139]

the graphene lattice for the (13, 3) nanotube was approximately 64 nm, and that for the (30, 5) tube was about 66 nm. To match the graphene curvature with the reconstructed results that we will discuss later, the bounding box of the cell was initially compressed by 0.7 and 0.8% for the (13, 3) and (30, 5) tubes, respectively, leaving the graphene under a negative strain and hence free to adapt to the adsorbed SWCNT. The eccentricity of the nanotubes was evaluated by comparing the diameters of a nanotube relaxed in a vacuum and on the surface.

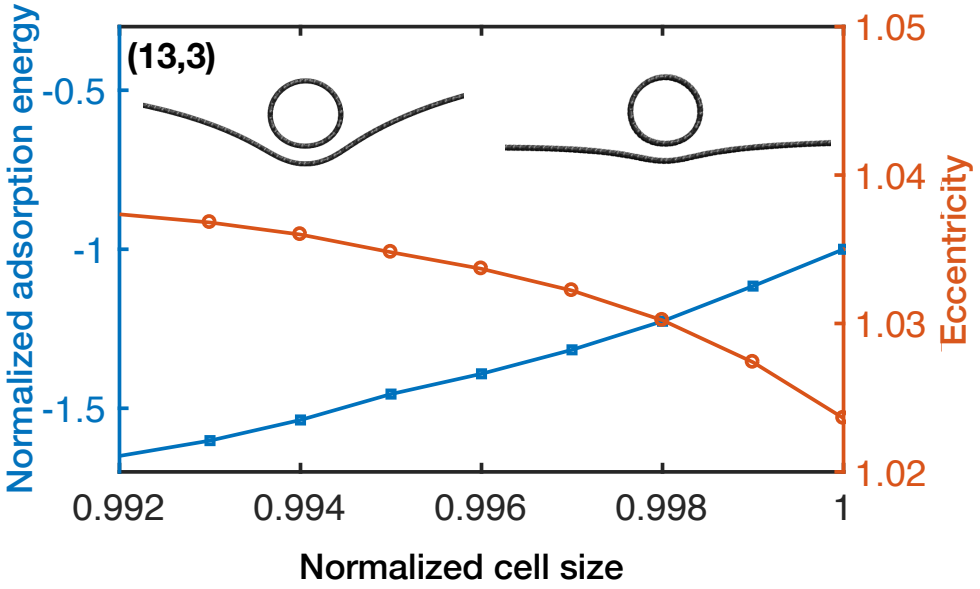

Figure 3.21: Normalized adsorption energy and eccentricity of a (13, 3) SWCNT on graphene monolayer as a function of normalized cell size. The insets show models of the extreme cases. Figure adapted from Ref. [139].

Interestingly, SWCNTs show larger deformations on graphene than on graphite, by $\varepsilon = 1.038$ vs 1.009 for (13, 3) tube and 1.110 vs 1.090 for (30, 5) tube. This seemingly counter-intuitive result is explained by an increase in binding energy on graphene, yielding 0.085 vs 0.176 eV/Å for (13, 3) tube and 0.205 vs 0.411 eV/Å for (30, 5) tube. This outcome is interpreted as a direct consequence of graphene minimizing its surface energy by partially folding around the nanotube as demonstrated in figure 3.20 (e-g). At this point, to calculate the adsorption energy of e.g. (13,3) nanotube, the pristine graphene supercell was compressed by 0.0 - 0.8 % to introduce negative strain. The width of the graphene area in the cell was the same as mentioned above (∼64 nm). After obtaining the adsorption energy values for compressed and non-compressed graphene cells, the energy values and cell size were normalized and the resulting graph is presented in figure 3.21. This graph shows that when the graphene is allowed to fold around the nanotube due to the negative strain, the nanotube exhibits larger deformation as evaluated by its eccentricity.

The observed eccentricity variation can be explained in a similar

way by stating that randomly oriented tubes on isotropically strained graphene experience minimum deformation, whereas in uniaxial strain makes it possible for graphene to bend perpendicular to the axis, with some of the nanotubes deviating from the curve. Apparently, the strain in the graphene membrane continuously varies both in direction and magnitude over the different areas of the specimen.

Next, we turn our attention to graphene, which in its ideal form is a perfectly two-dimensional crystal. Firstly, we analyze the carbon-carbon spacing in the graphene lattice at the vicinity of the carbon nanotubes. In a usual 2D projection, hexagonal network topology of graphene consists of carbon atoms uniformly separated from each other with a lattice constant of 2.46 Å and C-C-C bond angle of 120°. However, when the surface is curved, the projection of atoms changes systematically. This behaviour is schematically depicted in the lower part of figure 3.19 (c). In a projection from an ideally flat plane, the lattice constant of graphene is 2.46 Å whereas from a curved surface this value is less than 2.46 Å. For the analysis here, we chose the (30, 5) SWCNT shown in figure 3.19 (a) and used Fourier filtering by extracting the SWCNT components from the FT image to produce a clearer view of the atom positions of graphene lattice near the nanotube wall, as shown in figure 3.19 (b). From this filtered image we evaluated the interatomic distances by fitting Gaussian line-shapes to the intensity profiles of each atom, highlighted by the green circles in figure 3.19 (b). The resulting data is plotted in figure 3.19 (c). Here we observe that at the vicinity of the nanotube the apparent interatomic distances become smaller compared to the atomic distances on the right-hand side of the image (i.e far from the nanotube). This implies that near the contact point with nanotube graphene exhibits a local out-of-plane curvature extending ∼20 Å from the edge. The vertical direction of the inclination, however, can not be determined solely by this method.

3.2.4 Three-dimensional reconstruction of graphene lattice

To find out the topology of the curvature and the vertical direction of the inclination, an algorithm was used that has been developed recently [165]. This method requires recording atomic-resolution images of the sample from the same area under different tilt angles. The algorithm can obtain the 3D structure of a 2D material (in this case graphene) from a minimum of two projections with a relative sample tilt of about

15-20° during imaging. It identifies the positions of each atom within the 2D experimental projections and then finds the 3D structure that minimizes the difference between the acquired experimental images from different tilt angles and simulations of the structure through an optimisation process where both the atomic positions and the simulated imaging parameters are iteratively changed until the best result is achieved [165]. This was made possible by high-resolution STEM images where the location of each atom and their connections to nearest neighbours could be discerned.

Figures 3.20 (b) and (c) show the STEM images of the (13, 3) SWCNT on graphene recorded by rotating the sample separately around the x- and y- axis by 300 mrad (17.2°) relative to the zero-tilt position shown in figure 3.20 (a). By this method, only the structure of monolayer graphene can be unambiguously reconstructed, therefore the atom positions between the red dashed lines – where also the nanotubes lie – were omitted from the analysis. The resulting final 3D atomic model is presented in figure 3.20 (d). To recover the complete structure on the interface including the nanotube, several atomistic simulations were performed with varying degrees of strain in the monolayer graphene for simultaneously matching the result to experimental graphene curvature and SWCNT eccentricity as mentioned in 3.2.3. From the cross-section of the fitted atomistic simulation in figure 3.20 (e) it can be readily seen that a ∼14 Å deep 1D groove is formed which expands symmetrically on both sides of the nanotube. Here the experimental points represent the average vertical positions of atoms perpendicular to the nanotube axis. The reconstructed simulation image shown in the upper right corner of figure 3.20 (e) offers a 3D view of the curvature. The (30, 5) nanotube was also studied in a similar approach. The reconstructed lattice is shown in 3.20 (f) and the corresponding cross-section of the fitted simulation is given in 3.20 (g), with an inset showing the 3D reconstructed simulation image.

Lastly, we emphasize the extreme stability of these hybrid graphene-SWCNT nanostructures in our STEM experiments under the electron beam, presumably with an influence of high adsorption energies and strain in graphene. Just like a macroscopic membrane would strain by a mass that it supports, graphene also becomes slightly strained and as a result of this tension the mechanical vibrations of clean suspended regions are dampened, providing the heterostructures a stable environment to be imaged at resolutions higher than separately possible for either material as cleanly as in our examples. Due to the stability and strain-related reduced vibrations, individual atoms of the nanotubes embedded

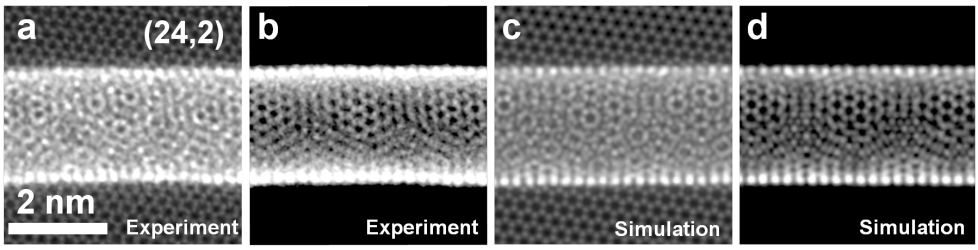

Figure 3.22: **Imaging stability of heterostructures** (a) A MAADF STEM image of a (24, 2) SWCNT suspended on graphene and (b) its Fourier-filtered version. (c) Simulation image of the (24, 2) SWCNT and (d) same simulation after removing the graphene lattice. The signal-to-noise ratio in (a, b) was improved by double Gaussian filtering [166]. Figure adapted from Ref. [139].

in hetero-interfaces can be resolved not just near the contact point, but along their entire length, unlike the vacuum-suspended SWCNTs [167]. This approach may be used to directly identify point defects at ambient temperature, as a complementary method to scanning probe techniques [168] , [163]. Here we present the exceptionally well-resolved images from arbitrary locations of the atomically clean structures along their entire length. Additionally, by removing the graphene lattice from these images using Fourier filtering, we can reveal a beautiful and high-quality view of SWCNT lattice where even the positions of the individual carbon atoms can be resolved along the tube axis. Figures 3.22 (a) and (b) show an example of such an image displaying a (24, 2) tube with and without the graphene lattice. These images are excellently well-resolved, showing obvious resemblance to the images obtained from simulations. Figures 3.22 (c) and (d) present the simulated versions of the (24, 2) nanotube.

In these simulations the best match with the experiment was realized by placing the carbon nanotube at a van der Waals distance of 0.34 nm from the graphene membrane (without optimizing the energy) and rotating the entire system by 5° around the principal axis perpendicular to the nanotube, followed by the electron beam arriving at the specimen plane at this angle. The chiral index, (24, 2), and the relative graphene orientation in the simulation were identified from the experimental images with the method described in 3.2.4. In 3.22 (d) to imitate the experimental contrast, the graphene lattice was first included in the simulations and afterwards removed manually by using Fourier filtering.

3.2.5 Conclusion

In this study, using monolayer graphene and single-walled carbon nanotube as building blocks, we synthesized a 1D/2D mixed-dimensional heterostructure held together by vdW forces and investigated the atomic-scale deformations at the molecular interface. After thermal annealing by laser irradiation, we observe that the structures self-align and thereby optimize the stacking of the lower nanotube wall with the underlying graphene lattice. Furthermore, we find that both carbon nanotubes and graphene deform as a result of the van der Waals forces, resulting in one-dimensional corrugations in the graphene lattice. The hybrid structure exhibits interesting topographical features, with nanotubes dipping into the supporting graphene layer, creating ordered, long-range, one-dimensional grooves that reduce the surface energy of the heterostructure. The three-dimensional structure of the lattice can be constructed with the help of multiple rotated projections, and when correlated with atomistic simulations the morphology of the complete structure of the interface can be restored. The graphene support enables the nanotubes to be visualized along their entire length at room temperature with high accuracy that was previously possible only with scanning probe techniques on rigid substrates. Our study sheds light on the substrate-induced deformations, and as a complete novelty, on the deformation induced by an adsorbed object in free-standing graphene. Alignment and deformations together result in a well defined 1D perturbation of the 2D material, and in a very clean and stable hybrid system that could be studied at atomic resolution along its entire length.

Chapter 4

Summary

4.1 Summary of the results

Carbon nanostructures including fullerenes, nanotubes and graphene, have been among the most studied structures in material science during last decades. In particular, graphene provides a new platform for building novel mixed-dimensional hybrid structures efficiently with zero- and one-dimensional nanomaterials due to its environmental stability and matured production and processing techniques. In this thesis we introduce two carbon based mixed-dimensional van der Waals heterostructures; a novel 0D/2D buckyball sandwich and 1D/2D graphene-single walled carbon nanotube hetero-interface.

The first part of the "Results" chapter is based on the novel suspended buckyball sandwich heterostructures – encapsulated C_{60} between two single-layer graphene. The resulting sandwich structures provide atomically clean areas to study fullerene islands and individual molecules through high-resolution transmission electron microscopy which we attribute to graphene encapsulation. First we started with a confirmation that the C_{60} structures are located indeed in sandwich structure, i.e. between two monolayer graphene sheets by electron diffraction, Raman spectroscopy and STEM image analysis. We then studied multilayer regions of the sandwich structure and revealed that molecules of multilayered fullerenes self-assemble into hexagonally closed-packed ABA and ABC stacked structures on graphene monolayer following either the zigzag or the armchair direction of graphene lattice.

Next we investigated the C_{60} monolayers in detail, provided atomically-resolved, high-quality STEM images and image sequences of these monolayers. Generally we observed remarkable stability of the sandwiched

structures under the electron irradiation compared to non-sandwiched samples. We measured the lattice spacing in C_{60} monolayers and found slightly different value (∼4-5% shorter) than the reported lattice constant for bulk C_{60} crystals, which was also confirmed by the simulations.

We further concentrated on understanding the atomic-scale structure and dynamics of the C_{60} molecules in monolayer. Our results showed that individual C_{60} molecules are exceptionally mobile under the electron beam at the edges of the fullerene monolayer. We also observed the diffusion of individual molecules and found that they were actively rotating during room temperature experiments. Furthermore, during continuous e-beam irradiation, some C_{60} molecules first bonded with adjacent neighbours to form dimers and then fused peanut-like structures, which seem to rotate around the joint axis. This movement is hindered only for polymerized structures containing three or more molecules.

This work has shown that, beside offering a new platform for synthesis of new nanomaterials, graphene provides a partial shield against irradiation damage, a 2D nanoscale reaction chamber and a "clean view" for the STEM experiments.

In the second part of the "Results" chapter we studied single-walled carbon nanotubes suspended on single-layer graphene as a model system of a 1D/2D molecular interface through atomic-resolution STEM imaging. Here, we investigated in detail how the nanotubes stack onto graphene and how the adsorption changes the morphology of both materials.

We first discussed the fabrication of the samples and efficiency of the sample cleaning technique. Based on the initial STEM micrographs we could already distinguish the well-aligned nanotubes spanning hundreds of nanometers. We then discussed the methodology to determine the chiral indices (n, m) of nanotubes and explained the procedure on how we obtain the chiral indices directly from the real space projections and their Fourier transforms thanks to our atomically-resolved sharp STEM images.

Next we presented the result of our systematic analysis of several nanotubes to determine the relative orientation angles of nanotubes on graphene lattice. We found that SWCNTs align on the surface in accordance with the symmetry of graphene, presumably to optimize the stacking of their lower wall with underlying lattice. We attribute the self-order of nanotubes on ultra-clean graphene regions to thermal excitation during the laser cleaning.

Furthermore, we studied separately the atomic-scale deformation of the carbon nanotubes and graphene as a response to dispersion forces.

We used the eccentricity of the tubes in a redefined way to characterize the amount of the radial deformation. Our results showed that the deformation in SWCNTs are strain-correlated but show no sensitivity to helicity, electronic structure, or stacking type.

Systematic analysis of atomic distances in the graphene lattice around the nanotube contact wall revealed the out-of-plane curved structure of graphene. Through 3D reconstruction of the interface, we found that graphene partially folded around the suspended nanotube molecules as a result of the interplay between vdW and elastic energies which allows the interfaces to maximize their contact areas and minimize the total energy of the system. The dampened mechanical vibrations due to the slightly strained and curved graphene allowed the heterostructure to be viewed clearly at a high-resolution. Finally we presented exceptionally well-resolved STEM images of carbon nanotubes showing their structure in atomic detail. This work has shown that, despite the random deposition of the nanotubes, the competition between the dvW forces and strain results in aligned molecular interfaces.

4.2 Outlook and future work

The results presented in this study provide important implications for developing carbon-based organic devices using graphene template in the future. The sandwiching method can be used for further investigation of other materials instead of fullerenes or beam-sensitive nanoparticles to study and analyse them under electron microscopy. This technique opens a way to reveal structure and dynamics of many other materials and understand their behaviour at the atomic-scale. A possible application of the graphene-C_{60} hybrid heterostructure could be adding alkali-metals to the sandwich structure in order to refresh the superconductivity research on fullerenes. Since the C_{60} monolayer growth parameters are known and the sample preparation can be controlled better, the stable structure of fullerenes in sandwich structure can enhance the alkali-metal-doping process of C_{60}. The sandwiching of fullerenes can also be used to trap other molecules inside the cage of stabilized fullerenes to study them in STEM between quasi-transparent graphene layers. For this purpose the synthesis of rotationally-locked fullerene sandwich structure would be of great interest. Even though it might be very challenging, the realization of free-standing monolayer C_{60} could also be added to our to-do list.

Carbon nanostructures are still strongly investigated and are under the spotlights of science and research community due to their distinctive

electronic and physical properties as well as their potential use for the development of electronic, photonic and optoelectronic nano-devices with diverse functionality. The realization of these devices can only be possible by understanding the fundamentals of these nanomaterials and by being able to control their structure and behaviour on the molecular and atomic scale. This study enables us to elucidate the method of synthesis and characterization of the the mixed-dimensional carbon materials as well as to study and control their behaviour in the atomic level and preparation on a large scale, which paves the way for developing new generation technology.

Bibliography

[1] H. Kroto, J. Heath, S. Obrien, R. Curl, and R. Smalley, "C_{60}: Buckminsterfullerene," *Nature*, vol. 318, pp. 162–163, 1985.

[2] S. Iijima, "Helical microtubules of graphitic carbon," *Nature*, vol. 354, pp. 56–58, 1991.

[3] S. Iijima and T. Ichihashi, "Single-shell carbon nanotubes of 1-nm diameter," *Nature*, vol. 363, pp. 603–605, 1993.

[4] P. R. Wallace, "The Band Theory of Graphite," *Phys. Rev.*, vol. 71, pp. 622–634, 1947.

[5] A. Geim and I. Grigorieva, "Van der Waals heterostructures," *Nature*, vol. 499, pp. 419–425, 2013.

[6] D. Jariwala, T. Marks, and M. Hersam, "Mixed-Dimensional van der Waals Heterostructures," *Nature Materials*, vol. 16, pp. 170–181, 2016.

[7] B. W. Smith, M. Monthioux, and D. Luzzi, "Encapsulated C_{60} in carbon nanotubes," *Nature*, vol. 396, pp. 323–324, 1998.

[8] B. W. Smith and D. E. Luzzi, "Formation mechanism of fullerene peapods and coaxial tubes: a path to large scale synthesis," *Chemical Physics Letters*, vol. 321, no. 1, pp. 169–174, 2000.

[9] Q. H. Wang, D. O. Bellisario, L. W. Drahushuk, R. M. Jain, S. Kruss, M. P. Landry, S. G. Mahajan, S. F. E. Shimizu, Z. W. Ulissi, and M. S. Strano, "Low Dimensional Carbon Materials for Applications in Mass and Energy Transport," *Chemistry of Materials*, vol. 26, no. 1, pp. 172–183, 2014.

[10] H. R. Barzegar, E. Gracia-Espino, A. Yan, C. Ojeda-Aristizabal, G. Dunn, T. Wågberg, and A. Zettl, "C_{60}/Collapsed Carbon Nanotube Hybrids: A Variant of Peapods," *Nano Letters*, vol. 15, no. 2, pp. 829–834, 2015.

[11] M. Fuhrer, J. Hou, X.-D. Xiang, and A. Zettl, "C_{60} intercalated graphite: Predictions and experiments," *Solid State Communications*, vol. 90, no. 6, pp. 357–360, 1994.

[12] S. Saito and A. Oshiyama, "Design of C_{60}-graphite cointercalation compounds," *Phys. Rev. B*, vol. 49, pp. 17413–17419, 1994.

[13] V. Gupta, P. Scharff, K. Risch, H. Romanus, and R. Müller, "Synthesis of C_{60} intercalated graphite," *Solid State Communications*, vol. 131, no. 3, pp. 153–155, 2004.

[14] A. Hebard, M. Rosseinsky, R. Haddon, D. Murphy, S. Glarum, T. Palstra, A. Ramirez, and A. Kortan, "Superconductivity at 18 K in potassium-doped C_{60}," *Nature*, vol. 350, pp. 600–601, 1991.

[15] K. Tanigaki, T. Ebbesen, S. Saito, J. Mizuki, J. Tsai, Y. Kubo, and S. Kuroshima, "Superconductivity at 33 K in CsxRbyC_{60}," *Nature*, vol. 352, pp. 222–223, 1991.

[16] A. R. Kortan, N. Kopylov, S. Glarum, E. Gyorgy, A. Ramirez, R. Fleming, F. Thiel, and R. Haddon, "Superconductivity at 8.4 K in calcium-doped C_{60}," *Nature*, vol. 355, pp. 529–532, 1992.

[17] A. Khlobystov, "Carbon nanotubes: From Nano Test Tube to Nano-Reactor," *ACS Nano*, vol. 5, no. 12, pp. 9306–9312, 2011.

[18] J. C. Meyer, F. Eder, S. Kurasch, V. Skakalova, J. Kotakoski, H. J. Park, S. Roth, A. Chuvilin, S. Eyhusen, G. Benner, A. V. Krasheninnikov, and U. Kaiser, "Accurate measurement of electron beam induced displacement cross sections for single-layer graphene," *Phys. Rev. Lett.*, vol. 108, 196102, 2012.

[19] T. Susi, C. Hofer, G. Argentero, G. Leuthner, T. Pennycook, C. Mangler, J. Meyer, and J. Kotakoski, "Isotope analysis in the transmission electron microscope," *Nature Communications*, vol. 7, 13040, 2016.

[20] Q. H. Wang and M. Hersam, "Room-temperature molecular-resolution characterization of self-assembled organic monolayers on epitaxial graphene," *Nature Chemistry*, vol. 1, pp. 206–211, 2009.

[21] S. Sato, T. Yamasaki, and H. Isobe, "Solid-state structures of peapod bearings composed of finite single-wall carbon nanotube and fullerene molecules," *Proceedings of the National Academy of Sciences*, vol. 111, no. 23, pp. 8374–8379, 2014.

[22] P. Utko, J. Nygård, M. Monthioux, and L. Noé, "Sub-Kelvin transport spectroscopy of fullerene peapod quantum dots," *Applied Physics Letters*, vol. 89, no. 23, 233118, 2006.

[23] K. S. Novoselov, A. K. Geim, S. V. Morozov, D. Jiang, Y. Zhang, S. V. Dubonos, I. V. Grigorieva, and A. A. Firsov, "Electric Field Effect in Atomically Thin Carbon Films," *Science*, vol. 306, no. 5696, pp. 666–669, 2004.

[24] R. Peierls, "Quelques propriétés typiques des corps solides," *Annales de l'institut Henri Poincaré*, vol. 5, no. 3, pp. 177–222, 1935.

[25] L. D. Landau, "Zur Theorie der Phasenumwandlungen II," *Phys. Z. Sowjetunion*, vol. 11, pp. 26–35, 1937.

[26] N. D. Mermin, "Crystalline Order in Two Dimensions," *Phys. Rev.*, vol. 176, pp. 250–254, 1968.

[27] J. C. Meyer, A. K. Geim, M. I. Katsnelson, K. S. Novoselov, T. J. Booth, and S. Roth, "The structure of suspended graphene sheets," *Nature*, vol. 446, pp. 60–63, 2007.

[28] C. Lee, X. Wei, J. Kysar, and J. Hone, "Measurement of the Elastic Properties and Intrinsic Strength of Monolayer Graphene," *Science*, vol. 321, pp. 385–388, 2008.

[29] A. A. Balandin, S. Ghosh, W. Bao, I. Calizo, D. Teweldebrhan, F. Miao, and C. N. Lau, "Superior Thermal Conductivity of Single-Layer Graphene," *Nano Letters*, vol. 8, no. 3, pp. 902–907, 2008.

[30] K. Bolotin, K. Sikes, Z. Jiang, M. Klima, G. Fudenberg, J. Hone, P. Kim, and H. Stormer, "Ultrahigh electron mobility in suspended graphene," *Solid State Communications*, vol. 146, no. 9, pp. 351–355, 2008.

[31] X. Du, I. Skachko, A. Barker, and E. Andrei, "Approaching ballistic transport in suspended graphene," *Nature Nanotechnology*, vol. 3, no. 8, pp. 491–495, 2008.

[32] A. H. Castro Neto, F. Guinea, N. M. R. Peres, K. S. Novoselov, and A. K. Geim, "The electronic properties of graphene," *Rev. Mod. Phys.*, vol. 81, pp. 109–162, 2009.

[33] F. D. M. Haldane, "Model for a Quantum Hall Effect without Landau Levels: Condensed-Matter Realization of the "Parity Anomaly"," *Phys. Rev. Lett.*, vol. 61, pp. 2015–2018, 1988.

[34] M. Katsnelson, K. S. Novoselov, and A. K. Geim, "Chiral tunneling and the Klein paradox in graphene," *Nature Physics*, vol. 2, pp. 620–625, 2006.

[35] B. David, R. Ibberson, J. Matthewman, K. Prassides, T. J. S. Dennis, J. Hare, H. Kroto, R. Taylor, and D. Walton, "Crystal structure and bonding of ordered C_{60}," *Nature*, vol. 353, pp. 147–149, 1991.

[36] K. Herdberg, L. Herdberg, D. S. Bethune, C. A. Brown, H. C. Dorn, R. D. Johnson, and M. De Vries, "Bond Lengths in Free Molecules of Buckminsterfullerene, C_{60}, from Gas-Phase Electron Diffraction," *Science*, vol. 254, no. 5030, pp. 410–412, 1991.

[37] D. H. Parker, P. Wurz, K. Chatterjee, K. R. Lykke, J. E. Hunt, M. J. Pellin, J. C. Hemminger, D. M. Gruen, and L. M. Stock, "High-yield synthesis, separation, and mass-spectrometric characterization of fullerenes C_{60} to C_{266}," *Journal of the American Chemical Society*, vol. 113, no. 20, pp. 7499–7503, 1991.

[38] W. A. Scrivens and J. M. Tour, "Synthesis of gram quantities of C_{60} by plasma discharge in a modified round-bottomed flask. Key parameters for yield optimization and purification," *The Journal of Organic Chemistry*, vol. 57, no. 25, pp. 6932–6936, 1992.

[39] S. Kitazawa, H. Abe, and S. Yamamoto, "Formation of nanostructured solid-state carbon particles by laser ablation of graphite in isopropyl alcohol," *Journal of Physics and Chemistry of Solids*, vol. 66, pp. 555–559, 2005.

[40] T. Rabenau, R. Kremer, and E. Sohmen, "The energy gaps of fullerene C_{60} and C_{70} determined from the temperature dependent microwave conductivity," *Zeitschrift für Physik B Condensed Matter*, vol. 90, pp. 69–72, 1993.

[41] C. Chen, L. Tjeng, P. Rudolf, G. Meigs, J. Rowe, J. Chen, J. Mccauley, A. III, A. McGhie, W. Romanow, and E. Plummer, "Electronic states and phases of K_xC_{60} from photoemission and X-ray absorption spectroscopy," *Nature*, vol. 352, pp. 603–605, 1991.

[42] L. Tutt and A. Kost, "Optical limiting performance of C_{60} and C_{70} solutions," *Nature*, vol. 356, pp. 225–226, 1992.

[43] P.-M. Allemand, K. Khemani, A. Koch, F. Wudl, K. Holczer, S. Donovan, G. Gruner, and J. Thompson, "Organic Molecular Soft Ferromagnetism in a Fullerene C_{60}," *Science*, vol. 253, pp. 301–302, 1991.

[44] F. Wudl and J. D. Thompson, "Buckminsterfullerene C_{60} and organic ferromagnetism," *Journal of Physics and Chemistry of Solids*, vol. 53, no. 11, pp. 1449–1455, 1992.

[45] G. Lalwani and B. Sitharaman, "Multifunctional Fullerene- and Metallofullerene-Based Nanobiomaterials," *Nano LIFE*, vol. 3, 1342003, 2013.

[46] J. W. Mintmire, B. I. Dunlap, and C. T. White, "Are fullerene tubules metallic?," *Phys. Rev. Lett.*, vol. 68, pp. 631–634, 1992.

[47] R. Saito, M. Fujita, G. Dresselhaus, and M. S. Dresselhaus, "Electronic structure of graphene tubules based on C_{60}," *Phys. Rev. B*, vol. 46, pp. 1804–1811, 1992.

[48] N. Hamada, S.-i. Sawada, and A. Oshiyama, "New one-dimensional conductors: Graphitic microtubules," *Phys. Rev. Lett.*, vol. 68, pp. 1579–1581, 1992.

[49] C. Staii, A. T. Johnson, M. Chen, and A. Gelperin, "DNA-Decorated Carbon Nanotubes for Chemical Sensing," *Nano Letters*, vol. 5, no. 9, pp. 1774–1778, 2005.

[50] C. E. Banks, T. J. Davies, G. G. Wildgoose, and R. G. Compton, "Electrocatalysis at graphite and carbon nanotube modified electrodes: edge-plane sites and tube ends are the reactive sites," *Chem. Commun.*, pp. 829–841, 2005.

[51] M. Scarselli, P. Castrucci, and M. D. Crescenzi, "Electronic and optoelectronic nano-devices based on carbon nanotubes," *Journal of Physics: Condensed Matter*, vol. 24, no. 31, 313202, 2012.

[52] V. N. Popov, "Carbon nanotubes: properties and application," *Materials Science and Engineering: R: Reports*, vol. 43, no. 3, pp. 61–102, 2004.

[53] E. Pop, D. Mann, Q. Wang, K. Goodson, and H. Dai, "Thermal conductance of an individual single-wall carbon nanotube above room temperature," *Nano Letters*, vol. 6, 1, pp. 96–100, 2006.

[54] J. A. Misewich, R. Martel, P. Avouris, J. C. Tsang, S. Heinze, and J. Tersoff, "Electrically induced optical emission from a carbon nanotube fet," *Science*, vol. 300, no. 5620, pp. 783–786, 2003.

[55] J. Chen, V. Perebeinos, M. Freitag, J. Tsang, Q. Fu, J. Liu, and P. Avouris, "Bright infrared emission from electrically induced excitons in carbon nanotubes," *Science*, vol. 310, no. 5751, pp. 1171–1174, 2005.

[56] M. Freitag, Y. Martin, J. A. Misewich, R. Martel, and P. Avouris, "Photoconductivity of single carbon nanotubes," *Nano Letters*, vol. 3, no. 8, pp. 1067–1071, 2003.

[57] Z. K. Tang, L. Zhang, N. Wang, X. X. Zhang, G. H. Wen, G. D. Li, J. N. Wang, C. T. Chan, and P. Sheng, "Superconductivity in 4 Angstrom Single-Walled Carbon Nanotubes," *Science*, vol. 292, no. 5526, pp. 2462–2465, 2001.

[58] A. Hirsch, "The era of carbon allotropes," *Nature Materials*, vol. 9, pp. 868–71, 2010.

[59] W. Ren and H.-M. Cheng, "The global growth of graphene," *Nature Nanotechnology*, vol. 9, pp. 726–730, 2014.

[60] Q. H. Wang, K. Kalantar-zadeh, A. Kis, J. Coleman, and M. Strano, "Electronics and optoelectronics of two-dimensional transition metal dichalcogenides," *Nature Nanotechnology*, vol. 7, pp. 699–712, 2012.

[61] M. Xu, T. Liang, M. Shi, and H. Chen, "Graphene-Like Two-Dimensional Materials," *Chemical reviews*, vol. 113, no. 5, pp. 3766–3798, 2013.

[62] S. Z. Butler, S. M. Hollen, L. Cao, Y. Cui, J. A. Gupta, H. R. Gutiérrez, T. F. Heinz, S. S. Hong, J. Huang, A. F. Ismach,

E. Johnston-Halperin, M. Kuno, V. V. Plashnitsa, R. D. Robinson, R. S. Ruoff, S. Salahuddin, J. Shan, L. Shi, M. G. Spencer, M. Terrones, W. Windl, and J. E. Goldberger, "Progress, Challenges, and Opportunities in Two-Dimensional Materials Beyond Graphene," *ACS Nano*, vol. 7, no. 4, pp. 2898–2926, 2013.

[63] L. de Broglie, "Recherches sur la théorie des quanta," *PhD Thesis*, 1924.

[64] H. Busch, "Berechnung der Bahn von Kathodenstrahlen im axialsymmetrischen elektromagnetischen Felde," *Annalen der Physik*, vol. 386, no. 25, pp. 974–993, 1926.

[65] E. Ruska, "The Development of the Electron Microscope and of Electron Microscopy (Nobel Lecture)," *Angewandte Chemie International Edition in English*, vol. 26, no. 7, pp. 595–605, 1987.

[66] U. Kaiser, J. Biskupek, J. Meyer, J. Leschner, L. Lechner, H. Rose, M. Stöger-Pollach, A. Khlobystov, P. Hartel, H. Müller, M. Haider, S. Eyhusen, and G. Benner, "Transmission electron microscopy at 20kV for imaging and spectroscopy," *Ultramicroscopy*, vol. 111, no. 8, pp. 1239–1246, 2011.

[67] S. Pennycook and P. Nellist, "Scanning transmission electron microscopy: Imaging and Analysis," *Springer New York*, 2011.

[68] D. B. Williams and C. B. Carter, "Transmission Electron Microscopy a Textbook for Materials Science," *Springer US*, 2009.

[69] O. Scherzer, "Über einige Fehler von Elektronenlinsen," *Zeitschrift für Physik*, vol. 101, no. 9, pp. 593–603, 1936.

[70] O. Scherzer, "Sphärische und chromatische Korrektur von Elektronen-Linsen," *Optik*, vol. 2, pp. 114–132, 1947.

[71] O. Krivanek, N. Delby, A. Spence, R. Camps, and L. Brown, "Aberration correction in the STEM," *Inst. Phys. Conf. Ser. 153 (Proceedings EMAG meeting, Cambridge 1997)*, pp. 35–40, 1997.

[72] M. Haider, S. Uhlemann, E. Schwan, H. Rose, B. Kabius, and K. Urban, "Electron microscopy image enhanced," *Nature*, vol. 392, no. 6678, pp. 768–769, 1998.

[73] I. MacLaren and Q. M. Ramasse, "Aberration-corrected scanning transmission electron microscopy for atomic-resolution studies of functional oxides," *International Materials Reviews*, vol. 59, no. 3, pp. 115–131, 2014.

[74] A. Muller and J. Grazul, "Optimizing the environment for sub-0.2 nm scanning transmission electron microscopy," *Journal of Electron Microscopy*, vol. 50, no. 3, pp. 219–226, 2001.

[75] O. L. Krivanek, G. J. Corbin, N. Dellby, B. F. Elston, R. J. Keyse, M. F. Murfitt, C. S. Own, Z. S. Szilagyi, and J. W. Woodruff, "An electron microscope for the aberration-corrected era.," *Ultramicroscopy*, vol. 108, no. 3, pp. 179–195, 2008.

[76] C. Raman and K. Krishnan, "A new type of secondary radiation," *Nature*, vol. 121, no. 3048, pp. 501–502, 1928.

[77] D. Basko, S. Piscanec, and A. Ferrari, "Electron-electron interactions and doping dependence of the two-phonon Raman intensity in graphene," *Physical Review B*, vol. 80, 16, 165413, 2009.

[78] A. Ferrari, J. Meyer, V. Scardaci, C. Casiraghi, M. Lazzeri, F. Mauri, S. Piscanec, D. Jiang, K. Novoselov, S. Roth, and A. Geim, "Raman Spectrum of Graphene and Graphene Layers," *Physical review letters*, vol. 97, 187401, 2006.

[79] H. Kuzmany, R. Pfeiffer, M. Hulman, and C. Kramberger, "Raman spectroscopy of fullerenes and fullerene-nanotube composites," *Philosophical transactions. Series A, Mathematical, physical, and engineering sciences*, vol. 362, pp. 2375–406, 2004.

[80] X. Li, W. Cai, J. An, S. Kim, J. Nah, D. Yang, R. Piner, A. Velamakanni, I. Jung, E. Tutuc, S. Banerjee, L. Colombo, and R. Ruoff, "Large-Area Synthesis of High-Quality and Uniform Graphene Films on Copper Foils," *Science*, vol. 324, pp. 1312–1314, 2009.

[81] K. Mustonen, P. Laiho, A. Kaskela, Z. Zhu, O. Reynaud, N. Houbenov, Y. Tian, T. Susi, H. Jiang, A. Nasibulin, and E. Kauppinen, "Gas phase synthesis of non-bundled, small diameter single-walled carbon nanotubes with near-armchair chiralities," *Applied Physics Letters*, vol. 107, 013106, 2015.

[82] A. Hussain, Y. Liao, Q. Zhang, E.-X. Ding, P. Laiho, S. Ahmad, N. Wei, Y. Tian, H. Jiang, and E. I. Kauppinen, "Floating catalyst

CVD synthesis of single walled carbon nanotubes from ethylene for high performance transparent electrodes," *Nanoscale*, vol. 10, pp. 9752–9759, 2018.

[83] P. Laiho, K. Mustonen, Y. Ohno, S. Maruyama, and E. Kauppinen, "Dry and direct deposition of aerosol synthesized single-walled carbon nanotubes by thermophoresis," *ACS Applied Materials and Interfaces*, vol. 9, 24, pp. 20738–20747, 2017.

[84] M. Tripathi, A. Mittelberger, K. Mustonen, C. Mangler, J. Kotakoski, J. C. Meyer, and T. Susi, "Cleaning graphene: Comparing heat treatments in air and in vacuum," *physica status solidi (RRL) – Rapid Research Letters*, vol. 11, no. 8, 1700124, 2017.

[85] S. Plimpton, "Fast parallel algorithms for short-range molecular dynamics," *Journal of Computational Physics*, vol. 117, no. 1, pp. 1–19, 1995.

[86] S. J. Plimpton and A. P. Thompson, "Computational aspects of many-body potentials," *MRS Bulletin*, vol. 37, no. 5, pp. 513–521, 2012.

[87] T. O'Connor, J. Andzelm, and M. Robbins, "AIREBO-M: A reactive model for hydrocarbons at extreme pressures," *The Journal of chemical physics*, vol. 142, 024903, 2015.

[88] D. W. Brenner, "Empirical potential for hydrocarbons for use in simulating the chemical vapor deposition of diamond films," *Phys. Rev. B*, vol. 42, pp. 9458–9471, 1990.

[89] V. R. Cooper, "Van der Waals density functional: An appropriate exchange functional," *Phys. Rev. B*, vol. 81, 161104, 2010.

[90] K. Lee, E. D. Murray, L. Kong, B. I. Lundqvist, and D. C. Langreth, "Higher-accuracy van der Waals density functional," *Phys. Rev. B*, vol. 82, 081101, 2010.

[91] A. H. Larsen, M. Vanin, J. J. Mortensen, K. S. Thygesen, and K. W. Jacobsen, "Localized atomic basis set in the projector augmented wave method," *Phys. Rev. B*, vol. 80, 195112, 2009.

[92] M. Koshino, Y. Niimi, E. Nakamura, H. Kataura, T. Okazaki, K. Suenaga, and S. Iijima, "Analysis of the reactivity and selectivity of fullerene dimerization reactions at the atomic level," *Nature chemistry*, vol. 2, pp. 117–24, 2010.

[93] M. Terrones, "Transmission electron microscopy: Visualizing fullerene chemistry," *Nature Chemistry*, vol. 2, pp. 82–83, 2010.

[94] K. Kim, T. H. Lee, E. J. G. Santos, P. S. Jo, A. Salleo, Y. Nishi, and Z. Bao, "Structural and Electrical Investigation of C_{60}–Graphene Vertical Heterostructures," *ACS Nano*, vol. 9, no. 6, pp. 5922–5928, 2015.

[95] G. Li, H. T. Zhou, L. D. Pan, Y. Zhang, J. H. Mao, Q. Zou, H. M. Guo, Y. L. Wang, S. X. Du, and H.-J. Gao, "Self-assembly of C_{60} monolayer on epitaxially grown, nanostructured graphene on Ru(0001) surface," *Applied Physics Letters*, vol. 100, 013304, 2012.

[96] X. Ye, M. Jones, L. Frechette, Q. Chen, A. Powers, P. Ercius, G. Dunn, G. Rotskoff, S. Nguyen, V. Adiga, A. Zettl, E. Rabani, P. Geissler, and A. Alivisatos, "Single-particle Mapping of Nonequilibrium Nanocrystal Transformations," vol. 354, no. 6314, pp. 874–877, 2016.

[97] G. Algara-Siller, S. Kurasch, M. Sedighi, O. Lehtinen, and U. Kaiser, "The pristine atomic structure of MoS2 monolayer protected from electron radiation damage by graphene," *Applied Physics Letters*, vol. 103, 203107, 2013.

[98] R. Zan, Q. Ramasse, R. Jalil, T. Georgiou, U. Bangert, and K. Novoselov, "Control of radiation damage in MoS2 by graphene encapsulation," *ACS Nano*, vol. 7, pp. 10167–10174, 2013.

[99] T. Chamberlain, J. Meyer, J. Biskupek, J. Leschner, A. Santana, N. Besley, E. Besley, U. Kaiser, and A. Khlobystov, "Reactions of the inner surface of carbon nanotubes and nanoprotrusion processes imaged at the atomic scale," *Nature Chemistry*, vol. 3, pp. 732–737, 2011.

[100] G. Van Tendeloo, C. Van Heurck, J. Van Landuyt, S. Amelinckx, M. A. Verheijen, P. H. M. Van Loosdrecht, and G. Meijer, "Phase transitions in fullerene (C_{60}) and the related microstructure: a study by electron diffraction and electron microscopy," *The Journal of Physical Chemistry*, vol. 96, no. 18, pp. 7424–7430, 1992.

[101] Y. Lu, M. Kappes, and J. Ibers, "The Structure of the C_{60} molecule: X-Ray Crystal Structure Determination of a Twin at 110 K," *Science*, vol. 254, pp. 408–410, 1991.

[102] P. A. Heiney, J. E. Fischer, A. R. McGhie, W. J. Romanow, A. M. Denenstein, J. P. McCauley Jr., A. B. Smith, and D. E. Cox, "Orientational ordering transition in solid C_{60}," *Phys. Rev. Lett.*, vol. 66, pp. 2911–2914, 1991.

[103] M. S. Dresselhaus, G. Dresselhaus, and P. C. Eklund, "Raman Scattering in Fullerenes," *Journal of Raman Spectroscopy*, vol. 27, pp. 351–371, 1996.

[104] R. Mirzayev, K. Mustonen, M. R. A. Monazam, A. Mittelberger, T. J. Pennycook, C. Mangler, T. Susi, J. Kotakoski, and J. C. Meyer, "Buckyball sandwiches," *Science Advances*, vol. 3, no. 6, e1700176, 2017.

[105] M. Koshino, Y. Niimi, E. Nakamura, H. Kataura, T. Okazaki, K. Suenaga, and S. Iijima, "Analysis of the reactivity and selectivity of fullerene dimerization reactions at the atomic level," *Nature Chemistry*, vol. 2, pp. 117–124, 2010.

[106] K. Suenaga, "PhD thesis," *University of Tokyo*, 1994.

[107] K. Hirahara, S. Bandow, K. Suenaga, H. Kato, T. Okazaki, H. Shinohara, and S. Iijima, "Electron diffraction study of one-dimensional crystals of fullerenes," *Phys. Rev. B*, vol. 64, 115420, 2001.

[108] G. Zhang, R. Zhou, and X. C. Zeng, "Carbon nanotube and boron nitride nanotube hosted C_{60}–V nanopeapods," *J. Mater. Chem. C*, vol. 1, pp. 4518–4526, 2013.

[109] K. Hirahara, K. Suenaga, S. Bandow, H. Kato, T. Okazaki, H. Shinohara, and S. Iijima, "One-dimensional metallofullerene crystal generated inside single-walled carbon nanotubes," *Phys. Rev. Lett.*, vol. 85, pp. 5384–5387, 2000.

[110] C. Reddy, Z. Yu, and Y.-W. Zhang, "Two-dimensional van der Waals C_{60} molecular crystal," *Scientific Reports*, vol. 5, 12221, 2015.

[111] G. Henkelman, B. P. Uberuaga, and H. Jónsson, "A climbing image nudged elastic band method for finding saddle points and minimum energy paths," *The Journal of Chemical Physics*, vol. 113, no. 22, pp. 9901–9904, 2000.

[112] S. Bommel, N. Kleppmann, C. Weber, H. Spranger, P. Schäfer, J. Novák, S. Roth, F. Schreiber, S. Klapp, and S. Kowarik, "Unravelling the multilayer growth of the fullerene C_{60} in real time," *Nature Communications*, vol. 5, 5388, 2014.

[113] H. Liu, Z. Lin, L. V. Zhigilei, and P. Reinke, "Fractal structures in fullerene layers: Simulation of the growth process," *The Journal of Physical Chemistry C*, vol. 112, no. 12, pp. 4687–4695, 2008.

[114] A. V. Talyzin, Y. O. Tsybin, A. A. Peera, T. M. Schaub, A. G. Marshall, B. Sundqvist, P. Mauron, A. Züttel, and W. E. Billups, "Synthesis of C59Hx and C58Hx fullerenes stabilized by hydrogen," *The Journal of Physical Chemistry B*, vol. 109, no. 12, pp. 5403–5405, 2005.

[115] Y. Zou, B. Liu, L. Wang, D. Liu, S. Yu, P. Wang, T. Wang, M. Yao, Q. Li, B. Zou, T. Cui, G. Zou, T. Wågberg, and B. Sundqvist, "Rotational dynamics of confined C_{60} from near-infrared Raman studies under high pressure," *Proceedings of the National Academy of Sciences of the United States of America*, vol. 106, pp. 22135–22138, 2009.

[116] S. Rols, J. Cambedouzou, M. Chorro, H. Schober, V. Agafonov, P. Launois, V. Davydov, A. V. Rakhmanina, H. Kataura, and J.-L. Sauvajol, "How confinement affects the dynamics of C_{60} in carbon nanopeapods," *Phys. Rev. Lett.*, vol. 101, 065507.

[117] K. Matsuda, Y. Maniwa, and H. Kataura, "Highly rotational C_{60} dynamics inside single-walled carbon nanotubes: NMR observations," *Phys. Rev. B*, vol. 77, 075421, 2008.

[118] M. Neek-Amal, N. Abedpour, S. N. Rasuli, A. Naji, and M. R. Ejtehadi, "Diffusive motion of C_{60} on a graphene sheet," *Phys. Rev. E*, vol. 82, 051605, 2010.

[119] A. Rao, K. Zhou, Y. Wang, P. Eklund, G. Hager, W. Lee, X. Bi, J. Holden, D. Cornett, M. Duncan, and I. Amster, "Photoinduced polymerization of solid C_{60} films," *Science*, vol. 259, pp. 955–957, 1993.

[120] J. Onoe, T. Nakayama, M. Aono, and T. Hara, "Structural and electrical properties of an electron-beam-irradiated C_{60} film," *Applied Physics Letters*, vol. 82, pp. 595–597, 2003.

[121] D. Jariwala, T. Marks, and M. Hersam, "Mixed-dimensional van der Waals heterostructures," *Nature Materials*, vol. 16, pp. 170–181, 2016.

[122] Y. Liu, N. Weiss, X. Duan, H.-C. Cheng, Y. Huang, and X. Duan, "Van der Waals heterostructures and devices," *Nature Reviews Materials*, vol. 1, 16042, 2016.

[123] L. Britnell, R. Ribeiro, A. Eckmann, R. Jalil, B. Belle, A. Mishchenko, Y.-J. Kim, R. Gorbachev, T. Georgiou, S. Morozov, A. Grigorenko, A. Geim, C. Casiraghi, A. Castro Neto, and K. Novoselov, "Strong Light-Matter Interactions in Heterostructures of Atomically Thin Films," *Science*, vol. 340, pp. 1311–1314, 2013.

[124] Q. Zheng, W. A. Saidi, Y. Xie, Z. Lan, O. V. Prezhdo, H. Petek, and J. Zhao, "Phonon-assisted ultrafast charge transfer at van der waals heterostructure interface," *Nano Letters*, vol. 17, no. 10, pp. 6435–6442, 2017.

[125] M. Gjerding, R. Petersen, T. Pedersen, N. Mortensen, and K. Thygesen, "Layered van der Waals crystals with hyperbolic light dispersion," *Nature Communications*, vol. 8, 320, 2017.

[126] W. Yu, Q. Vu, H. Oh, H. Nam, H. Zhou, S. Cha, J.-Y. Kim, A. Carvalho, m. s. Jeong, H. Choi, A. Castro Neto, Y. H. Lee, and X. Duan, "Unusually efficient photocurrent extraction in monolayer van der waals heterostructure by tunnelling through discretized barriers," *Nature Communications*, vol. 7, 13278, 2016.

[127] G. Argentero, A. Mittelberger, M. Monazam, Y. Cao, T. Pennycook, C. Mangler, C. Kramberger, J. Kotakoski, A. Geim, and J. Meyer, "Unraveling the 3D atomic structure of a suspended graphene/hBN van der Waals heterostructure," *Nano letters*, vol. 17, pp. 1409–1416, 2017.

[128] I. Leven, T. Maaravi, I. Azuri, L. Kronik, and O. Hod, "Interlayer potential for graphene/h-BN heterostructures," *Journal of chemical theory and computation*, vol. 12, pp. 2896–2905, 2016.

[129] W. Yang, G. Chen, Z. Shi, C. Liu, L. Zhang, G. Xie, M. Cheng, D. Wang, R. Yang, D.-X. Shi, K. Watanabe, T. Taniguchi, Y. Yao, Y. Zhang, and G. Zhang, "Epitaxial growth of single-domain

graphene on hexagonal boron nitride," *Nature materials*, vol. 12, pp. 792–797, 2013.

[130] C. Zhang, S. Zhao, C. Jin, A. L. Koh, y. Zhou, W. Xu, Q. Li, Q. Xiong, H. Peng, and Z. Liu, "Direct growth of large-area graphene and boron nitride heterostructures by a co-segregation method," *Nature communications*, vol. 6, 6519, 2015.

[131] A. Yan, V. Jairo, S. Kahn, K. Watanabe, T. Taniguchi, F. Wang, M. Crommie, and A. Zettl, "Direct growth of single- and few-layer MoS2 on h-BN with preferred relative rotation angles," *Nano letters*, vol. 15, 10, pp. 6324–6331, 2015.

[132] S. Xu, Y. Han, X. Chen, Z. Wu, L. Wang, T. Han, W. Ye, H. Lu, G. Long, Y. Wu, J. Lin, C. Yuan, K. Ho, h. Yuheng, and N. Wang, "Van der Waals epitaxial growth of atomically thin Bi2Se3 and thickness-dependent topological phase transition," *Nano letters*, vol. 15, 4, pp. 2645–2651, 2015.

[133] Z. Zuo, Z. Xu, R. Zheng, A. Khanaki, J.-G. Zheng, and J. Liu, "In-situ epitaxial growth of graphene/h-BN van der Waals heterostructures by molecular beam epitaxy," *Scientific Reports*, vol. 5, 14760, 2015.

[134] T. Hertel, R. E. Walkup, and P. Avouris, "Deformation of carbon nanotubes by surface van der Waals forces," *Phys. Rev. B*, vol. 58, pp. 13870–13873, 1998.

[135] Y. Jiang, W. Zhou, T. Kim, Y. Huang, and J.-M. Zuo, "Measurement of radial deformation of single-wall carbon nanotubes induced by intertube van der Waals forces," *Phys. Rev. B*, vol. 77, 153405, 2008.

[136] R. Ruoff, J. Tersoff, D. Lorents, S. Subramoney, and B. Chan, "Radial deformation of carbon nanotubes by van der Waals forces," *Nature*, vol. 364, pp. 514–516, 1993.

[137] T. Kim, G. Kim, W. I. Choi, Y.-K. Kwon, and J.-M. Zuo, "Electrical transport in small bundles of single-walled carbon nanotubes: Intertube interaction and effects of tube deformation," *Applied Physics Letters*, vol. 96, no. 17, 173107, 2010.

[138] S. Paulson, A. Helser, M. Buongiorno Nardelli, R. Taylor, M. Falvo, R. Superfine, and S. Washburn, "Tunable resistance of a carbon

nanotube-graphite interface," *Science*, vol. 290, pp. 1742–1744, 2001.

[139] K. Mustonen, A. Hussain, C. Hofer, M. R. A. Monazam, R. Mirzayev, K. Elibol, P. Laiho, C. Mangler, H. Jiang, T. Susi, E. I. Kauppinen, J. Kotakoski, and J. C. Meyer, "Atomic-scale deformations at the interface of a mixed-dimensional van der waals heterostructure," *ACS Nano*, vol. 12, no. 8, pp. 8512–8519, 2018.

[140] S. Haigh, A. Gholinia, R. Jalil, S. Romani, L. Britnell, D. Elias, K. Novoselov, L. Ponomarenko, A. K. Geim, and R. Gorbachev, "Cross-sectional imaging of individual layers and buried interfaces of graphene-based heterostructures and superlattices.," *Nature materials*, vol. 11, pp. 764–767, 2012.

[141] A. Rooney, A. Kozikov, A. Rudenko, E. Prestat, M. Hamer, F. Withers, Y. Cao, K. Novoselov, M. Katsnelson, R. Gorbachev, and S. Haigh, "Observing Imperfection in Atomic Interfaces for van der waals heterostructures," *Nano Letters*, vol. 17, 9, pp. 5222–5228, 2017.

[142] A. Hashimoto, K. Suenaga, K. Urita, T. Shimada, T. Sugai, S. Bandow, H. Shinohara, and S. Iijima, "Atomic correlation between adjacent graphene layers in double-wall carbon nanotubes," *Physical review letters*, vol. 94, 045504, 2005.

[143] J.-F. Colomer, L. Henrard, P. Lambin, and G. van Tendeloo, "Electron diffraction study of small bundles of single-wall carbon nanotubes with unique helicity," *Phys. Rev. B*, vol. 64, 125425, 2001.

[144] Z. Liu and L.-C. Qin, "A direct method to determine the chiral indices of carbon nanotubes," *Chemical Physics Letters*, vol. 408, pp. 75–79, 2005.

[145] J. Meyer, M. Paillet, G. Duesberg, and S. Roth, "Electron diffraction analysis of individual single-walled carbon nanotubes," *Ultramicroscopy*, vol. 106, pp. 176–90, 2006.

[146] H. Jiang, D. P. Brown, A. G. Nasibulin, and E. I. Kauppinen, "Robust bessel-function-based method for determination of the (n, m) indices of single-walled carbon nanotubes by electron diffraction," *Phys. Rev. B*, vol. 74, 035427, 2006.

[147] P. Lambin and A. A. Lucas, "Quantitative theory of diffraction by carbon nanotubes," *Phys. Rev. B*, vol. 56, pp. 3571–3574, 1997.

[148] H. Jiang, A. Nasibulin, D. Brown, and E. Kauppinen, "Unambiguous atomic structural determination of single-walled carbon nanotubes by electron diffraction," *Carbon*, vol. 45, pp. 662–667, 2007.

[149] S. Amelinckx, A. Lucas, and P. Lambin, "Chapter 3 - Electron Diffraction and Microscopy of Carbon Nanotubes," pp. 14–28, 1999.

[150] C. Giusca, Y. Tison, and S. R. Silva, "Atomic and electronic structure in collapsed carbon nanotubes evidenced by scanning tunneling microscopy," *Physical Review B*, vol. 76, 035429, 2007.

[151] Y. Chen, Z. Shen, X. Ziwei, Y. Hu, H. Xu, S. Wang, X. Guo, Y. F. Zhang, L.-M. Peng, F. Ding, Z. Liu, and J. Zhang, "Helicity-dependent single-walled carbon nanotube alignment on graphite for helical angle and handedness recognition," *Nature communications*, vol. 4, 2205, 2013.

[152] M.-F. Yu, O. Lourie, M. J. Dyer, K. Moloni, T. F. Kelly, and R. S. Ruoff, "Strength and breaking mechanism of multiwalled carbon nanotubes under tensile load," *Science*, vol. 287, no. 5453, pp. 637–640, 2000.

[153] V. Lordi and N. Yao, "Radial compression and controlled cutting of carbon nanotubes," *The Journal of Chemical Physics*, vol. 109, no. 6, pp. 2509–2512, 1998.

[154] M.-F. Yu, T. Kowalewski, and R. S. Ruoff, "Investigation of the radial deformability of individual carbon nanotubes under controlled indentation force," *Phys. Rev. Lett.*, vol. 85, pp. 1456–1459, 2000.

[155] M.-F. Yu, M. J. Dyer, and R. S. Ruoff, "Structure and mechanical flexibility of carbon nanotube ribbons: An atomic-force microscopy study," *Journal of Applied Physics*, vol. 89, no. 8, pp. 4554–4557, 2001.

[156] J. Tersoff and R. S. Ruoff, "Structural properties of a carbon-nanotube crystal," *Phys. Rev. Lett.*, vol. 73, pp. 676–679, 1994.

[157] J. Tang, L.-C. Qin, T. Sasaki, M. Yudasaka, A. Matsushita, and S. Iijima, "Compressibility and polygonization of single-walled carbon nanotubes under hydrostatic pressure," *Physical review letters*, vol. 85, 1887, 2000.

[158] H.-Y. Wang, M. Zhao, and S. X. Mao, "Radial moduli of individual single-walled carbon nanotubes with and without electric current flow," *Applied Physics Letters*, vol. 89, no. 21, 211906, 2006.

[159] Z. R. Abrams and Y. Hanein, "Tube - tube and tube - surface interactions in straight suspended carbon nanotube structures," *The Journal of Physical Chemistry B*, vol. 110, no. 43, pp. 21419–21423, 2006.

[160] Z. Abrams and Y. Hanein, "Radial deformation measurements of isolated pairs of single-walled carbon nanotubes," *Carbon*, vol. 45, no. 4, pp. 738–743, 2007.

[161] R. S. Ruoff, D. Qian, and W. K. Liu, "Mechanical properties of carbon nanotubes: theoretical predictions and experimental measurements," *Comptes Rendus Physique*, vol. 4, no. 9, pp. 993–1008, 2003.

[162] S. Barraza-Lopez, P. M. Albrecht, and J. W. Lyding, "Carbon nanotubes on partially depassivated n-doped Si(100)$-(2 \times 1)$: H substrates," *Phys. Rev. B*, vol. 80, 045415, 2009.

[163] T. Odom, J.-L. Huang, P. Kim, and C. Lieber, "Atomic structure and electronic properties of single-walled carbon nanotubes," *Nature*, vol. 391, pp. 62–64, 1998.

[164] C. Li, "Elastic properties of single-walled carbon nanotubes in transverse directions," *Phys. Rev. B*, vol. 69, 073401, 2004.

[165] C. Hofer, C. Kramberger, M. Monazam, C. Mangler, A. Mittelberger, G. Argentero, J. Kotakoski, and J. Meyer, "Revealing the 3D structure of graphene defects," *2D Materials*, vol. 5, 045029, 2018.

[166] O. Krivanek, M. Chisholm, V. Nicolosi, T. Pennycook, G. Corbin, N. Dellby, M. Murfitt, C. Own, Z. Szilagyi, M. Oxley, S. Pantelides, and S. Pennycook, "Atom-by-atom structural and chemical analysis by annular dark-field electron microscopy," *Nature*, vol. 464, pp. 571–5744, 2010.

[167] J. Warner, N. Young, A. Kirkland, and G. Briggs, "Resolving strain in carbon nanotubes at the atomic level," *Nature materials*, vol. 10, pp. 958–62, 2011.

[168] M. Ishigami, H. Choi, S. Aloni, S. Louie, M. Cohen, and A. Zettl, "Identifying defects in nanoscale materials," *Physical review letters*, vol. 93, 196803, 2004.